Straintronic photodetectors based on 2D materials

Supervisors: Andrés Castellanos Gómez and Riccardo Frisenda
Tutor: Nicolás Agraït de la Puente

Patricia Gant Pinar

Contents

List of Figures

1. Introduction

the flake. (e) The flexible substrate is expanded while the flake is being transferred so once the strain is release from the substrate, wrinkles appear in the surface of the flake with certain amplitude and periodicity.

Figure 8.

Band structure of 1L-MoS_2 when no strain is applied, 25% of uniaxial strain is applied and 21% of biaxial strain is applied. The graphs are extracted from the work of Miao *et al*.[31]

Figure 9.

Image extracted from Conley's experiments.[38] a) and c) show the photoluminescence spectra of 1L-MoS_2 (a) and 2L-MoS_2 (c) under different levels of strain applied. b) and d) illustrate the energies of the excitonic peaks for each level of strain, in which the shift of the peaks can be observed.

2. Isolation and optical characterization of 2D materials

Figure 1.

(a) Optical image of the deterministic transfer setup. The main components of the system are indicated in the image. (b) Detail image of the manipulators of the setup while transferring a flake between Au electrodes.

Figure 2.

Optical images of the different steps of the deterministic transfer of a MoS_2 flake between Au electrodes.

Figure 3.

(a) Optical image of the Raman/photoluminescence setup, in which the main components of the system are highlighted. (b) Image of the software used for controlling the equipment during the measurements. The parameters shown are the main adjustable characteristics of the spectra recording.

Figure 4.

Raman spectra and optical images of the laser spot focused on the surface of (a) a black phosphorus flake, (b) a 1L-$MoSe_2$ flake and (c) a multilayer graphene flake.

Figure 5.

(a) Raman spectra of MoS_2 with 1L, 2L, 3L and 4L measured with a 532 nm excitation laser and vertically displaced 0.1. (b) Photoluminescence of MoS_2 with 1L, 2L, 3L and 4L measured with a 532 nm excitation.

Figure 6.

(a) Optical image of the micro-reflectance and transmittance setup with the main components marked. (b) Zoom in the modified trinocular of the setup pointing the components.

Figure 7.

(a) Optical images of the illuminated spot from where the spectrometer is collecting the light. The first image the spot is focused in the image plane and the second one the spot is out of focus. (b) Spectrum of the microscope light in transmission mode at maximum intensity with an acquisition time of 4 s and averaging 5 spectra. (c) Spectrum of the microscope light in reflection mode at maximum intensity with an acquisition time of 4 s and averaging 5 spectra.

Figure 8.

(a) Spectra in transmission mode of the light going through the sample (red), in this case a 1L-MoS_2, and the substrate (blue), which is PDMS. These data allow us to calculate the transmittance of the sample, resulting the black spectrum. (b) Spectra in reflection mode of the light going towards the sample (red), in this case a 1L-MoS_2, and the substrate (blue), which is PDMS. These data allow us to calculate the differential reflectance of the sample, resulting the black spectrum.

Figure 9.

Transmittance spectra from 1L (dark blue) to 4L (red) measured in (a) MoS_2, (b) $MoSe_2$, (c) WS_2 and (d) WSe_2 samples on PDMS substrate.

Figure 10.

Differential reflectance spectra from 1L (dark blue) to 4L (red) measured in (a) MoS_2, (b) $MoSe_2$, (c) WS_2 and (d) WSe_2 samples on PDMS substrate.

Figure 11.

(a) Optical image acquired in transmission mode of a MoS_2 flake with areas of different thicknesses. (b) Profiles of the transmittance in the red, green and blue channels along the line plotted in (a).

Figure 12.

Histograms of 1-transmittance calculated in 202 MoS_2 flakes for the red, green and blue channels.

Figure 13.

(a) Raman spectra of MoS_2 with 1L, 2L, 3L and 4L measured with a 532 nm excitation laser and vertically displaced 0.1. (b) Photoluminescence of MoS_2 with 1L, 2L, 3L and 4L measured with a 532 nm excitation. (c) Differential reflectance spectra of MoS_2 with 1L, 2L, 3L and 4L. (d) Scatter plot of the transmittance of the 202 MoS_2 flake in the blue channel together with the histogram shown in Figure 13.

Figure 14.

(a)-(d) Histograms of 1-transmittance calculated in 50 MoS_2 flakes doped with (a) Co, (b) Ni, (c) Fe and (d) Nb. (e) Values of 1-

transmittance for different number of layers of MoS_2 with different doping extracted from the gaussian fits of the histograms.

Figure 15.

(a)-(d) Histograms of 1-transmittance calculated in (a) 202 MoS_2 flakes, (b) 200 $MoSe_2$ flakes, (c) 200 WS_2 flakes and (d) 200 WSe_2 flakes. (e) Values of 1-transmittance for different number of layers of MoS_2, $MoSe_2$, WS_2 and WSe_2 extracted from the gaussian fits of the histograms.

3. Electrical contacts on 2D flakes

Figure 1.

Scheme of the different steps of the electron beam lithography. The example shows a SiO_2/Si substrate in which Au is evaporated.

Figure 2.

Scheme of the different steps of the photolithography. The example shows a SiO_2/Si substrate in which Au is evaporated.

Figure 3.

(a) Optical image of a commercial shadow mask (Ossila E321) stuck on a SiO_2/Si substrate with few pieces of Kapton tape. (b) Optical image of a SiO_2/Si substrate with Au/Ti pre-patterned electrodes. In this case, this sample is commercially available in Ossila (S221).

Figure 4.

(a) Optical image of a device contacted by wire bonding. The bonds in the Au pads are indicated in the image. (b) Optical image of the same sample contacted by wire bonding obtained at lower magnification in order to appreciate the bonds in the Cu board.

Figure 5.

Scheme of the main steps of the wire bonding for all the cases.

Figure 6.

(a) Optical image of the Linkam probe station with the main components indicated. (b) Optical image of the scanning photocurrent setup in which the Linkam is embedded.

Figure 7.

(a) Optical image of the home-made probe station with two probes. The different components are pointed in the image. (b) Zoomed image of the sample stage in which the two probes can be appreciated while they are contacting the sample.

Figure 8.

(a) Optical image of a home-made probe station to perform measurements in vacuum. The different components are pointed in the

image. (b) Image of the probe station when the isolated chamber is opened. Here, the micromanipulators in which the probes are mounted, and the sample stage can be observed.

Figure 9.

(a) Optical image of a home-made probe station to perform measurements in vacuum. The different components are pointed in the image. (b) Image of the probe station when the isolated chamber is opened. Here, the magnetic probes are mounted, and the sample stage can be observed.

Figure 10.

(a) Current versus bias voltage curves for a single-layer MoS_2 device measured in air conditions (red) and a pressure of $2.8 \cdot 10^{-6}$ mbar (blue). The measurements are performed in dark conditions and no gate voltage applied. (b) Gate traces measured in the same device at a bias voltage of 1 V in dark conditions. (c) Time traces recorded at an applied bias voltage of 1 V and no gate voltage applied. The LED used has a wavelength of 420 nm and a power density of 3 $\mu W/cm^2$. The light was turned on and off to observe the sample response.

Figure 11.

(a) Photocurrent spectra of the single-layer MoS_2 sample measured in air (red) and vacuum (blue) conditions. Each point corresponds to the photocurrent value calculated by subtracting the dark current to the current in light conditions. The measurements are time traces like the ones shown in Figure 12(c), measured with LEDs of different wavelengths (420 nm, 470 nm, 530 nm, 565 nm, 595 nm, 660 nm, 740 nm) and power density of 3 $\mu W/cm^2$. (b) Photocurrent dependency on the light power density of the single-layer MoS_2 sample measured in air (red) and vacuum (blue) conditions. Each point corresponds to the photocurrent value calculated by subtracting the dark current to the current in light conditions. The measurements are time traces like the ones shown in Figure 12(c), measured with a LED with a wavelength of 420 nm at different power densities (0.1 $\mu W/cm^2$, 3 $\mu W/cm^2$, 5.5 $\mu W/cm^2$, 8.4 $\mu W/cm^2$, 11.9 $\mu W/cm^2$).

Figure 12.

Comparison between a human hair and a PAN carbon fiber (7 μm of diameter) in the zoom lens.

Figure 13.

(a) Metallic needle welded to a PCB piece. (b) The piece with the needle is mounted in the deterministic transfer setup while a long carbon fiber is attached to the glass with tape. The glass slide is attached to an XYZ stage that allows the placement of the carbon fiber on the needle. This process is inspected by the zoom lens. (c) The carbon fiber is in contact with the metallic needle. (d) The carbon fiber is attached to the needle with one drop of silver paint. (e) The silver paint is already dry, so the

carbon fiber is contacted with the needle. (f) The long carbon fiber is cut with a nail cuticle nipper.

Figure 14.

(a) Optical image of the two carbon fiber microprobes setup. (b) Detail of the XYZ micro-stage used to move the probes. (c) Optical image of two carbon fiber tips contacting a MoS_2 flake on SiO_2/Si.

Figure 15.

The resistance measured between silver drop contacts at different distances in the carbon fiber.

Figure 16.

(a) Resistance measured in a TiS_3 nanoribbon at different distances between the two carbon fiber probes. (b) Current versus voltage curves recorded in order to measure the resistance at different distances in the flake.

Figure 17.

Current measurement while the probe is contacting the Au substrate, being the fluctuations due to the manual manipulation with the micro-stage.

Figure 18.

(a) Illustration of the MoS_2 flake transferred on Au substrate and the electrical connections to measure with the carbon fiber. (b) Optical image of the MoS_2 flake with different thicknesses on Au. Inset: Carbon fiber contacting the bilayer area of the flake. (c) Current versus bias voltage measured in the areas marked in (b). Inset: Resistance extracted from the IVs at bias voltage of 1V, subtracting the fiber resistance.

Figure 19.

(a) Illustration of the n-type MoS_2 flake transferred on p-type Si substrate and the electrical connections set for the measurements. (b) Optical image of the sample of MoS_2 transferred on Si. Inset: Transmission image of the MoS_2 flake to facilitate the recognition. (c) Current versus voltage curves for the p-n junction fabricated, measured in dark conditions (black trace) and under illumination with white light (blue).

Figure 20.

(a) Illustration of the MoS_2 flake on SiO_2/Si substrate and the electrical connection to measure with two carbon fiber probes. (b) Optical image of the MoS_2 flake on SiO_2, being the marked area the trilayer measured. Inset: MoS_2 trilayer contacted by two carbon fiber probes. (c) Current versus bias voltage traces measured at different gate voltages applied, ranging from -20 V to 20 V. Inset: Current extracted from the IVs at a bias voltage of 1 V for each gate voltage.

Figure 21.

(a) Photocurrent versus bias voltage traces measured under illumination with light wavelength of 455 nm at different power densities. Inset:

Photocurrent extracted from the IVs at bias voltage of 10 V for each light power density. (b) Response time measurements under illumination with LED sources of 455 nm (dark blue), 505 nm (light blue), 617 nm (yellow) and 660 nm (red) at fixed power density of 160 mW/cm^2 and bias voltage of 10 V. (c) Photocurrent spectrum extracted from measurements at bias voltage of 10V and power density of 140 mW/cm^2. The differential reflectance spectrum of MoS_2 flake is shown in the same graph.

Figure 22.

(a) Current versus voltage curves measured in the out-of-plane direction of a MoS_2 multilayer region transferred on Au substrate with one carbon fiber probe. The graph shows the trace and the retrace for each measurement. (b) Resistance calculated from the IVs measured in regions with different thicknesses of the MoS_2 flake on Au substrate, using the same configuration with one carbon fiber probe. The filled circles correspond to the trace and the unfilled circles to the retrace.

Figure 23.

Time trace of the MoS_2 sample transferred on Au substrate and measured in the out-of-plane direction with one carbon fiber probe. The bias voltage is kept at 10 V and the illumination is modulated with a square signal in a LED source of 505 nm with a power density of 160 mW/cm^2.

Figure 24.

(a) Optical images with better resolution of the flake before and after sweeping with a metallic wire. The last panel is the AFM image acquired after sweeping with the metallic wire. (b) Optical images of a carbon fiber sweeping a MoS_2 monolayer area. (c) Optical images with better resolution of the flake before and after sweeping. The last panel is the AFM image acquired after sweeping with the carbon fiber tip.

Figure 25.

Current versus bias voltage characteristics measured in flakes of (a) multilayer graphene flake, (b) WS_2 flake, (c) TiS_3 flake and (d) black phosphorus.

4. Strain tunable single-layer MoS_2 photodetector

Figure 1.

(a) Schematic representation of the single-layer MoS_2 photodetectors configuration and the setup in which the measurements were performed. There is a thermal stage underneath the device. The sample is illuminated with a light spot from the top. (b) Optical transmission

image of a single-layer MoS_2 photodetector. The substrate is polycarbonate (PC) and the source and drain electrodes are made of Au/Ti.

Figure 2.

Finite element calculation of a biaxial strain test sample consisting of a 100-μm-thick substrate and single-layer MoS_2 (0.7 nm thickness) on the substrate. The curve represents the maximum transferred strain in MoS_2 as a function of substrate's Young's Modulus.

Figure 3.

(a) Differential reflectance spectra measured at 25 ºC (dark blue), 60 ºC (light blue), 80 ºC (yellow) and 100 ºC (red). They are translated by 0.08 in the vertical axis. Inset: Calculated A exciton wavelength from the spectra shown. (b) Optical transmission photo of the single-layer MoS_2 device showing the different areas. (c)-(e) Exciton A energy maps, calculated from the differential reflectance spectra in each point measured at 25 ºC (c), 60 ºC (d) and 80 ºC (e).

Figure 4.

(a) Optical transmission images of the PC substrate with patterned pillars at -120 ºC and 40 ºC. (b) Zoom in the same area of the substrate for both temperatures in order to distinguish the expansion of the substrate thanks to the change in the distance between the pillars. (c) Calibration of the PC strain dependency on the temperature.

Figure 5.

Xenon lamp power spectrum recorded after passing through the zoom lens. The optical fiber used has a core of 400 μm.

Figure 6.

Response time of a single-layer MoS_2 photodetector at 0% (blue), 0.22% (green), 0.35% (orange) and 0.48% (red) of applied strain.

Figure 7.

Responsivity spectrum of an unstrained single-layer MoS_2 photodetector. Each dot corresponds to the value extracted from a response time measurement recorded at a bias voltage of 10 V and illuminated with a light power of 8 mW/cm^2.

Figure 8.

(a) Responsivity spectra of a single-layer MoS_2 photodetector measured at -0.80% (dark blue), -0.48% (light blue), -0.16% (green), 0.16% (yellow) and 0.48% (red) of applied strain. Each dot corresponds to the value extracted from a response time measurement recorded at a bias voltage of 10 V and illuminated with a light power of 8 mW/cm^2. The spectra are multiplied by certain factors in order to facilitate the comparison: -0.80% by 10, -0.48% by 10, -0.16% by 6 and 0.16% by 1.7. (b) Cut-off wavelengths calculated from the fits of the responsivity spectra of three single-layer MoS_2 photodetectors measured at different

strain ranges. Inset: Exciton A wavelengths of the same spectra calculated from the fits.

Figure 9.

(a) Responsivity spectra of a single-layer MoS_2 photodetector fabricated on PC measured at 25 ºC (0% of strain) and 100 ºC (0.48% of strain). Each dot corresponds to a response time measurement at 10 V of bias voltage and illuminated with a power density of 8 mW/cm^2. (b) Responsivity spectra of a single-layer MoS_2 photodetector fabricated on SiO_2/Si measured at 25 ºC and 100 ºC (in this case there is no strain applied). Each dot corresponds to a response time measurement at 10 V of bias voltage and illuminated with a power density of 8 mW/cm^2.

Figure 10.

Schematic of the photogating mechanism. In the left, the n-type semiconductor in dark conditions conduces the majority carriers (electrons in this case) between the electrodes. In the right, the illumination produces the separation between electrons and holes in the material. The majority carriers (electrons) travel between electrodes while part of the minority carriers (holes) are trapped in the defects or impurities of the semiconductor material.

Figure 11.

(a) Optical reflection photo of a single-layer MoS_2 photodetector on PC with the different areas marked. (b) Reflection map of the same photodetector measured with a laser of 650 nm. (c) Current maps of the same photodetector measured at 25 ºC, 50 ºC and 70 ºC. The lines show the same areas marked in the photo on (a) and the reflection map on (b).

Figure 12.

(a) Schematic of the band diagram for each case of applied voltage between the electrodes. (b)-(d) Current linecuts in the single-layer MoS_2 photodetector shown in Figure 8(a) measured with the same laser and applying bias voltages from -50 mV to 50 mV (measurements changing the bias voltage in 5 mV). Only few of the linecuts are shown for clarity. The electrodes area is marked with a dark area in the graphs. These linecuts were performed at 25 ºC (a), 50 ºC (b) and 70 ºC (c). (e)-(g) Current barrier measured in the left electrode at different applied bias voltages. The grey line corresponds to the fit of the linear part of the data (excluded the data points corresponding to the noise level). The fit provides an estimation of the Schottky barrier height at each temperature, given by the cut of the fit with the horizontal axis.

Figure 13.

(a) Response time to strain of a single-layer MoS_2 photodetector. The OFF state corresponds to 0.16% of strain and ON state is 0.48% of strain. The cycles are measured at bias voltage of 5 V and light wavelength of 740 nm with a power density of 5 mW/cm^2. (b) Zoom in the third strain cycle of the measurements shown in (a) to allow the

calculation of the rise and fall times, extracted with the 10%-90% criterion.

Figure 14.

Responsivities of a single-layer MoS_2 photodetector measured at a bias voltage of 10 V and illuminating with light wavelength of 740 nm and a power density of 12 mW/cm^2. The strain cycles shown are the cycle 5, 20, 30 and 40.

Ackowledgements

This thesis would not have been possible without all the help, guidance and support of Andrés Castellanos Gómez and Riccardo Frisenda, my two supervisors. Andrés, muchas gracias por haberme dado la oportunidad de trabajar y aprender de ti, para mí ha sido una gran experiencia que siempre recordaré con cariño. Y gracias por no dejar que me conforme, no habría sido capaz de terminar si no fuese por ti. Riccardo, thanks for the support during my ups and downs, I learnt a lot from you and will always remember it.

Along the time, a lot of people have helped me, taught me and supported me. First, all the people in the group; Mar, Carmen and Elena, cada una a su manera me habéis ayudado y enseñado durante el camino, gracias por vuestro apoyo. David y Aday, con vosotros empecé a trabajar en esto, muchas gracias por todos los buenos momentos y por toda vuestra ayuda. Qinghua thanks for always pushing me to give more, your big sister is really proud of you. Félix, muchas gracias por todas las risas y el apoyo, espero que sigas disfrutando durante la tesis. Begoña, muchas gracias por siempre escucharme y ayudarme, y por todas las anécdotas divertidas y los buenos ratos. Ryu, me alegro de haber compartido el último año en el laboratorio contigo, ha sido divertido.

I am also thankful to all the collaborators and other people (Simon, Jesús, Gabriel, Irene, Sergio, Hao and so many others) that I met during these years for their patience and support.

Muchas gracias a mis elefantitas (Alessandra, Gemma, Xoana, María y Luz), porque sin vosotras mi vida habría sido mucho más gris durante estos años y sin vuestro apoyo, no habría sido capaz de seguir adelante después de cada caída.

A mi familia, gracias por haberme enseñado a luchar y no conformarme (aunque sólo sea por demostrar que la gente se equivoca conmigo). Sin todos vosotros, nunca habría llegado a donde estoy.

Muchas gracias Bruno, por empujarme a empezar el doctorado y acompañarme durante parte del camino.

Finally, I am really thankful for all the support from my husband, Niko. You made my last years of PhD an unforgettable experience. Thanks for all the support, you made my life brighter and pushed me to finish the thesis.

Abstract

The world suffered an enormous revolution thanks to the emergence of the electronics; nowadays, our lives are surrounded by electronic devices that make them easier. Since the first fabrication of a transistor (the base the most common electronic devices) in 1947, electronics is been improving its performance by adding more elements to the electronic devices. In order to maintain the level of improvement, the size of the components included in the electronic devices decreased, which have led to difficulties during the last years. Researchers are looking for different strategies to continue the enhancement of electronics, among which is the study of new materials like 2D semiconductors. Likewise, another proposed idea is including more tuning knobs in the components, which would increase the functionality of each component. The different options for increasing the responses of the components include the control of different properties (degrees of freedom) of the device through control the valey or spin polarization or applying external deformations leading to valleytronics, spintronics, straintronics respectively.

The main aim of this thesis is the development of a proof-of-concept straintronic device, which would proof the viability of this technique to keep the electronic progress. Thus, this device is fabricated with a new semiconductor, which allows us to fabricate this type of device unlike silicon (Si). This new material is a 2D semiconductor from the transition metal dichalcogenides (TMDCs) family, MoS_2. Due to the special characteristics of 2D materials, the techniques used for studying and manipulating them are different from the common methods used in 3D semiconductor industry.

So, we introduce the optical techniques that allow us to characterize the optical properties of these materials. Some of them, like Raman and photoluminescence spectroscopies, are well spread in the material science world while some others are used specifically in 2D materials. All the different optical methods used along the thesis are presented in Chapter 2, where the details for studying the TMDCs family are included.

The different steps and methods used for electrically contact and measure these materials are explained in Chapter 3. Here, the steps of the different processes are presented with the options available depending on the needs of the experiment.

Moreover, one technique developed during the thesis which allows to minimize the number of steps is explained in this Chapter.

In Chapter 4, we fabricate several MoS_2 simple photodetector devices which can be strained. These photodetectors show an optoelectrical response to the strain, which is the mayor goal of this thesis. Different experiments prove the reliability of this new design for electronic components.

The results achieved in the last Chapter open a new path for researching this type of devices. As mentioned, the new design will allow to have components with higher functionalities and the use of 2D materials solve some of the issues lately found in the electronics industry. Moreover, the 2D devices can be mixed with the current Si technology, for improving the performance of the electronic devices. Thus, new concept devices would keep the improvement race in the electronic world.

Resumen

El mundo sufrió una gran revolución cuando la electrónica hizo su aparición; hoy en día, nuestras vidas están rodeadas de dispositivos electrónicos, los cuáles las hacen más fáciles. Desde la fabricación del primer transistor (la base de todos los dispositivos electrónicos) en 1947, la electrónica ha continuado mejorando su rendimiento mediante la agregación de más componentes en los dispositivos electrónicos. Para ser capaces de seguir con la optimización y aumento de componentes, el tamaño de estos disminuyó, lo que ha venido provocando dificultades durante los últimos años. Los investigadores están buscando diferentes estrategias para continuar con la mejora de los dispositivos electrónicos, entre los cuales se encuentran el estudio de nuevos materiales como los semiconductores 2D. Asimismo, otra idea propuesta para mejorar estos dispositivos es incluir más funcionalidades en los componentes, lo que aumentará las respuestas de cada uno de ellos. Las diferentes opciones que permitirían variar y aumentar el número de respuestas de los componentes incluyen el control de diferentes propiedades del dispositivo a través de la valetrónica, espintrónica o deformatrónica.

El objetivo principal de esta tesis es el desarrollo de un ejemplo de dispositivo deformatrónico, que demostrará la viabilidad de esta técnica para mantener el progreso electrónico. Así, este dispositivo se fabricará con un nuevo semiconductor, el cual nos permite conseguir este tipo de dispositivo a diferencia del silicio (Si). Este nuevo material es un semiconductor 2D de la familia de los dicalcogenuros de metales de transición (TMDCs), el MoS_2. Debido a las características especiales de los materiales 2D, las técnicas utilizadas para estudiarlos y manipularlos son diferentes de los métodos comúnmente utilizados en la industria de semiconductores 3D.

Por lo tanto, es necesario que presentemos las técnicas ópticas que nos permiten caracterizar las propiedades ópticas de estos materiales. Algunas de ellas, como las espectroscopias Raman y de fotoluminiscencia, son bien conocidas en el mundo de la ciencia de los materiales, mientras que otras se usan específicamente en materiales 2D. Los diferentes métodos ópticos utilizados a lo largo de la tesis se presentan en el Capítulo 2, donde se incluyen los detalles para el estudio de la familia de los TMDCs.

Del mismo modo, los diferentes pasos y métodos utilizados para el contacto eléctrico y la medición de estos materiales se explican en el Capítulo 3. Aquí, los pasos del proceso de fabricación y medida se presentan con las diferentes opciones disponibles para llevarlos a cabo dependiendo de las necesidades. Por último, en este capítulo se explica una técnica desarrollada durante la tesis que permite minimizar el número de pasos del proceso.

Toda esta información sobre las técnicas y métodos ópticos y eléctricos utilizados durante el trabajo nos facilita la presentación y compresión de los estudios realizados en los dispositivos deformatrónicos de MoS_2. En el Capítulo 4, fabricamos varios dispositivos de geometría sencilla de MoS_2, fotodetectores, que pueden ser sometidos a deformaciones. Estos fotodetectores muestran diferencias en su respuesta ante la deformación, que es el objetivo principal de esta tesis. Diferentes experimentos demuestran la fiabilidad y adecuación de este nuevo diseño para su inclusión como componentes electrónicos.

Los resultados obtenidos en el último capítulo abren un nuevo camino para investigar este tipo de dispositivos. Como se mencionó anteriormente, el nuevo diseño permitirá tener componentes con mayor funcionalidad y el uso de materiales 2D resolverá algunos de los problemas encontrados recientemente en la industria electrónica. Además, los dispositivos 2D se pueden combinar con la tecnología del Si actual para mejorar el rendimiento de los dispositivos electrónicos. Por lo tanto, este nuevo concepto de dispositivo permitirá mantener la carrera en el progreso de la electrónica.

1. Introduction

1.1 Modern electronics

Nowadays, our world is surrounded by electronic devices which make our lives easier. Starting from our phone to the fridge, everything works thanks to the invention of the electronics. Modern electronics is based on a key component discovered in 1947, the transistor.[1] The transistor is a component built with semiconducting materials, which resulted in the development of the solid-state electronics.

The schematics of the first point-contact transistor is shown in Figure 1(b), in which the main component is a piece of Ge. The device has three electrodes connected to the Ge: the emitter, the collector and the base. The emitter and the collector electrodes contact the Ge just in one point, while the base electrode covers the Ge block in one side for amplifying the current. An optical image of the real device is shown in Figure 1(a).

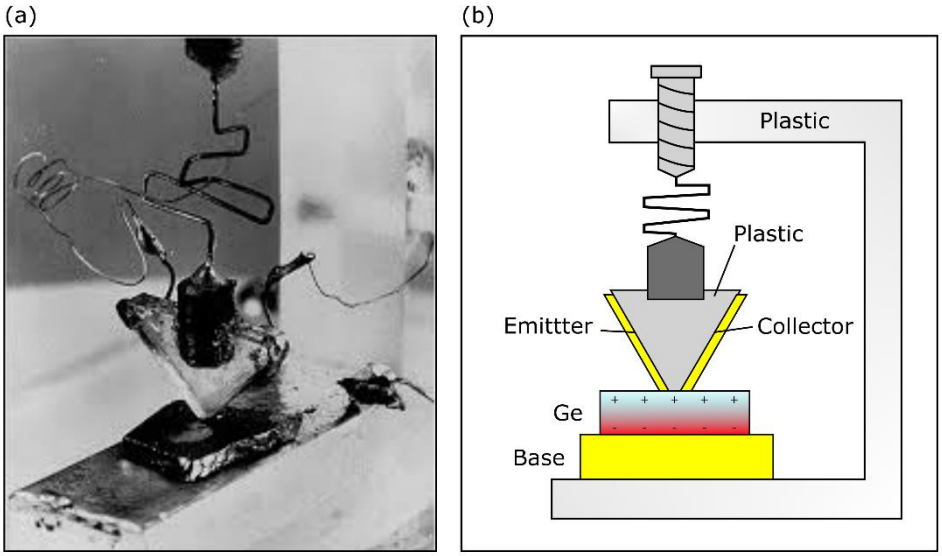

Figure 1. (a) Photo of the first point-contact transistor fabricated by John Bardeen and Walter Brattain in 1947. (b) Schematic of a point-contact transistor, with the main components marked.

Even though the first transistor was fabricated with Ge, the lack of reproducibility due to technical difficulties with controlling the fabrication and doping processes forced the quest of another material.[2,3] The Si was the semiconductor which rapidly substituted the Ge, thanks to the surface stability of Si due to the formation of the native oxide layer. In the present, Si is still the most used material in electronic components, proving its adequacy.

The transistor which was developed for commercialization was not the point-contact transistor in the end, but the bipolar junction transistor (BJT), shown in Figure 2. Thanks to this design, the transistor industry started to overcome some of the problems shown by the vacuum tubes (the technology used in electronics before the transistors) regarding power consumption and waste heat.[3,4] However, bipolar junction transistors still had integration issues for allowing the miniaturization of circuits required by the customers (especially military demands).

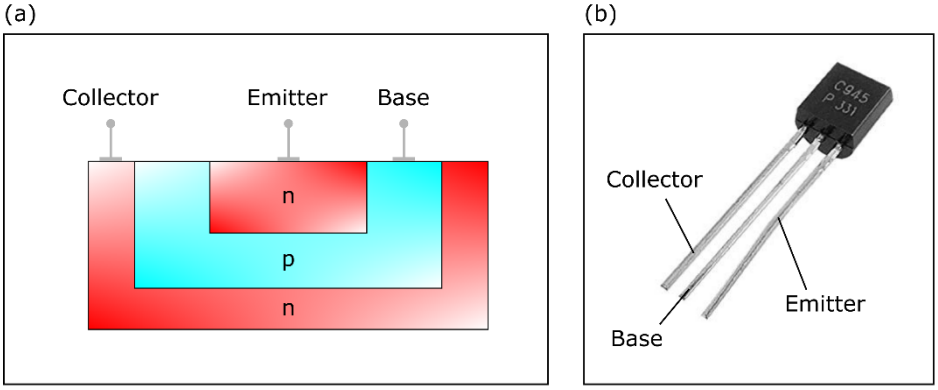

Figure 2. (a) Schematic of a npn bipolar junction transistor (BJT), with the main components marked. (b) Photo of a BJT real model sold in the market with the three electrodes labelled.

Among all the approaches investigated for improving the implementation of transistors, the integrated circuit was the design solution which most of companies started to research. Thus, the monolithic integrated circuit (IC) designed by Robert Noyce in 1960 became the standard of the electronics industry.[3,4]

1.1.1 Electronics miniaturization

The Si based-electronics reached the maturity and stability in this point, requiring from engineering improvements to keep evolving. Thus, Gordon Moore foretold the electronics evolution by observing the evolution tendency, which result in the postulation of the famous Moore's law.[5] The prediction was that the number of components of an IC would grow exponentially, which proved to be accurate as it can be observed in Figure 3.

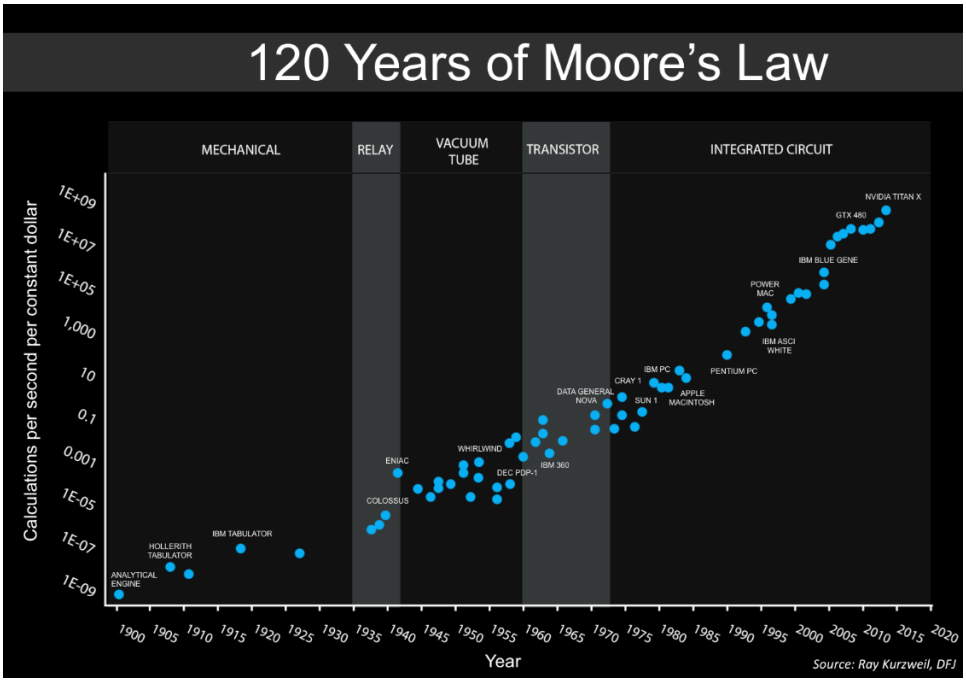

Figure 3. Moore's law graph extracted from https://medium.com/stoned-immaculate.

As it was predicted, the industry started a process of miniaturization of the components in ICs in order to increase the benefits. This process required a change in the type of transistors used in the ICs, which until that moment were the BJTs. So, the industry developed a new transistor technology which allowed the necessary improvements in the ICs performance. The new type of transistor was the metal-oxide-semiconductor field-effect transistor (MOSFET), which scheme is shown in Figure 4. Compare with the previous technology, MOSFETs were slightly slower in the beginning. Despite this inconvenient, they facilitated the miniaturization process

which provoked an increase in the transistors circuit density, leading to a drop in the fabrication cost.[6]

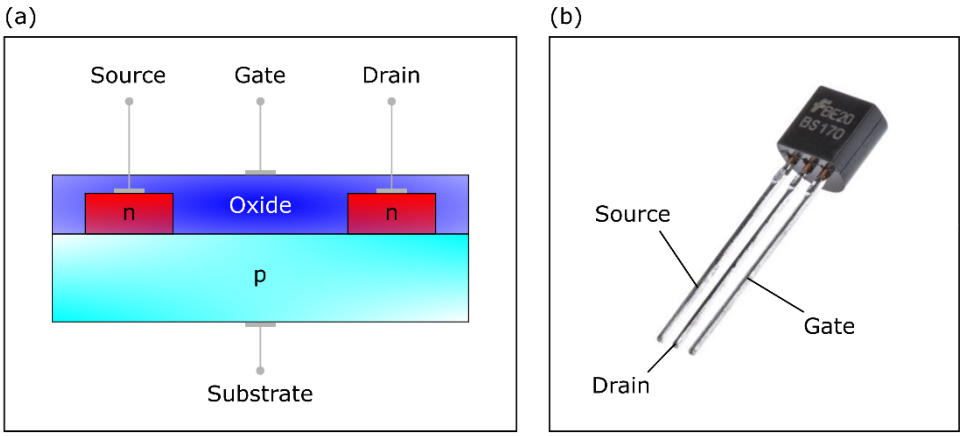

Figure 4. (a) Schematic of a metal-oxide-semiconductor field-effect transistor (MOSFET), with the main components marked. (b) Photo of a MOSFET real model sold in the market with the three electrodes labelled.

The MOSFET paved the path to the main IC technology currently used, the complementary-MOS (CMOS) integrated circuits. CMOS are a highly energy-efficient IC based on MOSFET. Thus, the high efficiency of the CMOS allowed the improvement of the power density of the IC thanks to the implementation of higher number of components. Despite the emergence of this new technology led to an increase in the cost of the facilities for manufacturing the electronic components, the result was a continuous decrease in the transistor cost over the last 50 years.

However, the trend is slowing down lately due to the issues that have been arising from the miniaturization of the transistors. The small gate lengths achieved by the industry have coupled problems with the OFF state current and the ON/OFF ratio of the components.[7,8] These two issues can result in the overheating of the ICs, which can even produce the burned down of the components. So, the engineers and researchers are looking for alternatives to the miniaturization for continuing the improvement in the performance of electronic devices.

1.1.2 Beyond Moore's law

The new advances in the field started from including other processes in the implementation of transistors to the current CMOS technology. The first change introduced was the used of strained Si,[8,9] which allow higher mobilities, but the underlying problem was the same and required from other strategies.

Until the moment, the CMOS were based on planar architectures which required from miniaturizing the elements in order to introduce more of them for increasing the power density. Another new approach consisted in reducing the space between components, mounting them each time closer. Researchers knew that this process was just a temporary solution because of the increase of parasitic resistance and capacitance when the space between the components is reduced.[10–12]

Another approach for solving this problem appeared, the scale length theory emerged as a new tool for continuing the scaling down. The main claim is that the transistor's electrostatic integrity at certain length depends on the gate/channel geometry, thicknesses and dielectric constant. So, a reduction in the gate length should be followed by a decrease in the channel thickness.[13,14] The necessity of thin channels triggered the research of new semiconducting materials in which the transport properties do not degrade with the reduction of thickness like in the Si.

The 2D semiconductors arose as a good option for substituting the Si when the thickness reduction provoked a degradation in the electrical properties of the channel.[15,16] In 2D semiconductors, the characteristic structural composition allows them to keep their transport properties down to the monolayer. Thus, 2D materials have a general structure in which there is a plane form by atoms linked by strong forces (covalent bonds) and the planes are linked between them by van der Waals interactions. So, it is possible to separate the different planes of the material until reaching the limit of one plane or a monolayer of that material. Moreover, the layers or planes maintain the electrical properties because of the integrity of the main bones of the structure remain invariable.[17]

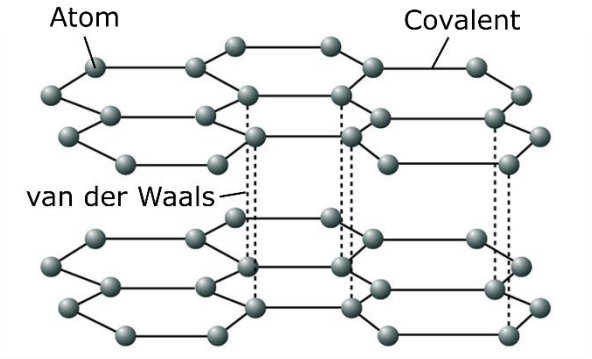

Figure 5. Atomic scheme of the main structure of a 2D material. In one plane, the atoms are bonded by covalent forces while in the perpendicular direction there are van der Waals interactions between the atoms.

Along with the study of new materials, other strategies are considered to improve the efficiency in order to increase the power of the electronic devices. As we mentioned before, the first step for overcoming the issues with the CMOS scaling down was the used of strained Si, so studying the change of the strained 2D semiconductors properties was an obvious path to follow for the research.[18,19] We discuss about this topic in the next section, how the strain engineering allows us to obtain different electronic behaviours in the semiconductors.[20]

Apart of the study of new materials and properties, the community is considering another strategy for solving the issues of the current CMOS technology, the implementation of more than one functionality per component. Current transistors use the field effect as the only tuning knob for creating different responses to the electric field, obtaining two possible states (ON and OFF). If the components have more than one tuning knob, the number of states in that component increases. So, the functionality of each component is higher, allowing a bigger number of responses and degrees of freedom. In the case of 2D semiconductors, there are several properties that can act as a knob, creating new research fields like valleytronics[21,22] or spintronics.[23,24] Here, we focus in the use of strain in 2D semiconductors, not only for changing the characteristics of the channel, but also for introducing it as an external tuning knob.

1.2 Strain engineering of semiconducting materials

In the previous section, we commented that one of the strategies followed for the successful continuation of the scaling down of the CMOS was the introduction of strained Si in the MOSFETs. The strain engineering allows one induce changes in the optoelectronic behaviour of a material by distorting its structure.[8]

Apart of the Si, strain engineering is been used in several semiconducting materials in order to modify their characteristics for the different requirements of the technological advances. However, strain engineering is applied in very different ways depending on the material. So, we divide this section in two parts for explaining the different approaches for 3D semiconductors, like the Si, and 2D semiconductors.

1.2.1 Strain engineering in 3D semiconductors

The strain engineering started as a demand for improving the mobility of the Si in order to overcome some of the issues found during the scaling down of the CMOS. The introduction of strain in the Si lattice produces a huge increase of the Si transport mobility, [9,25,26] even bigger than other high- mobility III-V semiconductors. There are two main types of strain that can be introduced in the Si lattices, tensile or compressive. Each type leads to an increment in the holes or electrons mobilities, allowing us to adjust the electronic behaviour to the needs of the devices.[27]

Both possibilities of strain can be usually achieved by using the same method, controlled growth of the material. The technique consists in the epitaxial growth of Si on a substrate, which is usually another Si based material, with a lattice mismatch with the pristine Si lattice.[28] In the case of tensile strain, SiGe substrate is usually employed for obtaining an increase in the electron mobility. The increment of holes mobility is accomplished by using SiC as a substrate for the growing process, which introduces a compressive strain to the Si lattice.

This is one of the methods commonly used for introducing strain in the lattices of 3D semiconductors. The changes introduced in the interatomic distances of the materials result in a modification of their physical properties. The strain allows us to engineer the band structure of the semiconductors, adjusting the bandgap energy of the material. Thus, biaxial strain has similar effects in Ge and Si carrier mobilities while uniaxial compression provokes changes in Ge mobility along a bigger strain

range.[29] Another example of the different changes that can introduce the strain engineering in materials is the increase in the mobility of GaAs under biaxial strain, while the uniaxial strain produces increase, saturation and decrease of the carrier mobility.[29] These methods usually achieve a strain level of 1.5% in Si and similar low strain levels in other semiconductors. Above these levels, the 3D semiconductors cannot hold the strain because it produces cracks in the areas with defects or dangling bonds.

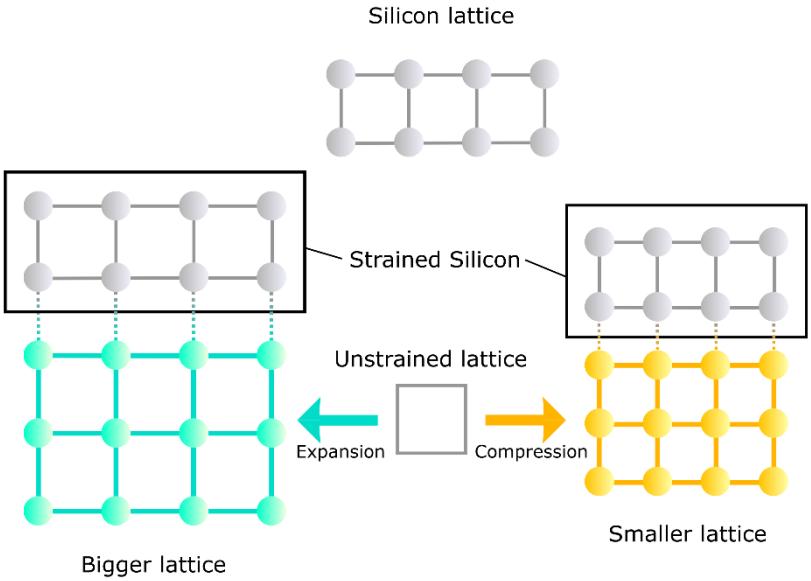

Figure 6. The silicon lattice can be strained by growing the material on substrates with different lattice parameters. The silicon grown on materials with bigger or smaller lattices, adjusts the distance between the Si atoms in the interface plane for matching the lattice parameter of the substrate while maintaining the same stacked distance of the unstrained silicon.

1.2.2 Strain engineering in 2D semiconductors

In 2D semiconductors, the strain can be introduced in the materials with a big variety of techniques, besides of the previous one, thanks to the characteristic mechanical properties of these materials. Unlike 3D semiconductors, 2D semiconductors have a small number of defects, which allow them to hold higher values of strain without breaking. Thus, the fracture point in brittle materials depends on the intrinsic strength

of the atomic bonds and not on the presence of defects. So, the predicted value for the ideal breaking point is around 1/9 of the Young's modulus.[30] In 2D materials, the real breaking value is very close to the ideal predicted value thanks to their structural characteristics.

1.2.2.1 Techniques for introducing strain

Thanks to the flexibility of 2D semiconductors, there are more techniques for applying strain than the one used for 3D semiconductors. Here, we explain the main five methods used for strain engineering: bending of flexible substrates, elongating an elastic substrate, piezoelectric stretching, substrate thermal expansion and controlled wrinkling.[18,20]

The first technique described here is commonly used for achieving uniaxial tensile strain in 2D materials. Thus, the 2D semiconductor is deposited in a flexible substrate that can be easily bent. When the flexible substrate with the 2D semiconductor is bent, the surface of the substrate is stretched like in Figure 7(a), transferring that stretch to the 2D semiconductor. The strain is transferred from the substrate to the material due to the van der Waals interactions established between substrate and the 2D semiconductor. Moreover, the slippage of the material while stretching the substrate is avoided by the van der Waals forces.

A similar method which allows to apply the strain homogeneously is the elongation of the flexible substrate. As mentioned in the previous technique, the 2D semiconductor is deposited on the flexible substrate for stretching it as shown in Figure 7(b). However, the substrate is elongated instead of bent, which produces a homogeneous tensile strain in the 2D semiconductor. Again, the strain is transferred thanks to the van der Waals interactions between the interface of the substrate and the 2D semiconductor.

The piezoelectric stretching is carried out by transferring the 2D semiconductor on a piezoelectric substrate. The piezoelectricity of the substrate allows us to produce mechanical deformations in the substrate by applying an electric field as shown in Figure 7(c). So, these mechanical changes in the substrate are transduced to the 2D semiconductor thanks to the same mechanism previously explained. This method can be used for producing different types of strain, depending on the substrate

characteristics and the voltage applied. For example, homogeneous compressive strain was achieved using this technique.

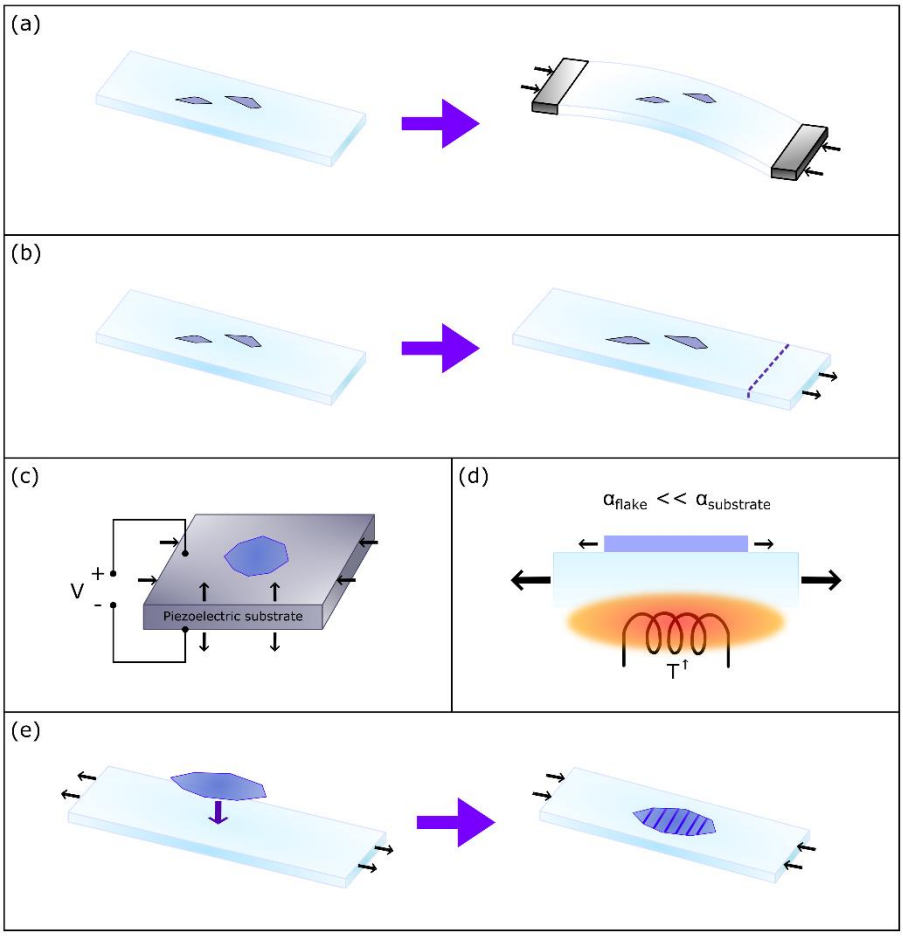

Figure 7. (a) Flexible substrate with transferred flakes can be bent by stretching the edges of the substrate. (b) Flexible substrate with transferred flakes can be expanded by elongating the edges of the substrate. (c) Piezoelectric substrate with transferred flake can be strained in two different directions (one of them will be stretched and the other one will be expanded) by applying a voltage difference as in the image. (d) Flexible substrate can be expanded/stretched by modulating the temperature, the flake transferred on the surface has lower thermal coefficient, so the bigger expansion of the substrate produces strain in the flake. (e) The flexible substrate is expanded while the flake is being transferred so once the strain is release from the substrate, wrinkles appear in the surface of the flake with certain amplitude and periodicity.

Another different technique used for strain engineering 2D materials is the exploitation of the thermal expansion mismatch between the substrate and the 2D material. For performing strain, the substrate where the 2D semiconductor is transferred must have a bigger thermal coefficient than the 2D semiconductor. So, the strain is achieved by heating up/cooling down the substrate, which produces an expansion/contraction of the substrate. On the other hand, the 2D semiconductor is not stretched due to the negative thermal coefficient. These two facts provoke a tensile/compressive biaxial strain in the 2D semiconductor as shown in Figure 7(d). This technique will be used along this thesis for performing the main experiments described in Chapter 4.

The last method discussed in this section is the controlled wrinkling of 2D semiconductors, which allows the production of strongly localized anisotropic strain. In this method, we bend or elongate a flexible substrate similarly to the techniques described in the beginning of the section. Once the substrate is stretched, the 2D semiconductor is deposited on it. Then, we release the strain from the substrate, producing a compressive strain in the 2D semiconductor. This compression produces ripples or wrinkles (depending on the initial strain of the substrate) in the 2D material thanks to the phenomena of the buckling-induced rippling or wrinkling. So, we have areas of the 2D semiconductor with different values of strain. A scheme of the process is shown in Figure 7(e).

1.2.2.2 Modulation of physical properties

The introduction of strain in the lattice of a 2D material produces changes in the structural arrangement of the material, causing differences in the interatomic distances regarding the natural ones. The first consequence is a modification of the band structure and the bandgap of the material in the strained region.[20] On the other hand, the behaviour of different 2D materials under the application of mechanical strain differs from each other, appearing different properties depending on the material.

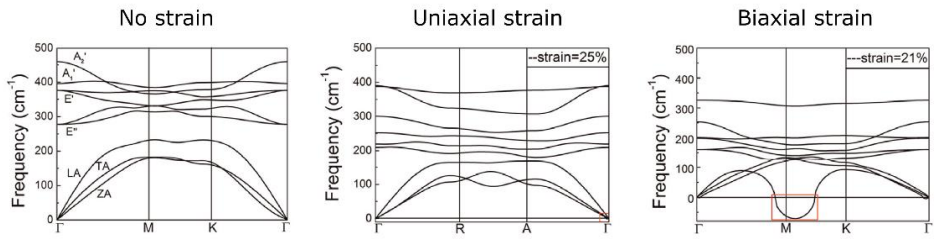

Figure 8. Band structure of 1L-MoS_2 when no strain is applied, 25% of uniaxial strain is applied and 21% of biaxial strain is applied. The graphs are extracted from the work of Miao *et al.*[31]

The modification of the band structure can easily yield to a modification of the electrical characteristics of the 2D material. One example is the piezo resistive effect that appears in MoS_2 and black phosphorus.[32,33] So, the conductance of the material can be easily tuned by the application of strain. In the case of MoS_2, in-plane strain increases the electrical conductivity while in the black phosphorus (anisotropic material) the strain allows to choose the preferred conductance direction.

Strain can also trigger different magnetic properties in 2D materials or enhance the already existent magnetic characteristics. MoS_2 magnetization can be modified with the application of strain, increasing in the case of 1T structure and appearing in the case of 2H structure.[34] $ReSe_2$ is another 2D material which magnetic properties are modify in the presence of strain. Under wrinkle formation, this material magnetic moment increases, showing a stable magnetic state.[35] On the other hand, pseudomagnetic characteristics appear in graphene upon strain, showing a pseudo quantum Hall effect.[36]

Another important change operated in 2D materials under strain is the modification of the optical properties, which are directly related with the band structure of the materials. One of the best examples of the transformation of the optical characteristics occurs in the transition metal dichalcogenides. It will be better explained in the next chapter, but these materials Raman modes and photoluminescence signals shift in energy when strain is applied to the samples.[37] Some good examples can be observed in the different experiments of Conley *et al*., Castellanos *et al*. or Frisenda *et al*. among other authors.[38–42] Figure 9 illustrates an example of optical changes in MoS_2. Here, we show the results of the Conley's photoluminescence experiments, in which the application of strain produces a shift

in the excitonic energies of the material.[38] Likewise, Frisenda's work will have a high impact in the development of this thesis (as will be mentioned in the next Section).[40] In this work, the author shows how the strain affects the optical properties of the most common four TMDCs (MoS_2, $MoSe_2$, WS_2 and WSe_2).

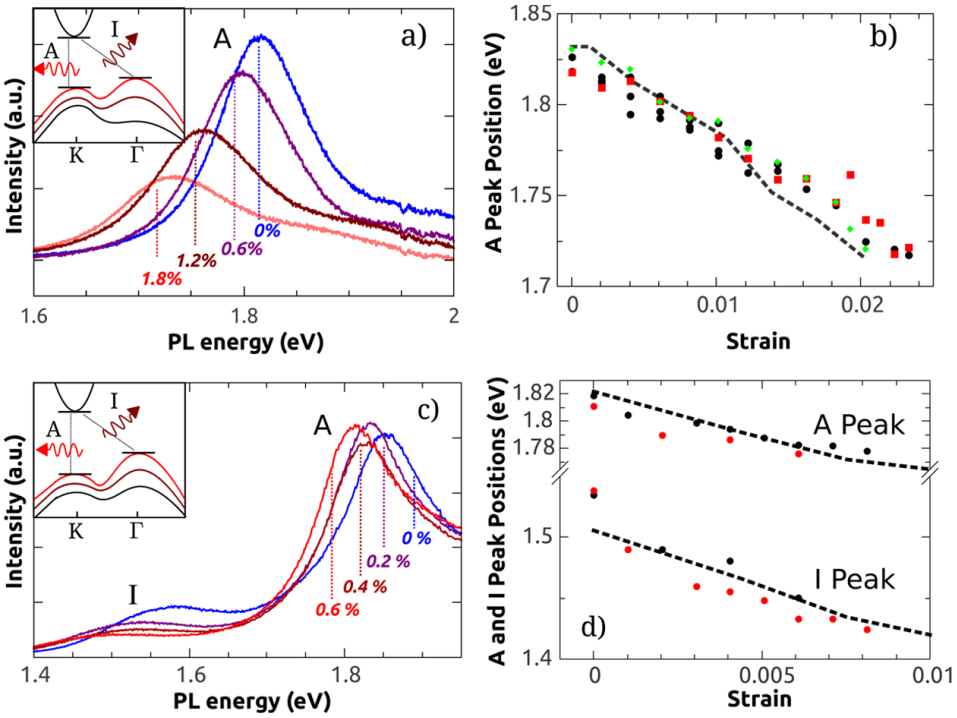

Figure 9. Image extracted from Conley's experiments.[38] a) and c) show the photoluminescence spectra of 1L-MoS_2 (a) and 2L-MoS_2 (c) under different levels of strain applied. b) and d) illustrate the energies of the excitonic peaks for each level of strain, in which the shift of the peaks can be observed.

On the other hand, the optical signals of 2D materials can also be enhance by using the funnel effect, in which the anisotropic strain produces an increment in the photogenerated excitons in the most strained area.[43] This funnel effect is also present in inverse form in black phosphorus, in which the photogenerated excitons decrease in the most strained area.[44]

The thermal conductivity of 2D materials is also dependent on the strain level of the material. An interesting case is the graphene and graphite thermal conductivities,

which behaviour differs from the monolayer to the multilayer. The tensile strain decreases the thermal conductivity in monolayer graphene and increases it in multilayer graphene and graphite.[45] In defect-free MoS_2, strain (tensile and compressive strain) always produces a reduction in the thermal conductivity, being stronger the effect for tensile strain.[46]

Finally, strain can tune the catalytic properties of the 2D materials or the interactions in van der Waals stacks of 2D materials. For example, the photocatalytic characteristics are modified by strain due to the bandgap tuning produced in the materials.[47] Another example is the changes in the interlayer distance of two graphene layers stacked under compressive strain, which yields to an increase of the optical transition energy.[48] The interaction changes can be introduced even inside the material, producing phase transitions by applying strain to the material. One example is the transition from a direct bandgap semiconductor to indirect bandgap semiconductor of MoS_2 under the application of >1% strain and the semiconductor to metal transition in the presence of 10%-15% of strain.[49,50]

1.3 Straintronics in 2D materials

As we explained in the previous section, there are several techniques that allow us to apply strain in 2D semiconductors, unlike in 3D semiconductors. Moreover, these techniques are in majority reversible, which means that we can apply and release strain as demand. Consequently, we can tune the physical properties of 2D semiconductors in a reversible way. As it was previously demonstrated by Frisenda *et al*., the time scale for the modification of the optical characteristics in 2D materials is in the order of seconds.[40] So, the modification of the band structure and the consequences of the application of strain take place in a short period of time in the material.

The importance of the reversibility of the changes and the time scale in which they take place lies on the possibility of implementing strain in operative devices. The main idea of straintronics is being able to use strain as another external tuning knob in a device in order to increase the functionality of each device. Thus, this use of the devices will allow to augment the different functionalities of the CMOS technology.

Until now, it has been proposed different concepts of devices in which using straintronics. One example is the use of strain for inducing a pseudomagnetic field

in graphene devices.[51] Another concept device would use TMDCs with phase transitions propitiated by the application of strain. In this case, the phase of the 2D material (semiconductor-semimetal or direct-indirect bandgap for example) would be the property tuned by strain. There are already some examples in literature, in which different applications take advantage of the tunability that the strain in 2D materials offers. For example, several strain experiments in piezoelectric and piezoresistive devices are reviewed by Li. *et al*.[52] Likewise, some optical devices, as light emitting devices[53] or quantum emitters,[54] have shown their tunability under different strain conditions.

The major aim of this thesis is to develop a proof of concept device which can be operated by strain. Strain engineering has proven to be a powerful tool for tuning the properties of different 2D semiconductors, so strain can be used in devices made of 2D materials for changing the outcome of the device. The design of the device will be simple in order to better illustrate how it works and will use a well-studied 2D semiconductor. Thus, we use the work of Frisenda *et al.* as starting point for developing this thesis.

The response of the photodetector depends on the absorption spectrum of the semiconductor channel. In our case, we will use MoS_2 as semiconductor channel, which absorbance can be tuned by using strain. So, this device can easily lead to a straintronic application. For applying strain to the 2D semiconductors, Frisenda uses the thermal mismatch between a polymeric substrate and the 2D semiconductors. So, this method can be easily implemented in our photodetector. This proof of concept device will show the possibilities of straintronics for improving the already existing devices and implementing new concept devices.

1.4 This thesis

As explained in the previous section, the main goal of this thesis is to fabricate a proof-of-concept straintronic device. In order to reach this result, different optical and optoelectronic techniques have been studied or developed along this thesis. Some of the methods are well-known in the materials and/or electronics research, but their use in 2D semiconductors is not commonly studied.

The main optical techniques used along this thesis are explained in Chapter 2. Here, we introduce the use of Raman and photoluminescence spectroscopies for studying

the main optical properties of 2D materials. After these techniques, we explain two characteristic methods for measuring optical properties in 2D materials. One of them is the micro-reflectance/transmittance spectroscopy, which was developed in our laboratory for obtaining absorbance information of 2D materials in the visible light spectrum. The other technique allows us to establish the thickness of the material by calibrating the optical transmission.

The Chapter 3 is devoted to the review of the techniques and methods used for making electrical contacts to 2D materials. The process for performing electrical measurements usually requires of three steps: fabrication of electrodes, 2D material transfer and contacting of electrodes. There are several ways of performing these steps that are described in the Chapter, including a new technique developed during this thesis.

Finally, the Chapter 4 of the thesis gathers the information about all the experiments performed in order to achieve a straintronic device. Thus, the fabrication of the devices is explained, together with the optical measurements to test the changes in the optical performance of the devices. Likewise, the optoelectrical response of the devices is tested in different type of experiments to show their behaviour under strain. So, proof-of-concept straintronic devices are successfully developed in this thesis, proving their feasibility for a new generation of electronic components.

References

1. Bardeen, J. & Brattain, W. H. The transistor, a semi-conductor triode. *Physical Review* **74**, 230–231 (1948).
2. Gatos, H. C. Semiconductor electronics and the birth of the modern science of surfaces. *Surf. Sci.* **299**–**300**, 1–23 (1994).
3. Khan, H. N., Hounshell, D. A. & Fuchs, E. R. H. Science and research policy at the end of Moore's law. *Nat. Electron.* **1**, 14–21 (2018).
4. Schaller, R. R. Moore's law: past, present, and future. *IEEE Spectr.* **34**, 52–55, 57 (1997).
5. Moore, G. E. Cramming more components onto integrated circuits, Reprinted from Electronics, volume 38, number 8, April 19, 1965, pp.114 ff. *IEEE Solid-State Circuits Soc. Newsl.* **11**, 33–35 (2009).
6. Dennard, R. H. *et al.* Design of Ion-Implanted MOSFET's With Very Small Physical Dimensions. *IEEE J. Solid-State Circuits* **9**, 256–268 (1974).
7. Taur, Y., Wann, C. H. & Frank, D. J. 25 nm CMOS design considerations. in *Technical Digest - International Electron Devices Meeting* 789–792 (IEEE,

1998). doi:10.1109/iedm.1998.746474
8. Thompson, S. E. & Parthasarathy, S. Moore's law: the future of Si microelectronics. *Mater. Today* **9**, 20–25 (2006).
9. Thompson, S. *et al.* A 90 nm logic technology featuring 50 nm strained silicon channel transistors, 7 layers of Cu interconnects, low k ILD, and 1 um2 SRAM cell. in *Technical Digest - International Electron Devices Meeting* 61–64 (2002).
10. Mohapatra, N. R., Desai, M. P., Narendra, S. G. & Rao, V. R. Modeling of parasitic capacitances in deep submicrometer conventional and high-K dielectric MOS transistors. *IEEE Trans. Electron Devices* **50**, 959–966 (2003).
11. Dixit, A. *et al.* Analysis of the parasitic S/D resistance in multiple-gate FETs. *IEEE Trans. Electron Devices* **52**, 1132–1140 (2005).
12. Ng, K. K. & Lynch, W. T. The Impact of Intrinsic Series Resistance on MOSFET Scaling. *IEEE Trans. Electron Devices* **34**, 503–511 (1987).
13. Yan, R. H., Ourmazd, A. & Lee, K. F. Scaling the Si MOSFET: From Bulk to SOI to Bulk. *IEEE Trans. Electron Devices* **39**, 1704–1710 (1992).
14. Suzuki, K., Tanaka, T., Tosaka, Y., Horie, H. & Arimoto, Y. Scaling Theory for Double-Gate SOI MOSFET's. *IEEE Trans. Electron Devices* **40**, 2326–2329 (1993).
15. Frank, D. J., Taur, Y. & Wong, H. S. P. Generalized scale length for two-dimensional effects in MOSFET's. *IEEE Electron Device Lett.* **19**, 385–387 (1998).
16. Akinwande, D. *et al.* Graphene and two-dimensional materials for silicon technology. *Nature* **573**, 507–518 (2019).
17. Novoselov, K. S. *et al.* Two-dimensional atomic crystals. *Proc. Natl. Acad. Sci. U. S. A.* **102**, 10451–10453 (2005).
18. Sun, Y. & Liu, K. Strain engineering in functional 2-dimensional materials. *Journal of Applied Physics* **125**, 082402 (2019).
19. Dai, Z., Liu, L. & Zhang, Z. Strain Engineering of 2D Materials: Issues and Opportunities at the Interface. *Adv. Mater.* **31**, 1805417 (2019).
20. Roldán, R., Castellanos-Gomez, A., Cappelluti, E. & Guinea, F. Strain engineering in semiconducting two-dimensional crystals. *J. Phys. Condens. Matter* **27**, 313201 (2015).
21. Vitale, S. A. *et al.* Valleytronics: Opportunities, Challenges, and Paths Forward. *Small* **14**, 1801483 (2018).
22. Schaibley, J. R. *et al.* Valleytronics in 2D materials. *Nature Reviews Materials* **1**, 1–15 (2016).
23. Feng, Y. P. *et al.* Prospects of spintronics based on 2D materials. *Wiley Interdiscip. Rev. Comput. Mol. Sci.* **7**, e1313 (2017).
24. Han, W. Perspectives for spintronics in 2D materials. *APL Mater.* **4**, 032401 (2016).
25. Welser, J., Hoyt, J. L., Takagi, S. & Gibbons, J. F. Strain dependence of the

performance enhancement in strained-Si n-MOSFETs. in *Technical Digest - International Electron Devices Meeting* 373–376 (IEEE, 1994).
26. Rim, K., Hoyt, J. L. & Gibbons, J. F. Fabrication and analysis of deep submicron strained-Si N-MOSFET's. *IEEE Trans. Electron Devices* **47**, 1406–1415 (2000).
27. Sun, Y., Thompson, S. E. & Nishida, T. Physics of strain effects in semiconductors and metal-oxide-semiconductor field-effect transistors. *J. Appl. Phys.* **101**, 104503 (2007).
28. Delhougne, R. *et al.* Selective epitaxial deposition of strained silicon: A simple and effective method for fabricating high performance MOSFET devices. *Solid. State. Electron.* **48**, 1307–1316 (2004).
29. Chu, M., Sun, Y., Aghoram, U. & Thompson, S. E. Strain: A Solution for Higher Carrier Mobility in Nanoscale MOSFETs. *Annu. Rev. Mater. Res.* **39**, 203–229 (2009).
30. Griffits, A. A. VI. The phenomena of rupture and flow in solids. *Philos. Trans. R. Soc. London. Ser. A, Contain. Pap. a Math. or Phys. Character* **221**, 163–198 (1921).
31. Miao, Y. P., Ma, F., Huang, Y. H. & Xu, K. W. Strain effects on electronic states and lattice vibration of monolayer MoS2. *Phys. E Low-Dimensional Syst. Nanostructures* **71**, 1–6 (2015).
32. Fei, R. & Yang, L. Strain-Engineering the Anisotropic Electrical Conductance of Few-Layer Black Phosphorus. *Nano Lett.* **14**, 2884–2889 (2014).
33. Manzeli, S., Allain, A., Ghadimi, A. & Kis, A. Piezoresistivity and Strain-induced Band Gap Tuning in Atomically Thin MoS $_2$. *Nano Lett.* **15**, 5330–5335 (2015).
34. Xu, W., Yan, S. & Qiao, W. Magnetism in monolayer 1T-MoS2 and 1T-MoS2H tuned by strain. *RSC Adv.* **8**, 8435–8441 (2018).
35. Meng, M. *et al.* Magnetism induced by cationic defect in monolayer ReSe 2 controlled by strain engineering. *Appl. Surf. Sci.* **425**, 696–701 (2017).
36. Guinea, F., Katsnelson, M. I. & Geim, A. K. Energy gaps and a zero-field quantum hall effect in graphene by strain engineering. *Nat. Phys.* **6**, 30–33 (2010).
37. Dadgar, A. M. *et al.* Strain Engineering and Raman Spectroscopy of Monolayer Transition Metal Dichalcogenides. *Chem. Mater.* **30**, 5148–5155 (2018).
38. Conley, H. J. *et al.* Bandgap engineering of strained monolayer and bilayer MoS2. *Nano Lett.* **13**, 3626–3630 (2013).
39. Castellanos-gomez, A. *et al.* Local Strain Engineering in Atomically Thin MoS_2. *Nano Lett.* **13**, 5361–5366 (2013).
40. Frisenda, R. *et al.* Biaxial strain tuning of the optical properties of single-layer transition metal dichalcogenides. *npj 2D Mater. Appl.* **1**, 10 (2017).
41. He, K., Poole, C., Mak, K. F. & Shan, J. Experimental demonstration of

continuous electronic structure tuning via strain in atomically thin MoS_2. *Nano Lett.* **13**, 2931–2936 (2013).
42. Zhu, C. R. *et al.* Strain tuning of optical emission energy and polarization in monolayer and bilayer MoS_2. *Phys. Rev. B - Condens. Matter Mater. Phys.* **88**, 121301 (2013).
43. Castellanos-Gomez, A. *et al.* Local strain engineering in atomically thin MoS_2. *Nano Lett.* **13**, 5361–6 (2013).
44. San-Jose, P., Parente, V., Guinea, F., Roldán, R. & Prada, E. Inverse funnel effect of excitons in strained black phosphorus. *Phys. Rev. X* **6**, 031046 (2016).
45. Kuang, Y., Lindsay, L. & Huang, B. Unusual Enhancement in Intrinsic Thermal Conductivity of Multilayer Graphene by Tensile Strains. *Nano Lett.* **15**, 6121–6127 (2015).
46. Ding, Z., Pei, Q. X., Jiang, J. W. & Zhang, Y. W. Manipulating the thermal conductivity of monolayer MoS_2 via lattice defect and strain engineering. *J. Phys. Chem. C* **119**, 16358–16365 (2015).
47. Putungan, D. B., Lin, S. H. & Kuo, J. L. A first-principles examination of conducting monolayer 1T′-MX_2 (M = Mo, W; X = S, Se, Te): Promising catalysts for hydrogen evolution reaction and its enhancement by strain. *Phys. Chem. Chem. Phys.* **17**, 21702–21708 (2015).
48. Del Corro, E. *et al.* Fine tuning of optical transition energy of twisted bilayer graphene via interlayer distance modulation. *Phys. Rev. B* **95**, 085138 (2017).
49. Kou, L. *et al.* Tuning magnetism and electronic phase transitions by strain and electric field in zigzag MoS_2 Nanoribbons. *J. Phys. Chem. Lett.* **3**, 2934–2941 (2012).
50. Yu, S., Xiong, H. D., Eshun, K., Yuan, H. & Li, Q. Phase transition, effective mass and carrier mobility of MoS_2 monolayer under tensile strain. *Appl. Surf. Sci.* **325**, 27–32 (2015).
51. Low, T. & Guinea, F. Strain-induced pseudomagnetic field for novel graphene electronics. *Nano Lett.* **10**, 3551–3554 (2010).
52. Li, F. *et al.* Recent Advances in Strain-Induced Piezoelectric and Piezoresistive Effect-Engineered 2D Semiconductors for Adaptive Electronics and Optoelectronics. *Nano-Micro Lett.* **1**, 3 (2020).
53. Andrzejewski, D. *et al.* Flexible Large-Area Light-Emitting Devices Based on WS_2 Monolayers. *Adv. Opt. Mater.* 2000694 (2020).
54. Mendelson, N., Doherty, M., Toth, M., Aharonovich, I. & Tran, T. T. Strain-Induced Modification of the Optical Characteristics of Quantum Emitters in Hexagonal Boron Nitride. *Adv. Mater.* **32**, 1908316 (2020).

2. Isolation and optical characterization of 2D materials

2.1 Introduction

The 2D materials has become a very broad and interesting research field thanks to the presence of intriguing physical phenomena that appear because of the low dimensionality of the materials.[1–5] The different optical techniques allow us to identify different 2D materials and determine the number of layers in a fast manner with a non-destructive approach. Most of the physic involved in 2D materials has consequences in the optical properties of these materials, making the optical characterization a key tool for disentangling the new information.[6–9] The optical techniques used in 2D materials allow to analyse the optical characteristics of the material without the damage of the samples.

The first techniques exposed are not exclusive from 2D materials research, the Raman and photoluminescence spectroscopies have been used in material science, chemistry and even biology for obtaining structural information about the compounds.[10–13] In the case of 2D materials, the changes due to the doping or the strain produce prominent modifications in the structure, which can be observed in the Raman and photoluminescence spectroscopies.[14,15]

After these two techniques, we introduce a method for obtaining the transmittance and differential reflectance spectra of 2D materials.[16] These measurements offer complementary spectral data about the materials, especially those with non-active Raman modes or photoluminescence features in the spectrum. Moreover, the differential reflectance and transmittance are related with the absorbance of the material, allowing us to obtain the absorbance spectral information.

Finally, we explain a simple optical method to extract the transmittance in different ranges of the spectrum of 2D materials.[17] The technique can be used for estimating the thickness of the samples before the transfer process, giving us control over the sample choice. We also calibrate the transmittance obtained by applying this method as a function of the number of layers for the TMDCs.

2.2 Isolation of 2D materials

In order to study the physical properties of 2D materials, we use a technique that allow us to isolate thin flakes of these materials. This technique is the mechanical exfoliation, which is introduced in this section.

On the other hand, the flakes need to be transfer to any type of substrate for performing different type of measurements. Here, we also explain the main techniques used for transferring 2D materials on the desired substrate.

2.2.1 Mechanical exfoliation

Novoselov and Geim isolated graphene for the first time by using the mechanical exfoliation or Scotch-tape method in 2004. Since then, the mechanical exfoliation spread among the 2D research community as a simple method for obtaining high quality samples.

The mechanical exfoliation of a 2D material requires from certain adhesive tape (Nitto tape SPV24 in our case) which allows us to extract pieces of crystal from the bulk material. The obtention of crystals from a bulk material is possible thanks to the weakness of the van der Waals forces between layers, which results in the easy delamination of 2D materials. In order to get thin crystals, we can use another piece of tape for re-exfoliating the adhesive tape with material.

Once the thickness of the material on the adhesive tape is appropriate, we re-exfoliate the tape with a piece of Gel-Film® (from Gel-Pak). Gel-Film® is made of polydimethylsiloxane (PDMS), which is a viscoelastic material that interacts with the 2D material by van der Waals forces. This last step is very useful for the all-dry deterministic transfer process, in which the lack of adhesive glue and the transparency of the Gel-Film® facilitate the transfer of the 2D material to a substrate.

2.2.2 Transfer of 2D materials on substrates

In order to study the optical properties (and the electrical properties later), it is usually necessary to transfer the exfoliated 2D material to another substrate. There are usually two main methods depending on the importance of the transfer location. In the case of a random flake transferred on a substrate with no special location, the

random transfer can be used. However, the deterministic transfer has to be applied for placing a chosen flake on a determined location.

2.2.2.1 Random transfer

The process of random transfer is quite simple and easy to follow. First, the bulk material is peeled off with a piece of adhesive tape (as explained in the previous section), so the exfoliated flakes need to be transfer from the tape to the chosen substrate. Thus, the piece of tape with flakes is adhered to the substrate surface and then it is raised very slowly in order to transfer the material. The flakes interact with the surface through van der Waals forces, remaining in the substrate when the tape is carefully picked up.

2.2.2.2 Deterministic transfer

This technique is usually followed by the fabrication of devices with 2D materials on pre-patterned electrodes (the methods for pre-patterning electrodes are explained in Chapter 3). In this case, the transfer process requires a technique that allows the accurate alignment of the flakes with the metallic electrodes. There are different deterministic transfer methods (PMMA carrying layer method, Elvacite® sacrificial layer, wedging transfer method, van der Waals pick-up transfer methods and PDMS deterministic transfer method),[18] being the technique used along this thesis based on a dry deterministic process with PDMS stamps.[19]

Figure 1 shows the deterministic transfer setup used in this thesis. The main parts of the setup are a zoom lens (Edmund Optics 89-862, 89-877, 89-878, 89-888, 89-903), which has a long working distance, and two micromanipulators, a XY stage (Optics Focus Solutions MAXY-B60L-13) with a rotation stage (Thorlabs MSRP01/M) for the substrate and a XYZ micro-stage (Optics Focus Solutions MAXY-60L) for handling the PDMS stamp. The zoom lens has a camera attached which is connected to a TV in order to monitor the transfer process. Moreover, the lens is mounted on a focussing stage, allowing us to change the focal distance. This setup allows us to determiniscally transfer the flakes previously exfoliated on PDMS (as previously explained) to any substrate with the process shown in Figure 2.

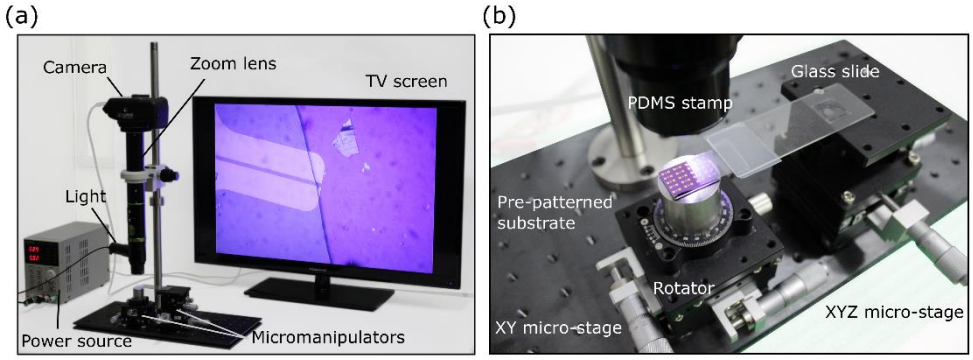

Figure 1. (a) Optical photo of the deterministic transfer setup. The main components of the system are indicated in the image. (b) Detail image of the manipulators of the setup while transferring a flake between Au electrodes.

First, we stick the substrate to the XY micro-stage, positioning it under the zoom lens. Then, the PDMS stamp with the flakes is attached to a glass slide with a piece of tape. The glass slide is placed in the XYZ micromanipulator, with the PDMS stamp positioned with the flakes facing towards the substrate. The transparency of the PDMS stamp allows us to observe the flake and the pre-patterned electrodes by changing the focus, enabling the alignment of the flake with respect to the electrodes. Once the flake is aligned with the electrodes as shown in Figure 2 Step 4, we slowly lower the PDMS stamp towards the substrate. Figure 2 Step 6 shows when the flake is in the same plane of the electrodes but the PDMS is still not adhered to the surface. We clearly see when the PDMS is stuck to the surface because the colours of the substrate and the flake change, as shown in Figure 2 Step 7. The next step requires to manipulate the XYZ micro-stage carefully to gently rise the PDMS stamp. We can easily monitor the peeling off process because it appears a meniscus (or front) at the interface between the region where the PDMS is still in contact with the substrate and that where the PDMS has been already peeled off as indicated in Figure 2 Step 8. When the meniscus is close to the flake, we decrease the speed of the peeling off process by controlling the Z micro-screw. The speed of the flake peeling off should be very low in order to leave the flake in the chosen position while detaching the PDMS. The transferred flake is shown in Figure 2 Step 12, in which we observe the accurate positioning of the flake between the electrodes.

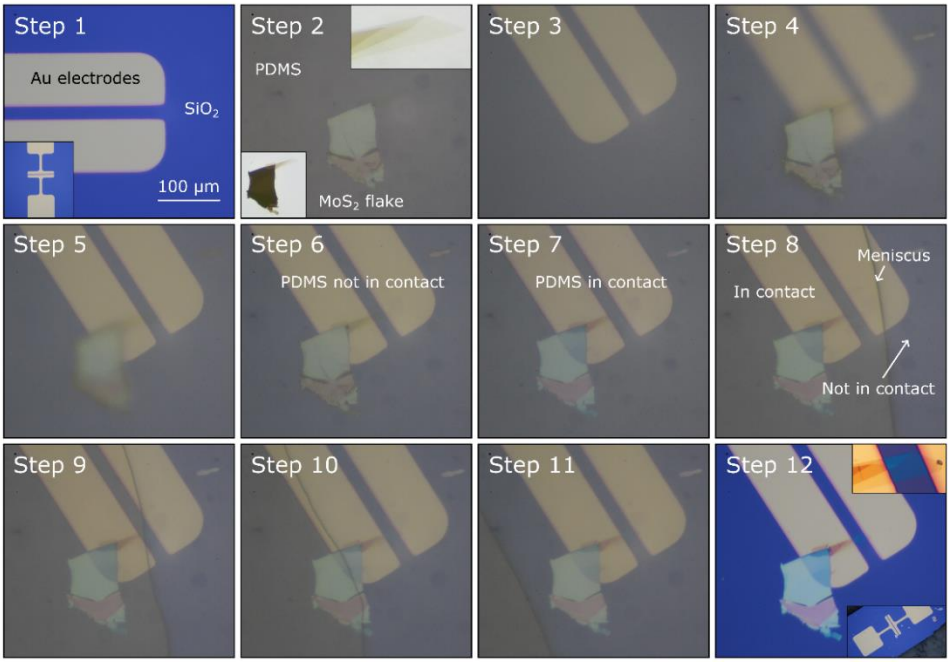

Figure 2. Optical images of the different steps of the deterministic transfer of a MoS_2 flake between Au electrodes.

2.3 Raman and photoluminescence spectroscopies

2.3.1 The technique

The Raman spectroscopy is an optical technique used in material science and chemistry to study the vibrational modes of molecules and crystals in solid or liquid form.[20] Moreover, it is usually used to provide information about the material structure, allowing us to identify the molecules and configurations. The main mechanism involved that allow us to study the optical properties of the material is the inelastic scattering of photons in the sample (Raman scattering). So, it is necessary to use a monochromatic light source to irradiate the sample in order to measure the inelastically scattered light. Thus, part of the light reflected by the sample shifts the energy after the interaction with the material. In the case of a shift to lower energies, the scattering is called Stokes while the scattering to higher energies is called anti-Stokes. So, both inelastic scattering processes together are the Raman scattering of the material. So, the Raman scattering occurs in the material

when there is a transition between two vibrational states of the molecules in which the electric dipole polarizability suffers a change.

On the other hand, the photoluminescence is a luminescence process in which the material irradiates light after exciting it with light of certain wavelength.[21] In the case of the most studied 2D materials, the luminescence is produced by the photoexcitation of electrons to a higher energy level. So, the same light source used for Raman spectroscopy might be suitable for performing photoluminescence measurements.

The typical Raman setup uses a laser to illuminate the sample with monochromatic light. After collecting the reflected light by the sample, the beam crosses a filter for eliminating the wavelength corresponding to the laser (Rayleigh scattering). Then, the inelastically scattered light (Raman scattering) is sent to the spectrometer for analysing the spectrum. Figure 3 shows the Raman setup used along this thesis, which incorporates a laser with a wavelength of 532 nm. The setup software allows us to select the integration time of the spectrometer and the intensity of the light beam (by applying different filters). We can also observe the sample and the light spot in order to focus the spot in the material surface to obtain accurate spectral information about the material.

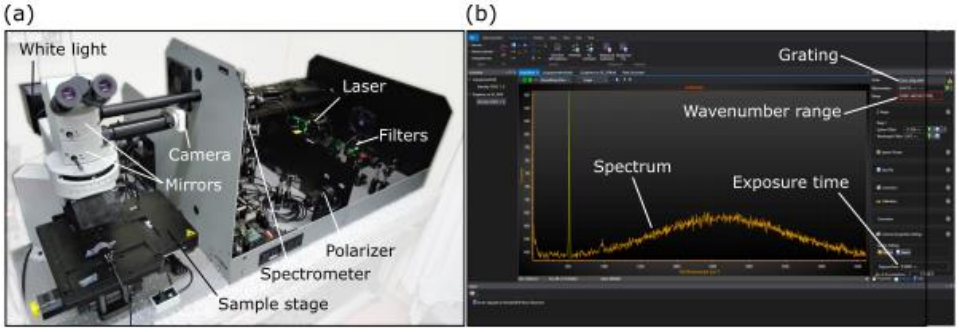

Figure 3. (a) Optical image of the Raman/photoluminescence setup, in which the main components of the system are highlighted. (b) Image of the software used for controlling the equipment during the measurements. The parameters shown are the main adjustable characteristics of the spectra recording.

2.3.2 Raman and photoluminescence in 2D materials

These techniques are a very important tool in the 2D material research field. The Raman spectrum provides information about the structure of the 2D material, from

which we can extract other data. Thus, the spectral signal allows us to deduce e material characteristics like the strain in the material, the doping or the quality of the material.

For example, the Raman spectroscopy helped to the development of the research in graphene, the first 2D material isolated and the most studied.[14] Graphene has two main Raman features, the G (~1580 cm^{-1}) and the 2D (~2670 cm^{-1}) modes; although another one can appear, the D (~1350 cm^{-1}) peak, as shown in Figure 4. The G peak comes from in-plane vibrations in the sp^2 atoms, so the doping (both, electrons and holes) produces a blueshift in the peak energy. Moreover, the strain also affects the energy of the G peak as well as the 2D peak. The 2D mode shows information about the stacking in the graphite, which is the reason why it changes with the strain. Finally, the D peak goes from no intensity for defect-free graphene to a continuously growing intensity for an increasing number of defects. Thus, the amount of defects in the samples is quantized by calculating the I_D/I_G.[1422]

The Raman modes are very useful in most of the 2D materials because the energies of the different modes usually depend on the thickness of the material. A good example in which this phenomenon appears is the black phosphorus. The black phosphorus Raman modes are the A^1_g (out-of-plane vibrations), B_{2g} (in-plane vibrations along the zigzag) and A^2_g (in-plane vibrations along the armchair), as it can be observed in the Figure 4.[23] The energies for the 1L black phosphorus or phosphorene are ~362.5 cm^{-1}, ~439.5 cm^{-1} and ~467.5 cm^{-1}, respectively; but their energies redshift for increasing number of layers until reaching ~359.5 cm^{-1}, ~435 cm^{-1} and ~462.5 cm^{-1} for the bulk material.[24–26]

In the case of TMDCs, the Raman modes also provide information about the thickness of the materials.[27,28] These materials are optically interesting because, apart from presenting several Raman modes, they show prominent photoluminescence peaks.[6,29] The excitonic resonances presented in TMDCs are the responsible of the photoluminescence in these materials.[30,31] Figure 4 shows the Raman modes and the photoluminescence of 1L $MoSe_2$, one of the 2D materials from the TMDC family.

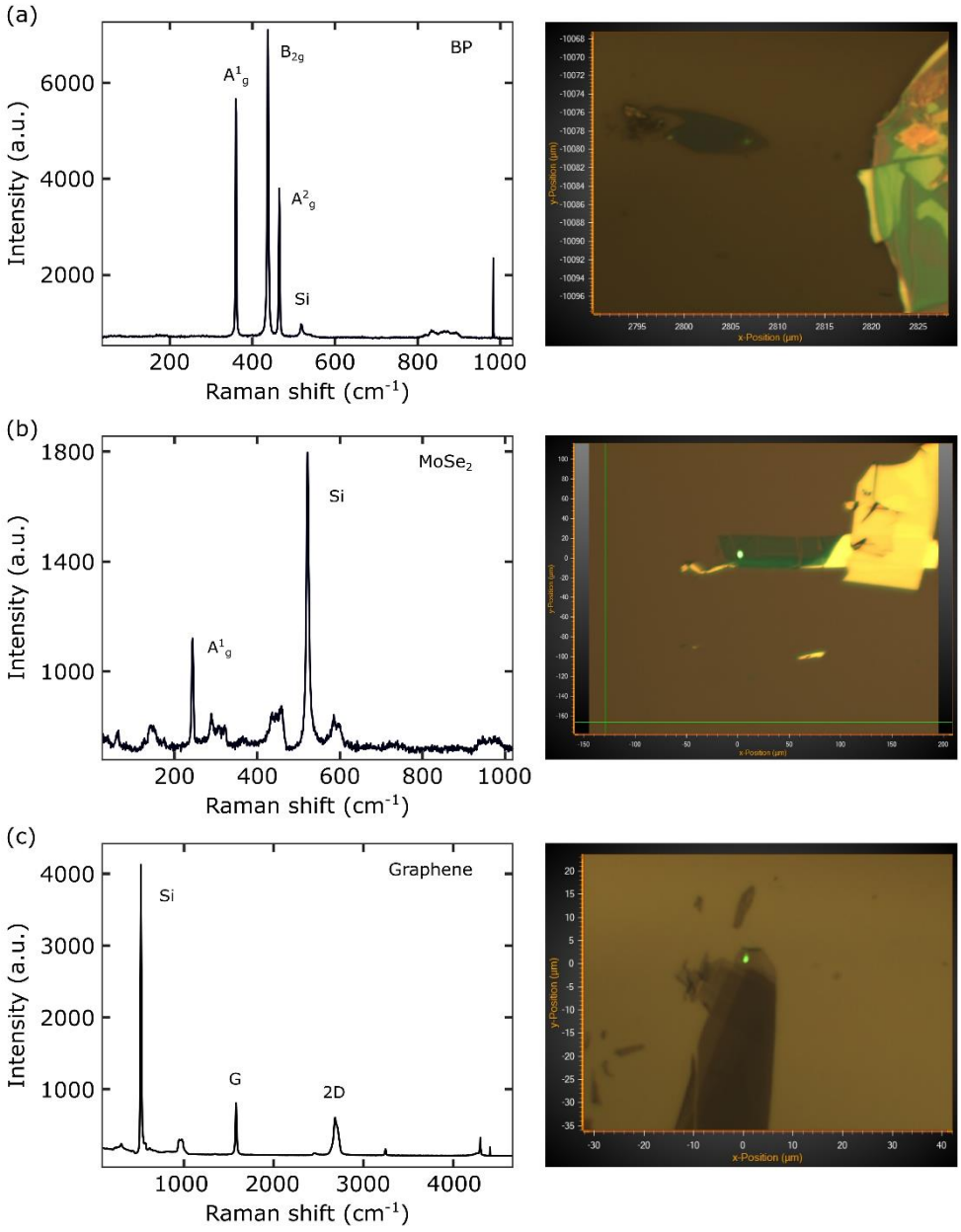

Figure 4. Raman spectra and optical images of the laser spot focused on the surface of (a) a black phosphorus flake, (b) a 1L-$MoSe_2$ flake and (c) a multilayer graphene flake.

2.3.3 MoS_2 Raman and photoluminescence dependency on the thickness

In this section, we focus on Raman and photoluminescence measurements of MoS_2, but this information can be extended to other TMDCs like the $MoSe_2$ shown in Figure 4. MoS_2 presents two main Raman modes, E^1_{2g} (opposite vibrations of two S atoms with respect to the Mo atom) and A_{1g} (out-of-plane vibrations of S atoms in opposite directions), and two photoluminescence peaks, corresponding to A and B excitonic resonances (these excitons appear due to interband recombination of electrons and holes at the K point of the Brillouin zone). As shown in Figure 5, the 1L MoS_2 Raman modes have energies of ~384.5 cm^{-1} for the E^1_{2g} and ~403 cm^{-1} for the A_{1g} phonons. However, the energies of the peaks change when increasing the number of layers, affecting the distance between the phonons energies as well.[32] This fact is easily observable in Figure 5, where the spectra are misplaced by 0.1 to facilitate the inspection.

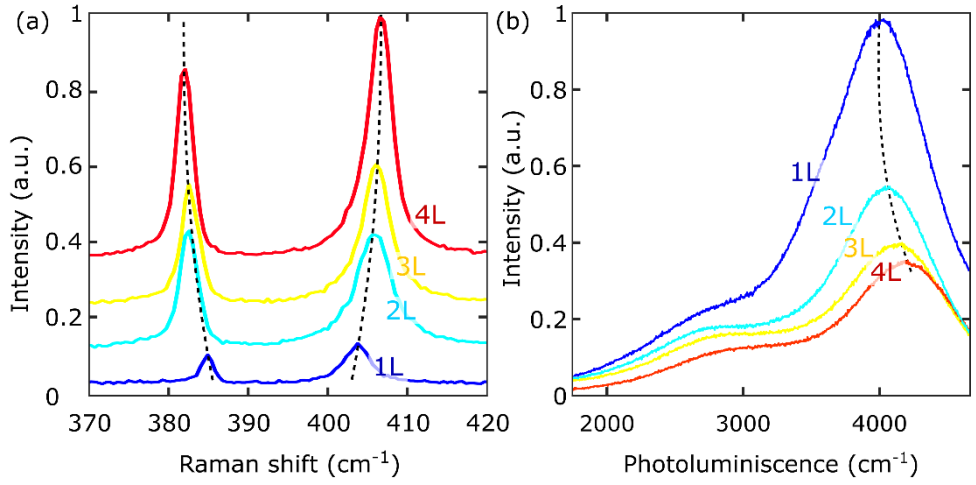

Figure 5. (a) Raman spectra of MoS_2 with 1L, 2L, 3L and 4L measured with a 532 nm excitation laser and vertically displaced 0.1. (b) Photoluminescence of MoS_2 with 1L, 2L, 3L and 4L measured with a 532 nm excitation.

Likewise, the A and B excitons energies and intensities are influenced by the thickness of the MoS_2 sample. So, the 1L MoS_2 energies for the excitons are 670 nm and 630 nm respectively, while the energies of the excitons decrease for increasing number of layers.[3,6] In the case of the excitonic resonances, the energies are not the only parameter affected by the number of layers, the intensity is highly dependent on the thickness too (see explanation below). Figure 5 shows the photoluminescence of MoS_2 samples with different thicknesses. Here, we can see a dramatic change in

the intensity of the peaks for 1L and the rest of the number of layers shown. When the bulk material is studied, it does not show signs of photoluminescence in comparison with the prominent photoluminescence of 1L MoS_2. The reason behind this difference is the transition from a direct bandgap semiconductor, in the case of 1L MoS_2, to an indirect bandgap semiconductor, for the MoS_2 with more than 1L.[3]

2.4 Microreflectance and transmittance spectroscopy

2.4.1 Introduction

As we previously mentioned, optical measurements are characterization techniques which allow us to collect a lot of information from the 2D materials without damaging them. The Raman spectroscopy and photoluminescence provide a fast way of obtaining the optical properties from the materials and determining the number of layers in the sample, as explained in the previous section. Nevertheless, the setup required for performing these studies is difficult to maintain, to operate and it is costly.

There are others complementary optical techniques which do not present these disadvantages. We are referring to the differential reflectance and transmittance spectroscopies, which also extract information of the optical characteristics along a wide range of energies of materials with non-active Raman modes or excitonic resonances.[16] The differential reflectance is intimately related to the absorbance of the material, so we can extract the absorbance spectrum from this measurement. The same setup used for these measurements can be used for extracting the transmittance spectrum, with a direct relation with the absorbance. Likewise, we can measure the optical contrast spectrum from the sample with respect to certain substrate.

In this section, we describe the setup used for performing the spectroscopic characterizations of 2D materials. The technique is explained using the TMDC family as example, providing a deeper information about the optical properties of these materials.

2.4.2 The system: components and how to set it up

The setup used for acquiring the micro-reflectance and transmittance spectra in 2D materials is shown in Figure 6(a). As it can be observed, the main part of the setup is a modified microscope (Motic BA310Met-T metallurgical microscope). The

modification introduced in the microscope to allow the spectroscopic measurements is situated in the trinocular, which image is shown in more detail in Figure 6(b). The light from the trinocular is divided in two different paths by connecting a 50:50 beam splitter for allowing to inspect through a camera and measure at the same time. The camera (AMScope MU1803) attached to the beam splitter receives half of the light intensity coming from the trinocular, while the other half of the intensity goes to the other connection of the beam splitter. In order to collect optical images from the samples, the camera is placed in the image plane of the optical system when the sample is focussed in the eyepieces for the 50x objective.

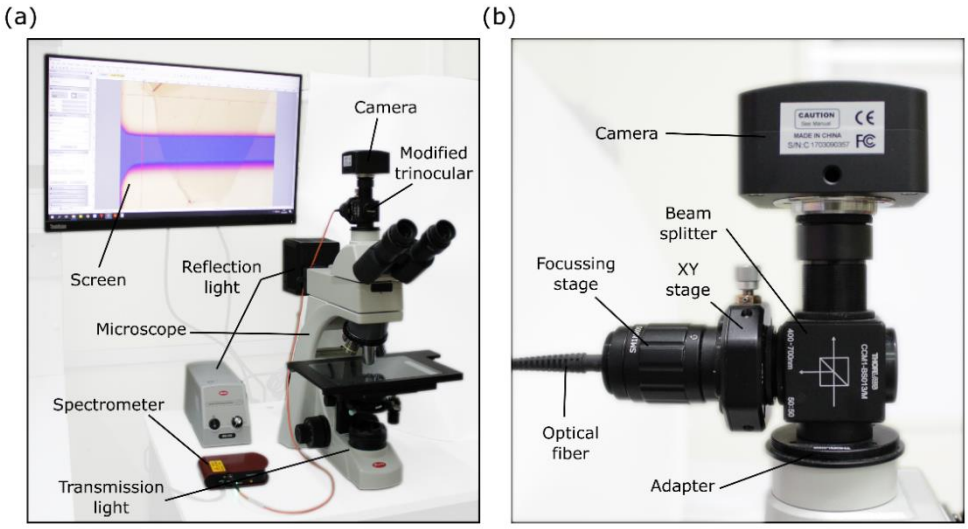

Figure 6. (a) Optical image of the micro-reflectance and transmittance setup with the main components marked. (b) Zoom in the modified trinocular of the setup pointing the components.

On the other connector of the beam splitter, we attached an optical fiber for collecting the light coming from the sample. The fiber is also connected to a CCD spectrometer (Thorlabs CCS200/M) in order to analyse the light spectrum recorded by the optical fiber. The fiber allows us to collect light from a small area of the image plane. In order to identify that area, we disconnect the fiber connector attached to the spectrometer and we connect it to a white fiber-coupled LED (Thorlabs MWWHF1). Once we turn on the illumination, a light spot (corresponding to the projection of the fiber core on the sample) can be observed through the camera, as shown in Figure 7(a). We focus the spot to ensure that both fiber core and camera are at the same image plane by adjusting the optical path with a focus stage. Thus, we determine the spot position and area, allowing us to mark it in the camera software for knowing the

collection area. In our setup, we use an optical fiber with a diameter of 105 µm, which corresponds to a collection spot size of 1 µm of diameter. The diameter size changes depending on the magnification of the objective used, being in our case a 50x objective. Moreover, we can easily modify this parameter by changing the core of the optical fiber used for collecting the light. The different sizes of the fiber cores result in a change of the light that our spectrometer is receiving.

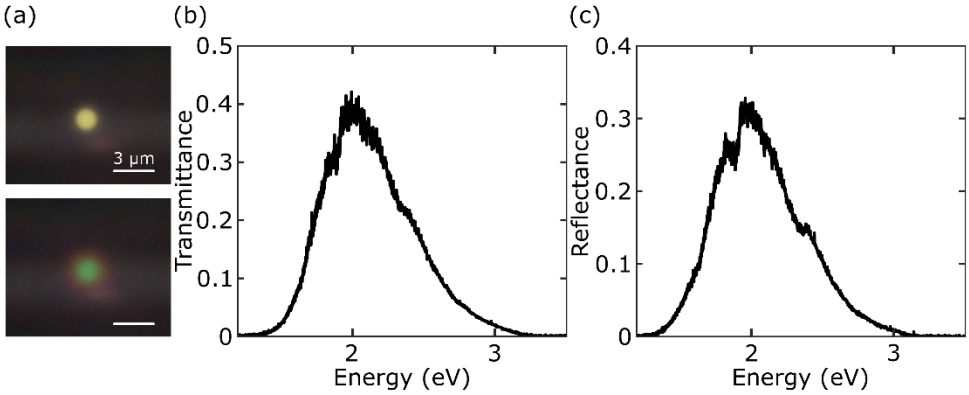

Figure 7. (a) Optical images of the illuminated spot from where the spectrometer is collecting the light. The first image the spot is focused in the image plane and the second one the spot is out of focus. (b) Spectrum of the microscope light in transmission mode at maximum intensity with an acquisition time of 4 s and averaging 5 spectra. (c) Spectrum of the microscope light in reflection mode at maximum intensity with an acquisition time of 4 s and averaging 5 spectra.

There are two different light sources (one for transmission mode and another one for reflection mode) in the system for measuring the samples spectra, both are white halogen lamps (halogen lamps incorporated in the Motic BA310Met-T microscope). The spectrum of this light source is centred in the usual wavelength range of study, providing us enough spectral information from 1.4 eV to 3 eV. Figure 7(b) shows the light spectra in transmission and reflection mode acquired with an integration time of 4 s and averaging 5 spectra, which allow us to observe the illumination spectral range.

2.4.3 Measuring micro-reflectance and transmittance spectra

Our setup is designed for measuring the transmittance and the differential reflectance or optical contrast spectra of 2D materials. In the case of transmittance, the sample is illuminated from the bottom with the transmission mode halogen lamp incorporated in the microscope. The light passes through the sample, which absorbs

part of it, and goes straight to the 50x microscope objective (situated in the Motic BA310Met-T microscope). Then, the light is collected by the fiber placed in the trinocular and send to the spectrometer. In order to obtain the transmittance spectrum, we need to acquire the spectrum in the sample and in the substrate. This proceed is necessary to calculate the transmission of the sample, which is directly related to the absorption of the sample, by:

$$T = \frac{S_{\text{sample}}}{S_{\text{substrate}}}$$

where T is the transmittance, S_{sample} is the spectrum recorded in the sample and $S_{\text{substrate}}$ is the spectrum measured in the substrate. Figure 8(a) shows the transmittance measurements performed in a 1L-MoS_2 sample. This measurement is very useful in the case of transparent substrates because of the direct relation between transmittance and absorbance.

On the other hand, a lot of samples are placed in non-transparent substrates, which require reflection mode measurements. The reflection mode light is used in this case to illuminate the sample from the top. By closing the field aperture of the microscope, we can reduce the stray light collected through the objective. This light goes to the fiber and it is sent to the spectrometer. This parameter is a differential quantity like the transmittance, so we require to measure the spectrum in the substrate and in the sample again. In this case, the relation between the reflectance and the absorption of the material is:[33,34]

$$R = \frac{S_{\text{sample}} - S_{\text{substrate}}}{S_{\text{sample}}} = \frac{4n}{n_0^2 - 1}\alpha(\lambda)$$

where R is the differential reflectance, S_{sample} is the spectrum recorded in the sample and $S_{\text{substrate}}$ is the spectrum measured in the substrate. The measurements on 1L-MoS_2 sample are shown in Figure 8(b). The optical contrast of the sample can be calculated as well from these measurements. The only difference is the formula used to calculate it:

$$OC = \frac{S_{\text{sample}} - S_{\text{substrate}}}{S_{\text{sample}} + S_{\text{substrate}}}$$

where *OC* is the optical contrast, S_{sample} is again the spectrum recorded in the sample and $S_{substrate}$ the spectrum measured in the substrate.

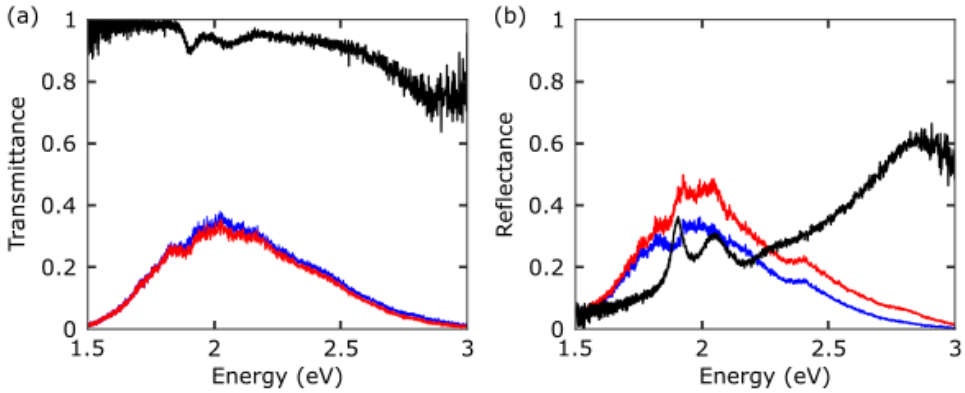

Figure 8. (a) Spectra in transmission mode of the light going through the sample (red), in this case a 1L-MoS_2, and the substrate (blue), which is PDMS. These data allow us to calculate the transmittance of the sample, resulting the black spectrum. (b) Spectra in reflection mode of the light going towards the sample (red), in this case a 1L-MoS_2, and the substrate (blue), which is PDMS. These data allow us to calculate the differential reflectance of the sample, resulting the black spectrum.

2.4.4 TMDCs differential reflectance and transmittance spectra

These techniques allow us to extract spectral information about the optical properties of 2D materials with a measurement easy to perform. In fact, they allow us to observe excitonic resonances in materials like TMDCs.[30,31] Figure 9 shows the transmittance spectra of the four most common TMDCs (MoS_2, $MoSe_2$, WS_2 and WSe_2). All the spectra present very characteristic peaks that are highlighted in the image, these are the different excitonic resonances from the TMDCs. These excitonic resonances arise due to the presence of spontaneous recombination of electrons and holes in the K point of the Brillouin zone of these materials. It is a very striking fact that the excitons are visible at room temperature, which is an important property of these materials. The excitons energies in 2D TMDCs are usually used as a tool for determining the number of layers of these materials. These energies change with the number of layers, providing an accurate method to establish the material thickness.

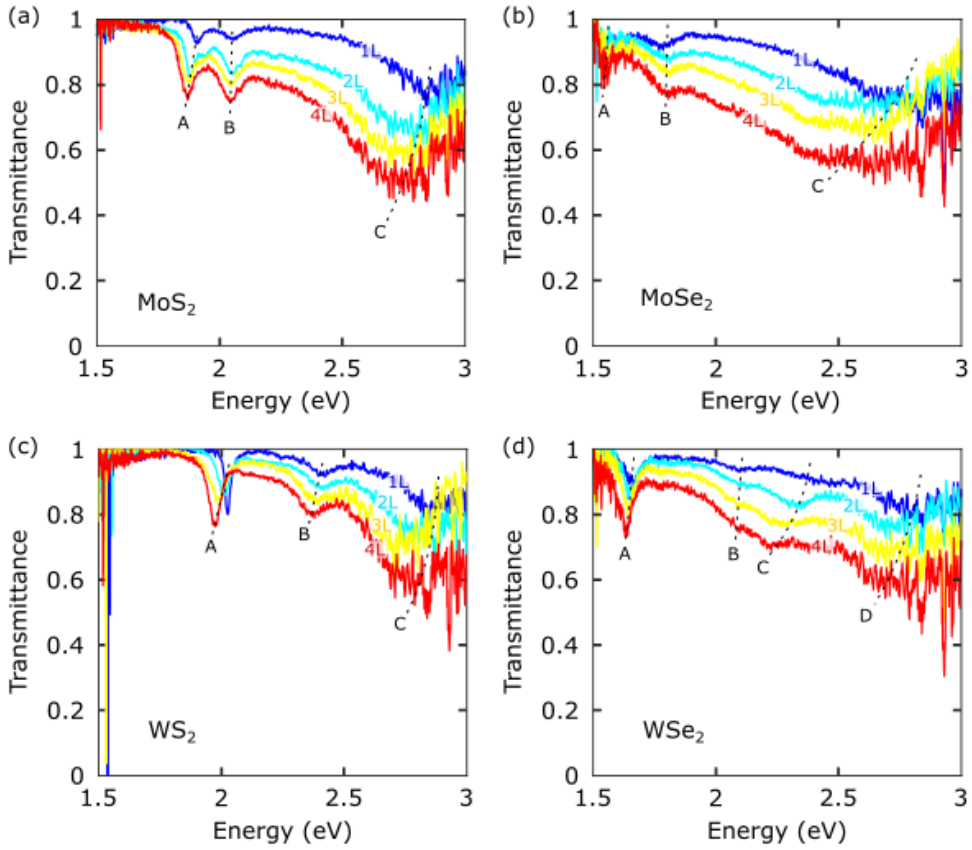

Figure 9. Transmittance spectra from 1L (dark blue) to 4L (red) measured in (a) MoS_2, (b) $MoSe_2$, (c) WS_2 and (d) WSe_2 samples on PDMS substrate.

The excitonic resonances also appear in the differential reflectance spectra, as shown in Figure 10. So, we can easily obtain the number of layers in a TMDC with a fast measurement. Likewise, these two techniques allow us to obtain optical information, independently on the carrying substrate.

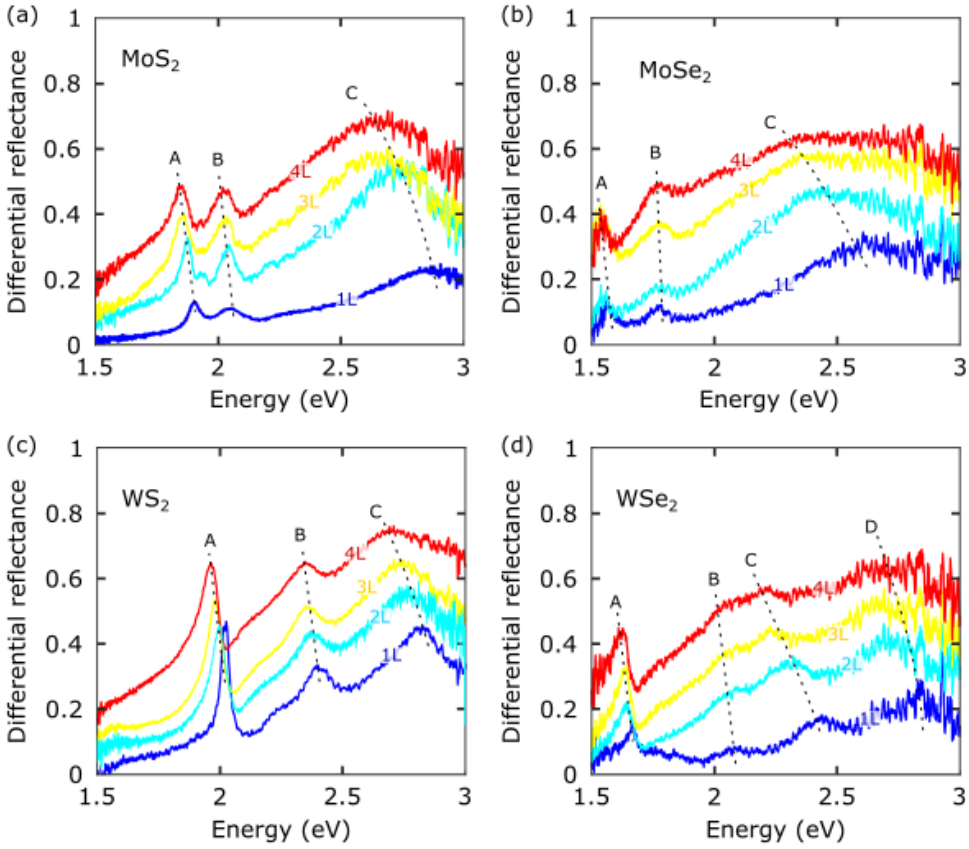

Figure 10. Differential reflectance spectra from 1L (dark blue) to 4L (red) measured in (a) MoS_2, (b) $MoSe_2$, (c) WS_2 and (d) WSe_2 samples on PDMS substrate.

2.5 Optical transmission acquired from optical images

2.5.1 Introduction

This section describes a new optical technique developed for determining the number of layers of a 2D material by quantitatively studying their optical transmittance extracted from optical images. Moreover, this characterization can be done by analysing optical microscope images with programs like Gwyddion or ImageJ.[35,36] The transmittance is monotonically dependent on the number of layers in most semiconducting 2D materials, which gives us the opportunity of extracting this information from an optical image of the sample. Once the number of layers is calibrated with the transmittance, we can use this analysis to select the flakes before transferring them to an opaque substrate. There are other methods for extracting the

number of layers by using the optical contrast, but they usually require transferring the flakes to the final substrate. Our technique allows the identification of the desire flake when it is still in the PDMS used during mechanical exfoliation. Thus, we have complete control over the sample choice without needing to choose after the transfer process (in the next section, we will study the importance of this possibility).

2.5.2 Optical transmission

In order to obtain the optical transmission of a flake, we need an optical microscopy image of this flake acquired in transmission mode. Figure 11(a) shows an image of a MoS_2 flake, which is mechanically exfoliated on a PDMS stamp. The PDMS is a substrate with the advantage of being a transparent, which allows us to obtain transmission mode images.

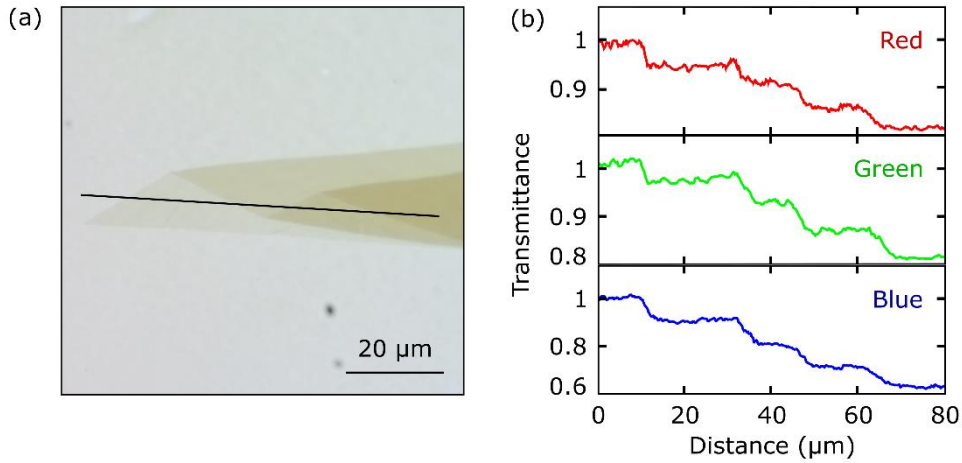

Figure 11. (a) Optical image acquired in transmission mode of a MoS_2 flake with areas of different thicknesses. (b) Profiles of the transmittance in the red, green and blue channels along the line plotted in (a).

The digital images are composed by three different channels, red, green and blue (RGB), which provide the different colours to the image. Figure 11(b) shows the transmittance values in each channel obtained along the profile displayed in Figure 11(a). In order to calculate the transmittance in each area of the sample, the formula used is:

$$T = \frac{S_{sample}}{S_{substrate}}$$

where T is the transmittance, S_{sample} is the value of the channel (RGB) intensity in that area and $S_{substrate}$ is the value of the channel (RGB) intensity in the substrate (in our case, it is the PDMS). The steps in the transmittance of all the channels, which correspond with the different thicknesses of the sample, can be easily distinguished. So, the transmission in the image correlates with the number of layers of the sample.

In order to use this method for thickness determination in 2D materials, it is necessary to know its accuracy. For this reason, we studied the optical images of 202 MoS_2 flakes with this technique. The information obtained provided us data to calculate the transmittance from images, obtaining enough statistics about the variations in the transmittance values and the uncertainty in the measurements. Figure 12 shows the histograms of 1-transmittance in each channel (RGB) calculated in all the flakes. It can be easily observed that the transmittance presents well-defined peaks, which correspond to different thicknesses of the material. These peaks are better distinguished in the blue channel due to the bigger separation between them. Moreover, the width of the peaks in the blue channel is the same as for the peaks in the rest of the channels, providing a higher contrast between 1, 2, 3 and 4 layers of MoS_2. The reason of this higher contrast is the presence of the exciton C in the blue part of the spectrum in MoS_2, as well as $MoSe_2$, WS_2 and WSe_2.[37,38] So, we focus on the blue channel transmittance for determining the thickness, which is easier thanks to the strong absorption changes in that wavelength range.

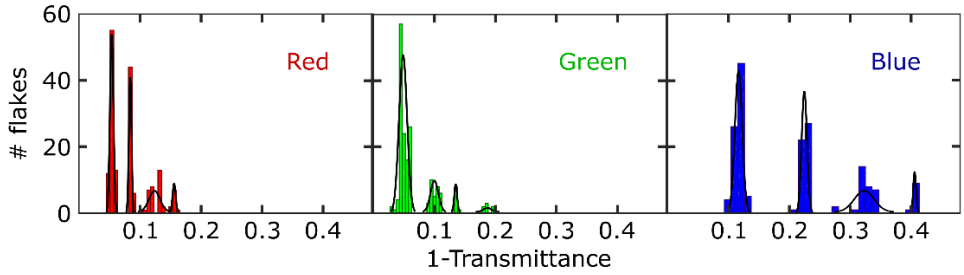

Figure 12. Histograms of 1-transmittance calculated in 202 MoS_2 flakes for the red, green and blue channels.

2.5.3 Comparison with the previous optical methods

Along this chapter, we studied other optical techniques which allow us to obtain the number of layers in MoS_2 and other TMDCs. So, the optical transmittance method is evaluated by contrasting the data obtained with this technique and the information extracted from other spectroscopic techniques. From all the MoS_2 flakes used in the previous section, four of them with different thicknesses (from 1L to 4L) were chosen to perform Raman, photoluminescence and differential reflectance measurements, providing three independent methods to verify the information. The flakes are labelled as 1L, 2L, 3L and 4L depending on the thickness calculated from the optical images.

Figure 13(a) shows the Raman signal (vertically displaced 0.1 for facilitating the inspection) for the flakes measured with a 532 nm excitation laser. The Raman spectra of the flakes show the A_{1g} and E^1_{2g} phonons corresponding to MoS_2. As it was mentioned in previous section, the energies of the phonons in MoS_2[29,39] change with the number of layers, allowing us to check the thickness determined by the blue channel optical transmittance.[32]

The photoluminescence was also measured in the same flakes using a 532 nm excitation laser. In this case, we can assigned the number of layers in MoS_2 flakes thanks to the strong dependency on the intensity and position of exciton A with the thickness.[40,41] The thickness of the flakes determined by the blue channel optical transmittance is again confirmed by another measurement.

Finally, the number of layers in the samples was tested by micro-reflectance spectroscopy. Figure 13(c) shows the spectra recorded in the four MoS_2 flakes, ranging from 1L to 4L. Here, the exciton A energy position is the parameter which allow us to determine the number of layers in the flakes.[38] This technique confirms the assignment of layers performed by the blue channel transmission method.

The different optical methods validate the correct determination of the number of layers in the MoS_2 flakes, allowing us to assign the thickness for the 202 MoS_2 flakes shown in the previous section. In Figure 13(d), the blue channel histogram is displayed again within the scatter plot of all the data. As we observe, the flakes are classified by the number of layers in the scatter plot, showing a clear dependency on the transmittance value.

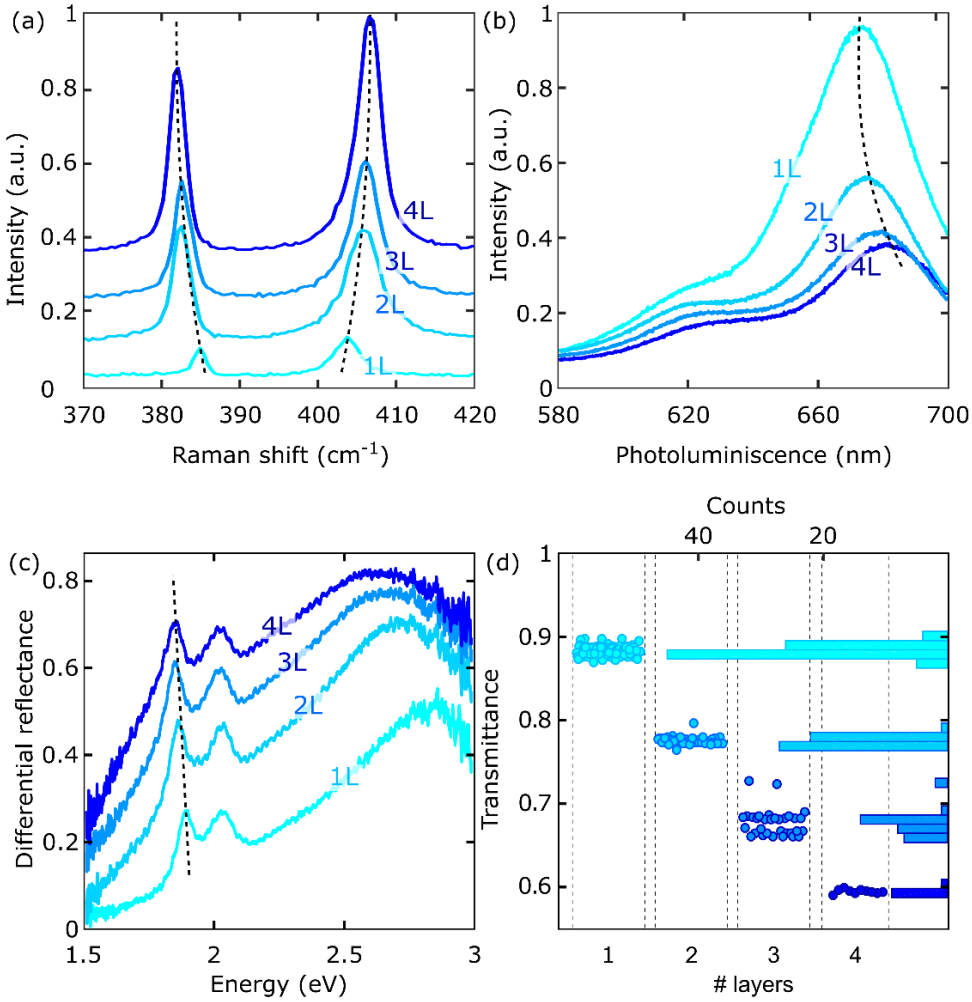

Figure 13. (a) Raman spectra of MoS_2 with 1L, 2L, 3L and 4L measured with a 532 nm excitation laser and vertically displaced 0.1. (b) Photoluminescence of MoS_2 with 1L, 2L, 3L and 4L measured with a 532 nm excitation. (c) Differential reflectance spectra of MoS_2 with 1L, 2L, 3L and 4L. (d) Scatter plot of the transmittance of the 202 MoS_2 flake in the blue channel together with the histogram shown in Figure 13.

2.5.4 Robustness of the technique

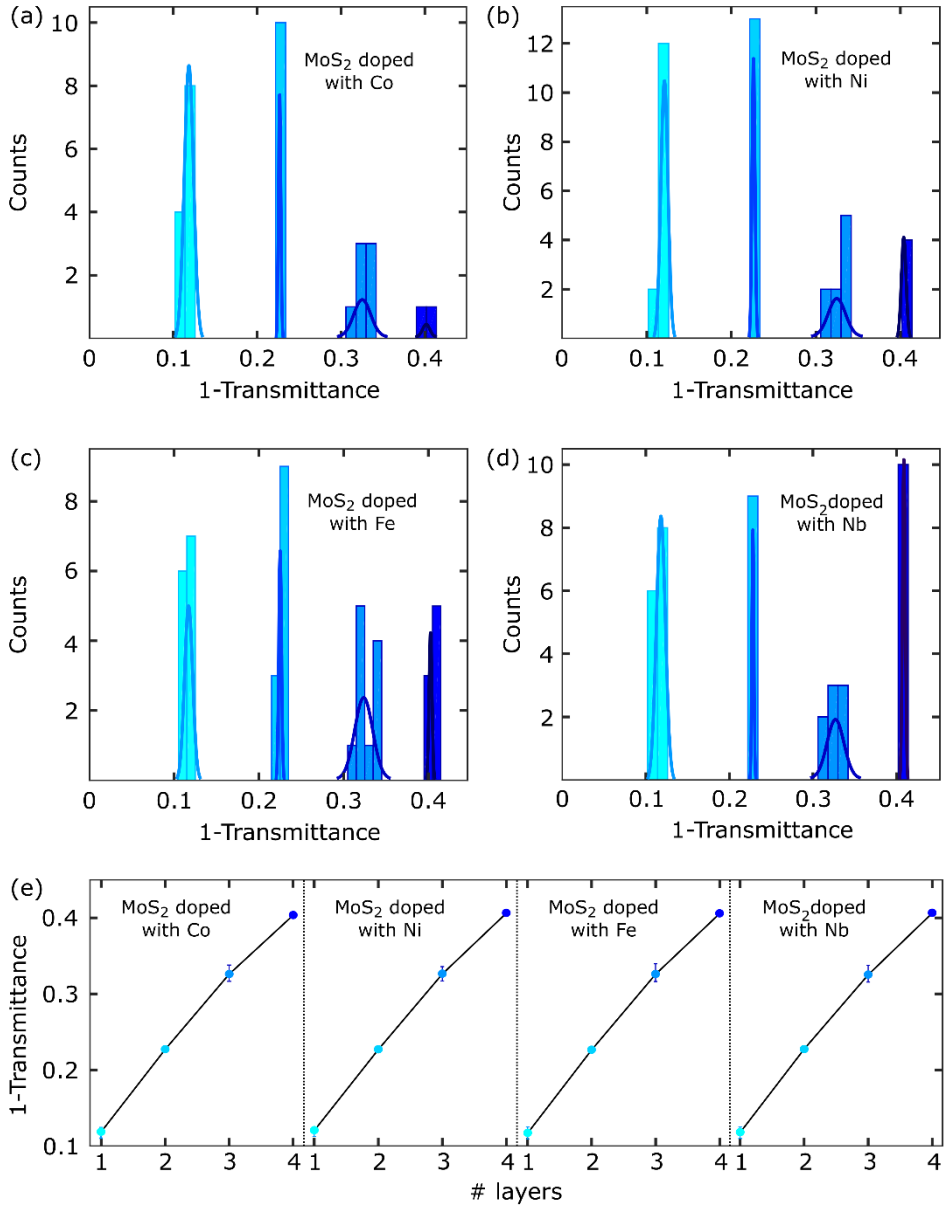

Figure 14. (a)-(d) Histograms of 1-transmittance calculated in 50 MoS_2 flakes doped with (a) Co, (b) Ni, (c) Fe and (d) Nb. (e) Values of 1-transmittance for different number of layers of MoS_2 with different doping extracted from the gaussian fits of the histograms.

The samples used in the previous test come from the same bulk material, a molybdenite mineral from Moly Hill mine, Quebec. In order to ensure that the previous results do not change from sample to sample, we measure MoS_2 with different doping levels. The MoS_2 new bulk materials were synthesized with substitutional metal atoms in the Mo sites. Thus, we can check if chemical changes (that usually have a big impact in the electronic characteristics[42,43]) affect or not our thickness determination method. The synthesis was performed following the technique described in References [42,44]. The chosen dopant metals for the MoS_2 are Fe, Ni, Nb and Co. In order to achieve a doping level of 0.3% to 0.4%, it is necessary to introduce a 0.5% of the metal inside the ampoule used for the synthesis.

Once the new bulk MoS_2 are ready, we exfoliated 50 flakes of each doped sample with PDMS for extracting the optical transmittance in the blue channel. In Figure 14, we can observe the histograms obtained for each doped material, which show similar peaks to the ones in the blue channel of Figure 12. The values extracted with the method do not depend on the exact chemical composition of the MoS_2, being the determination of the number of layers independent on the doping level of the sample. Furthermore, this insensitivity to the chemical composition of the sample is a great advantage compare with the previous spectroscopic methods like Raman and photoluminescence. These two last techniques are very susceptible to any changes in the doping of the sample or other chemical variations.[45–49]

2.5.5 Study in other materials

The method of determining the number of layers of MoS_2 by measuring the optical transmittance can be easily extended to other 2D materials, starting with the most common TMDCs. In Figure 15, we show the histograms extracted from the analysis of 202 MoS_2 flakes, 200 $MoSe_2$ flakes, 200 WS_2 flakes and 200 WSe_2 flakes. As it was previously mentioned, these TMDCs present a big change in the transmittance of the blue channel due to the presence of the exciton C. We can observe that the blue channel transmission in all the materials presents several peaks which correspond to different thicknesses. As in the MoS_2 case, the method allows us to assign the number of layers of the sample by extracting the blue channel transmittance from the optical images.

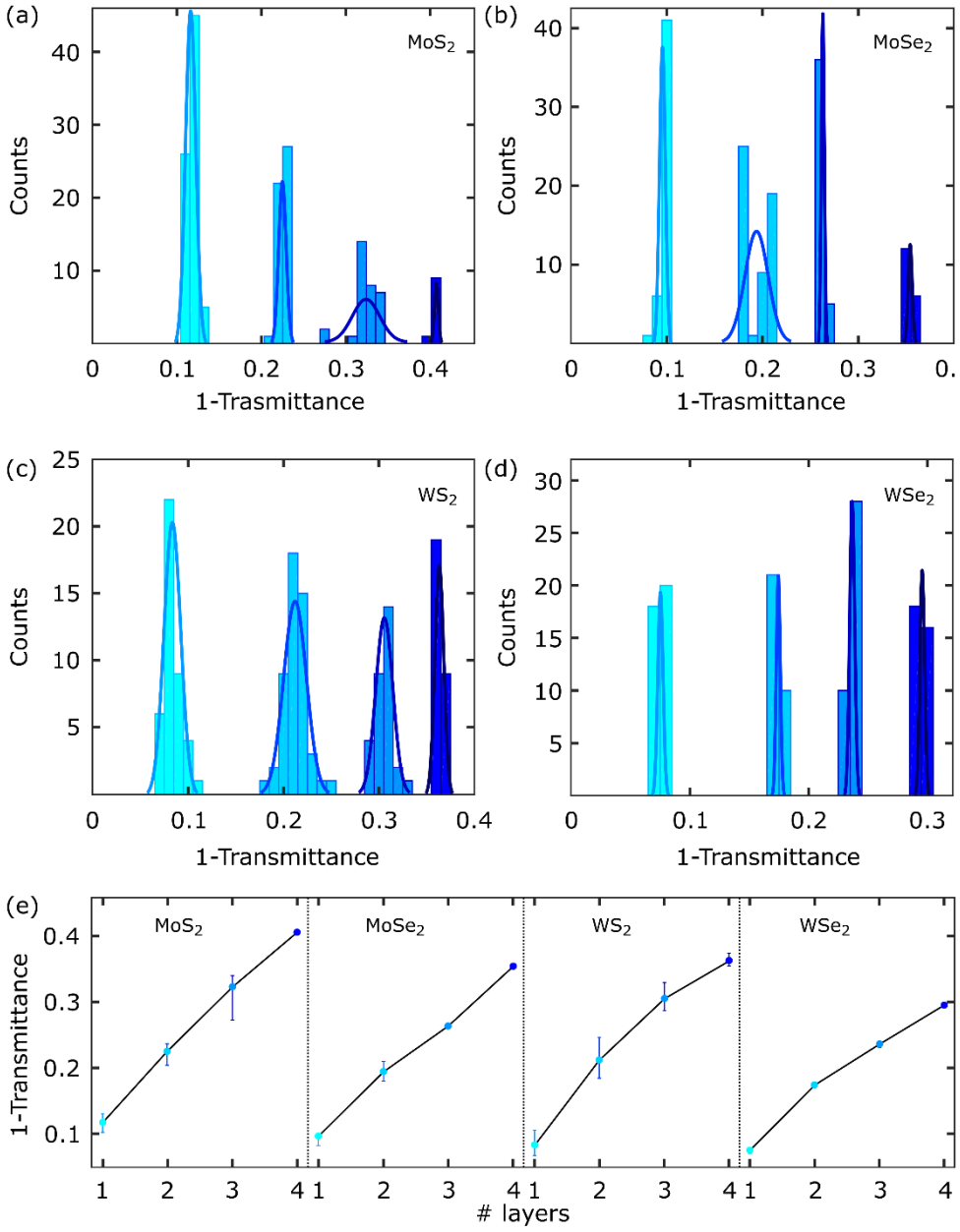

Figure 15. (a)-(d) Histograms of 1-transmittance calculated in (a) 202 MoS_2 flakes, (b) 200 $MoSe_2$ flakes, (c) 200 WS_2 flakes and (d) 200 WSe_2 flakes. (e) Values of 1-transmittance for different number of layers of MoS_2, $MoSe_2$, WS_2 and WSe_2 extracted from the gaussian fits of the histograms.

On the other hand, the channel selected for observing the transmittance depends on the absorbance spectrum of the material. The TMDC family studied here exhibits in the blue part of the spectrum the exciton C, facilitating the peaks resolution in the blue channel. Thus, each material needs to use the channel in which the change in the absorbance depends more on the number of layers.

2.6 Conclusions

In this chapter, we presented the main optical techniques used along this thesis for studying 2D materials. First, the Raman and photoluminescence spectroscopies were explained, showing the setup and the possibilities of the technique. The information provided by Raman and photoluminescence measurements are useful for the structural and chemical composition studies, as well as allowing us to accurately obtain the thickness of the material. These measurements are very sensitive to strain or doping changes in the materials, but the Raman and photoluminescence requires of active modes, excitonic resonances or other energetic transitions in order to show valuable information.

For samples without these characteristics, the differential reflectance and transmittance can show the optical behaviour of a 2D material in a wide range of wavelengths. Both are related to the absorbance of the material, allowing us to extract the absorbance spectrum from these measurements. Likewise, it can be used as a tool for calculating the thickness of the material in cases like TMDCs. On the other hand, the absorbance of a 2D material suffer changes under strain application, so these methods provide information about the modification of the optical properties of the material under strain.

Finally, the last section explained the fastest and easiest method to obtain the thickness of 2D materials. The extraction of the samples optical transmittance by using optical images is a technique which is available in any laboratory since the only requirement is having a microscope with a camera. The transmittance can be calibrated with other complementary techniques (Raman, photoluminescence, differential reflectance, transmittance) in order to obtain the relation between the transmittance and the number of layers of certain material. We extracted this dependency in the case of TMDCs, which will be helpful for producing the straintronic devices.

References

1. Castellanos-Gomez, A. Why all the fuss about 2D semiconductors? *Nat. Photonics* **10**, 202–204 (2016).
2. Zhou, S. Y. *et al.* First direct observation of Dirac fermions in graphite. *Nat. Phys.* **2**, 595–599 (2006).
3. Mak, K. F., Lee, C., Hone, J., Shan, J. & Heinz, T. F. Atomically thin MoS_2: A new direct-gap semiconductor. *Phys. Rev. Lett.* **105**, (2010).
4. Schaibley, J. R. *et al.* Valleytronics in 2D materials. *Nature Reviews Materials* **1**, (2016).
5. Dai, S. *et al.* Tunable phonon polaritons in atomically thin van der Waals crystals of boron nitride. *Science (80-.).* **343**, 1125–1129 (2014).
6. Splendiani, A. *et al.* Emerging Photoluminescence in Monolayer MoS_2.
7. Hendry, E., Hale, P. J., Moger, J., Savchenko, A. K. & Mikhailov, S. A. Coherent nonlinear optical response of graphene. *Phys. Rev. Lett.* **105**, (2010).
8. Jadczak, J. *et al.* Probing of free and localized excitons and trions in atomically thin WSe_2, WS_2, $MoSe_2$ and MoS_2 in photoluminescence and reflectivity experiments. *Nanotechnology* **28**, (2017).
9. Wang, X. *et al.* Highly anisotropic and robust excitons in monolayer black phosphorus. *Nat. Nanotechnol.* **10**, 517–521 (2015).
10. Kneipp, K., Kneipp, H., Itzkan, I., Dasari, R. R. & Feld, M. S. Ultrasensitive Chemical Analysis by Raman Spectroscopy. *Chem. Rev.* **99**, 2957–2975 (1999).
11. Movasaghi, Z., Rehman, S. & Rehman, I. U. Raman spectroscopy of biological tissues. *Applied Spectroscopy Reviews* **42**, 493–541 (2007).
12. Mooradian, A. Photoluminescence of metals. *Phys. Rev. Lett.* **22**, 185–187 (1969).
13. Hercules, D. M. Photoluminescence of solutions with applications to photochemistry and analytical chemistry (Parker, C. A.). *J. Chem. Educ.* **46**, A449 (1969).
14. Ferrari, A. C. Raman spectroscopy of graphene and graphite: Disorder, electron-phonon coupling, doping and nonadiabatic effects. *Solid State Commun.* **143**, 47–57 (2007).
15. Niehues, I. *et al.* Strain Control of Exciton−Phonon Coupling in Atomically Thin Semiconductors. (2018).
16. Frisenda, R. *et al.* Micro-reflectance and transmittance spectroscopy: A versatile and powerful tool to characterize 2D materials. *J. Phys. D. Appl. Phys.* **50**, (2017).
17. Taghavi, N. S. *et al.* Thickness determination of MoS_2, $MoSe_2$, WS_2 and WSe_2 on transparent stamps used for deterministic transfer of 2D materials. *Nano Res.* **12**, 1691–1695 (2019).
18. Frisenda, R. *et al.* Recent progress in the assembly of nanodevices and van

der Waals heterostructures by deterministic placement of 2D materials. *Chem. Soc. Rev.* **47**, (2018).
19. Castellanos-Gomez, A. *et al.* Deterministic transfer of two-dimensional materials by all-dry viscoelastic stamping. *2D Mater.* **1**, 011002 (2014).
20. Modern Raman Spectroscopy: A Practical Approach - Ewen Smith, Geoffrey Dent.
21. Hannewald, K., Glutsch, S. & Bechstedt, F. Theory of photoluminescence in semiconductors. *Phys. Rev. B - Condens. Matter Mater. Phys.* **62**, 4519–4525 (2000).
22. Malard, L. M., Pimenta, M. A., Dresselhaus, G. & Dresselhaus, M. S. Raman spectroscopy in graphene. *Physics Reports* **473**, 51–87 (2009).
23. Ribeiro, H. B., Pimenta, M. A. & de Matos, C. J. S. Raman spectroscopy in black phosphorus. *Journal of Raman Spectroscopy* **49**, 76–90 (2018).
24. Guo, Z. *et al.* From Black Phosphorus to Phosphorene: Basic Solvent Exfoliation, Evolution of Raman Scattering, and Applications to Ultrafast Photonics. *Adv. Funct. Mater.* **25**, 6996–7002 (2015).
25. Liu, S. *et al.* Thickness-dependent Raman spectra, transport properties and infrared photoresponse of few-layer black phosphorus. *J. Mater. Chem. C* **3**, 10974–10980 (2015).
26. Castellanos-Gomez, A. *et al.* Isolation and characterization of few-layer black phosphorus. *2D Mater.* **1**, (2014).
27. Li, H. *et al.* From bulk to monolayer MoS 2: Evolution of Raman scattering. *Adv. Funct. Mater.* **22**, 1385–1390 (2012).
28. Sahin, H. *et al.* Anomalous Raman spectra and thickness-dependent electronic properties of WSe_2. *Phys. Rev. B - Condens. Matter Mater. Phys.* **87**, (2013).
29. Tonndorf, P. *et al.* Photoluminescence emission and Raman response of MoS_2, $MoSe_2$, and WSe_2 nanolayers. in *2013 Conference on Lasers and Electro-Optics, CLEO 2013* (IEEE Computer Society, 2013).
30. Echeverry, J. P., Urbaszek, B., Amand, T., Marie, X. & Gerber, I. C. Splitting between bright and dark excitons in transition metal dichalcogenide monolayers. *Phys. Rev. B* **93**, (2016).
31. Robert, C. *et al.* Exciton radiative lifetime in transition metal dichalcogenide monolayers. *Phys. Rev. B* **93**, (2016).
32. Li, H. *et al.* From Bulk to Monolayer MoS_2: Evolution of Raman Scattering. *Adv. Funct. Mater.* **22**, 1385–1390 (2012).
33. McIntyre, J. D. E. & Aspnes, D. E. Differential reflection spectroscopy of very thin surface films. *Surf. Sci.* **24**, 417–434 (1971).
34. Dhakal, K. P. *et al.* Confocal absorption spectral imaging of MoS_2: Optical transitions depending on the atomic thickness of intrinsic and chemically doped MoS_2. *Nanoscale* **6**, 13028–13035 (2014).
35. Gwyddion: an open-source software for SPM data analysis in: Open Physics Volume 10 Issue 1 (2012).
36. Schneider, C. A., Rasband, W. S. & Eliceiri, K. W. NIH Image to ImageJ: 25

years of image analysis. *Nature Methods* **9**, 671–675 (2012).
37. Castellanos-Gomez, A., Quereda, J., van der Meulen, H. P., Agraït, N. & Rubio-Bollinger, G. Spatially resolved optical absorption spectroscopy of single- and few-layer MoS_2 by hyperspectral imaging. *Nanotechnology* **27**, 115705 (2016).
38. Niu, Y. et al. Thickness-Dependent Differential Reflectance Spectra of Monolayer and Few-Layer MoS_2, $MoSe_2$, WS_2 and WSe_2. *Nanomaterials* **8**, 725 (2018).
39. Lee, C. *et al.* Anomalous lattice vibrations of single- and few-layer MoS_2. *ACS Nano* **4**, 2695–2700 (2010).
40. Splendiani, A. *et al.* Emerging Photoluminescence in Monolayer MoS_2. *Nano Lett.* **10**, 1271–1275 (2010).
41. Mak, K. F., Lee, C., Hone, J., Shan, J. & Heinz, T. F. Atomically thin MoS_2: A new direct-gap semiconductor. *Phys. Rev. Lett.* **105**, 2–5 (2010).
42. Suh, J. *et al.* Doping against the native propensity of MoS_2: Degenerate hole doping by cation substitution. *Nano Lett.* **14**, 6976–6982 (2014).
43. Svatek, S. A. *et al.* Gate tunable photovoltaic effect in MoS_2 vertical p-n homostructures. *J. Mater. Chem. C* **5**, 854–861 (2017).
44. Wang, S. Y., Ko, T. S., Huang, C. C., Lin, D. Y. & Huang, Y. S. Optical and electrical properties of MoS_2 and Fe-doped MoS_2. in *Japanese Journal of Applied Physics* **53**, (Japan Society of Applied Physics, 2014).
45. Chen, Y. *et al.* Composition-dependent Raman modes of $Mo_{1-x}W_xS_2$ monolayer alloys. *Nanoscale* **6**, 2833–2839 (2014).
46. Dumcenco, D. O., Kobayashi, H., Liu, Z., Huang, Y. S. & Suenaga, K. Visualization and quantification of transition metal atomic mixing in $Mo_{1-x}W_xS_2$ single layers. *Nat. Commun.* **4**, (2013).
47. Mann, J. *et al.* 2-dimensional transition metal dichalcogenides with tunable direct band gaps: $MoS_{2(1-x)}Se_{2x}$ monolayers. *Adv. Mater.* **26**, 1399–404 (2014).
48. Zhang, M. *et al.* Two-dimensional molybdenum tungsten diselenide alloys: photoluminescence, Raman scattering, and electrical transport. *ACS Nano* **8**, 7130–7 (2014).
49. Mouri, S., Miyauchi, Y. & Matsuda, K. Tunable photoluminescence of monolayer MoS_2 via chemical doping. *Nano Lett.* **13**, 5944–5948 (2013).

3. Electrical contacts on 2D flakes

3.1 Introduction

In the previous chapter, we focussed in the main techniques used for optical characterization of 2D materials. Although these methods are very important for the experiments of this thesis, it is even more crucial to establish electrical contacts with the flakes in order to perform optoelectronic characterization of 2D materials. There are different processes that are necessary for contacting the flakes.

First, we comment about the different techniques available for the patterning of metallic electrodes, which allow us to electrically contact the flakes. Finally, the main methods to connect the patterned metallic micro-electrodes with a source-meter unit for measuring the devices are discussed. The last technique explained is a method developed along this thesis in order to avoid the electrodes patterning by directly probing the flakes. The experiments explained in the next chapter require of all these steps prior the measurements.

3.2 Electrodes patterning

There are different techniques that allow us to pattern electrodes for providing electrical contact to 2D materials. Despite most of these techniques were not used during this thesis (the only techniques used are the shadow mask patterning and the maskless photolithography with the SmartPrint system), we provide an overview in this Chapter of all the methods for offering a better understanding of the different possibilities of each technique.

3.2.1 Lithography techniques

3.2.1.1 Electron beam lithography

One of the most commonly used methods for fabricating electrodes on a flake of a 2D material is the electron beam lithography (e-beam lithography).[1–4] This technique allows us to pattern electrodes on a chosen flake which is already transferred in a substrate. Figure 1 shows the main steps of e-beam lithography:[3,4]

- Step 1: Prior to the process, it is necessary to clean the substrate due to the sensitivity of this technique to external contaminations. The cleaning also facilitates the homogeneity of the resist coating that will be produce in the next step. Usually plasma cleaning is used to remove most of the dirt on the surface of the substrate. In the absence of equipment for plasma cleaning, the substrate can be cleaned with acetone, isopropanol and distilled water (in this order) while applying ultrasonication.
- Step 2: The resist used for coating the substrate surface is a solution of an organic polymer. So, the liquid solution of resist is dropped on the substrate, which is placed in a spin-coater. The substrate with the liquid spins in order to create a homogeneous thin film coating of resist on the surface. During this process, the solvent of the resist solution evaporates creating a solid film on the substrate. The coated substrate is baked to ensure the complete evaporation of the resist.
- Step 3: There are two types of resists which behave differently during the exposure step: positive and negative. The positive resist is insoluble in a solvent called developer, but it becomes soluble under light exposure. On the other hand, the negative resist is soluble in developer, turning insoluble under light exposure. So, an e-beam draws in the resist the chosen pattern in order to remove it from the parts that will be metallized later.
- Step 4: The exposed substrate is introduced in the developer solution, which dissolves the soluble resist areas. In this way, the substrate has resist with open areas forming the desire pattern.
- Step 5: Once the surface has a resist pattern with opened areas, the substrate is introduced in a metal evaporator. Here, the metal is evaporated inside a chamber in order to adhere the metal atoms to the exposed substrate surface. The most common metal used are Ti, Cr, Au and Pt; requiring some of them a previous metal evaporation of another metal in order to stick to the substrate.
- Step 6: Finally, the remaining resist with a layer of metal on top is removed by a lift off process. The substrate is introduced in a bath of acetone, usually at warm temperature (~50 ºC), during ~30 min to eliminate the resist and residues. Then, the resulting substrate has a metallic pattern on the surface.

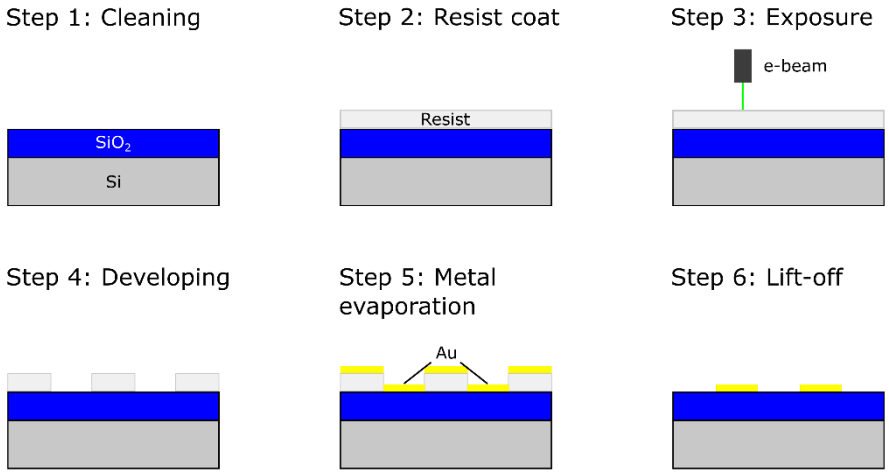

Figure 1. Scheme of the different steps of the electron beam lithography. The example shows a SiO_2/Si substrate in which Au is evaporated.

In the case of 2D materials, this process is usually performed at least two times: patterning of markers and pads and patterning of electrodes. It is usually needed to pattern a matrix of markers before the electrodes patterning to provide an alignment system for fabricating the electrodes onto the flake. So, the whole process is the previous patterning of markers and pads with lithography, for proceeding later to the random transfer of 2D flakes from an adhesive tape to the substrate with pre-patterned markers and the last step would be the patterning of electrodes connecting the flake with the pads. This process becomes even more complicated for vertical heterostructures in which it would be necessary more lithographic steps.

The main advantage of this technique is the possibility of contacting with metallic electrodes the flakes that are already transferred in a substrate. However, the method is time consuming, requiring several steps in which the sample can be damaged, or part of the process can go bad.

3.2.1.2 Conventional photolithography

Another technique used for patterning electrodes is the photolithography.[1,4] Unlike e-beam lithography, the electrodes fabricated by this technique are patterned prior the flake transfer. So, there is no need of pre-patterning markers or pads for aligning the electrodes. Figure 2 shows the different steps followed, which are the same than the e-beam lithography. We can find the main difference between both methods in

the exposure step. As shown in Figure 2, a Cr/glass mask is used to cover the resist while illuminating the sample with UV light. Thus, the mask has a pattern created in the Cr layer which is put in contact with the resist to expose the chosen areas. This process requires different masks for each pattern, so different masks have to be fabricated in order to create more type of devices.

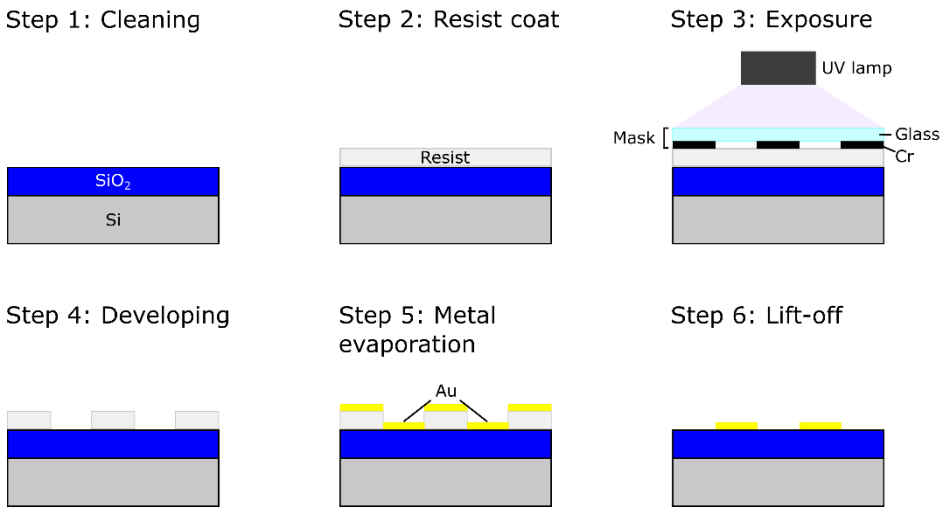

Figure 2. Scheme of the different steps of the photolithography. The example shows a SiO_2/Si substrate in which Au is evaporated.

3.2.1.3 Maskless-photolithography: Smart print

The Smart Print is a photolithography system designed by Smartforce Technologies for working on substrate patterning without the need of a physical mask. It follows the same procedure previously shown in Figure 2, but the exposure step is done with a light pattern instead of using a physical mask for creating the light pattern. This pattern is produced by the digital draw on an imaging software of the pattern, which is sent to the Smart Print's beam head. The light beam passes through an LCD matrix in which the digital pattern is present, allowing to cross the light only in the chosen areas. Then, the light is focused in the resist to expose the different parts of the substrate producing the designed pattern. This technique achieves a resolution of 0.7 µm, which is two orders of magnitude bigger than the resolution of the previous methods.

3.2.2 Shadow mask

The metallic electrodes used during this thesis are manufactured by utilizing this technique. Most of the electrodes used were fabricated by another person of the group, only some of the electrodes were produced by me.

When the geometry of the desired metal electrodes is rather simple, a direct evaporation through a shadow mask (or micro-stencil) is a good alternative technique for patterning electrodes.[5,6]

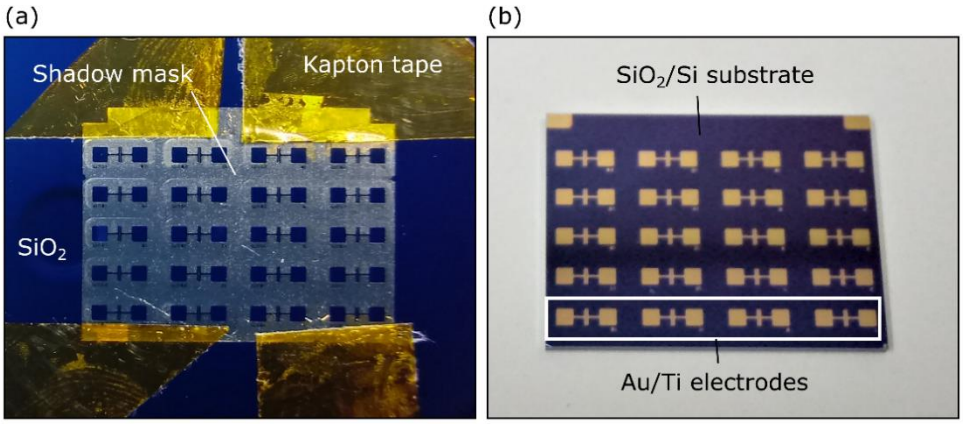

Figure 3. (a) Optical image of a commercial shadow mask (Ossila E321) stuck on a SiO_2/Si substrate with few pieces of Kapton tape. (b) Optical image of a SiO_2/Si substrate with Au/Ti pre-patterned electrodes. In this case, this sample is commercially available in Ossila (S221).

The shadow masks used for this technique can be fabricated with certain designed pattern or bought with pre-design patterns in different companies (the shadow mask shown in Figure 3a was bought in Ossila). The process starts similarly to the lithography, the substrate is first cleaned with the same cleaning method explained in the previous section. Once the substrate is clean, the shadow mask is attached to the substrate with Kapton tape, trying to reduce the space between the substrate and the mask like shown in Figure 3(a). Then, the substrate is introduced in the metal evaporator, in which the evaporated metal will adhere to the exposed substrate areas. The last step is the detachment of the shadow mask from the patterned substrate as shown in Figure 3(b). This process has only few easy steps, so the possibilities of failure are lower than in the case of the e-beam lithography. The main issue is the difficulty in the alignment of the shadow mask with certain flake. So, this technique

can be used for the creation of pre-patterned electrodes, but not for the evaporation of metal electrodes on transferred flakes.

3.2.3 Comparison

There are several differences between all the methods previously described, so the chosen technique for patterning the electrodes depends on the needed characteristics. The e-beam lithography is a technique which allows us to design any type of pattern in the resist with a resolution under the 500 nm. Moreover, it is the easiest method for electrodes patterning on top of a transferred flake. Nevertheless, the numerous steps of this technique make it time-consuming and there are high possibilities of spoiling the sample.

On the other hand, the photolithography is a shorter process which produce patterns with a resolution of ~1 μm. This method is usually used for fabricating arrays of electrodes with the same features. So, the major drawback of this method is the need of masks for creating the patterns, bounding the possible number designs.

The Smart Print joins the design flexibility of the e-beam lithography with the short process of the photolithography. The digital masks allow the fabrication of very different patterns, creating samples in just few steps. However, this technique has a low resolution of 2 μm and it cannot be used for patterning transferred flakes.

Finally, the metal evaporation through shadow masks is the fastest process to obtain electrodes. Nonetheless, shadow masks provide limited options for patterning electrodes and it is still not possible to pattern electrodes on transferred flakes. Likewise, the metal patterning can be bad due to the presence of spaces between the mask and the substrate or the damaging of the mask (very fragile).

3.3 Electrical contact with the pad electrodes

Once the flakes are contacted by electrodes, we can used different methods to connect them in order to perform electrical measurements. Here, we provide an overview of the most common techniques, that are the wire bonding and the use of probe stations. However, the only technique used along this thesis was the electrical contact of the pad electrodes by different probe stations. As explain during the Section, there are different probe stations designs depending on the needs of the experiment. Each sub-section will explained the different choices that we have

available in the laboratory, the characteristics and the person responsible of the development of each setup.

3.3.1 Wire bonding

The wire bonding is a technique in which the metallic electrodes are connected with a piece of metal by a small wire.[7] The piece of metal is usually a copper board, which can be easily contacted by soldering cables to the surface. The small wires used for making the bonds are attached to both copper surface and the electrode allowing us to measure the optoelectronic properties of the samples. The bonds between the wire and the metal parts are fabricated with a combination of force, temperature and ultrasonic power. There are different types of bonding depending on the parameters used: thermocompression bonding, ultrasonic bonding and thermosonic bonding.

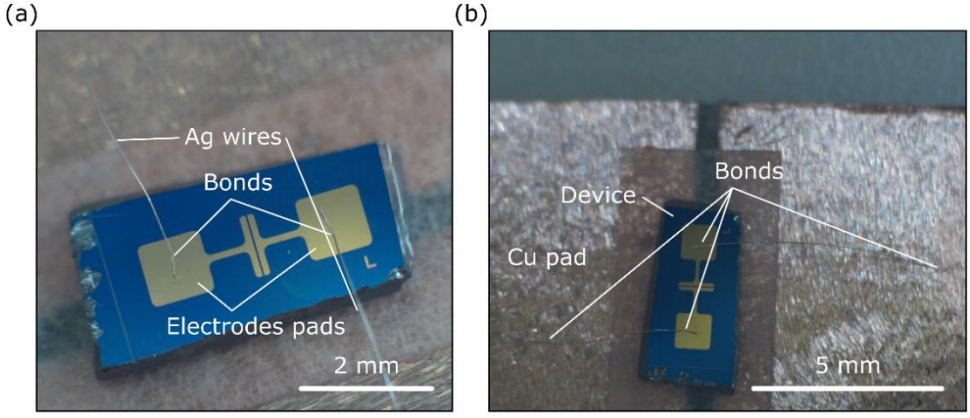

Figure 4. (a) Optical image of a device contacted by wire bonding. The bonds in the Au pads are indicated in the image. (b) Optical image of the same sample contacted by wire bonding obtained at lower magnification in order to appreciate the bonds in the Cu board.

The thermocompression bonding technique creates the bond with a combination of high bonding force from the metallic tip (which also handles the metallic wire) and temperatures above 300 ºC. The fabrication of bonds requires of a long formation time, which can produce a damage in the surface of the metal pads. On the other hand, we have the ultrasonic bonding method, in which the bonds are made at room temperature by applying ultrasonic power with the tip. The bonding force and the time for bonds fabrication are low, diminishing the possible damage of the pads. Finally, the thermosonic bonding technique requires of temperatures from 120 ºC to 220 ºC while using ultrasonic power. The bonds formation time is short, and the force is low, being the damage opportunities similar to the previous case.

Figure 5 shows a scheme of the main process followed by all the wire bonding techniques. First, the wire (usually an Au or Al wire) is placed in the bonder tip by threading the wire in the tip. Then, the tip is aligned with the Au pad of the electrode and lower down. At this point, each technique uses a different method to create the bond, as we already explained. Once the first bond is made, the tip with the wire is retracted to allow its placement on the copper board surface. Here, the second metal bond is fabricated by the chosen technique. Finally, the tip cut the metal wire to finish the process. The result is a contacted sample in which different electrical measurements can be performed.

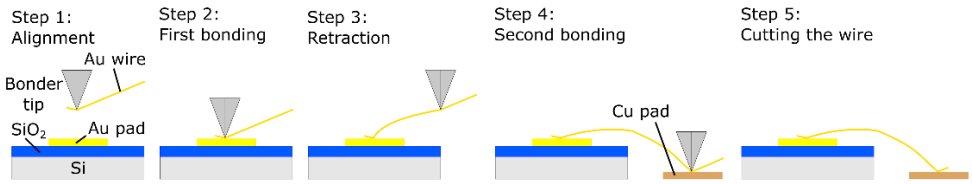

Figure 5. Scheme of the main steps of the wire bonding for all the cases.

3.3.2 Probe station

Electrical measurements in 2D materials are commonly carry out in probe stations, in which the sample electrodes are contacted by different kind of probes. These probes are connected to source-meters or multi-meters in order to perform optoelectronic characterizations of the devices. The number of probes in the probe station varies depending on the measurements performed in the equipment, being the most common configuration in this thesis two or three probes.

Here, we provide an overview of different commercial and home-made setups used along this thesis for performing the measurements, explaining the main components. We also show some of the possible characterizations that can be performed in one of our probe stations of a single-layer MoS_2 device on SiO_2/Si substrate. Some of these measurements will be useful for the experiment explained in the next chapter.

3.3.2.1 Commercial and home-made probe stations

Along this thesis, different probe stations have been operated depending on the requirements and the availability. First, we present the main commercial setup used for measuring, a Linkam probe station mounted by Riccardo Frisenda, which is

shown in Figure 6(a). As we can observe, there is a platform where the sample is deposited to contact it with the probes pointed in Figure 6(a). Moreover, these probes have magnets in the bottom part to attach them to the setup while making possible to place them in the desire position. The mentioned platform has a thermocouple connected in the base in order to control the temperature, as well as an internal heater. Furthermore, the chamber can be locked in order to pump the air inside while introducing liquid nitrogen in the system. The liquid nitrogen in combination with the heater allows us to set the temperature of the sample from 77 K to 650 K during the measurements.

This probe station allows us to perform simple measurements like bias voltage versus current characteristics or current dependency on the gate voltage, besides more complicated characterizations in combination with other components. Figure 6(b) shows an example of the implementation of a Linkam probe station in a scanning photocurrent setup. Apart of the probe station, the system includes an optical microscope with modified trinocular and binoculars, a motorized XY stage, the source-meter and two different lasers. Thus, the whole system is designed to map the current generated in certain area of the sample when a small spot of light is illuminating it. On the other hand, some adjustments in the design would allow to use the setup as a scanning micro-reflectance setup, providing another different application to this system. So, this commercial probe station is a versatile way to implement electrical measurements on 2D materials.

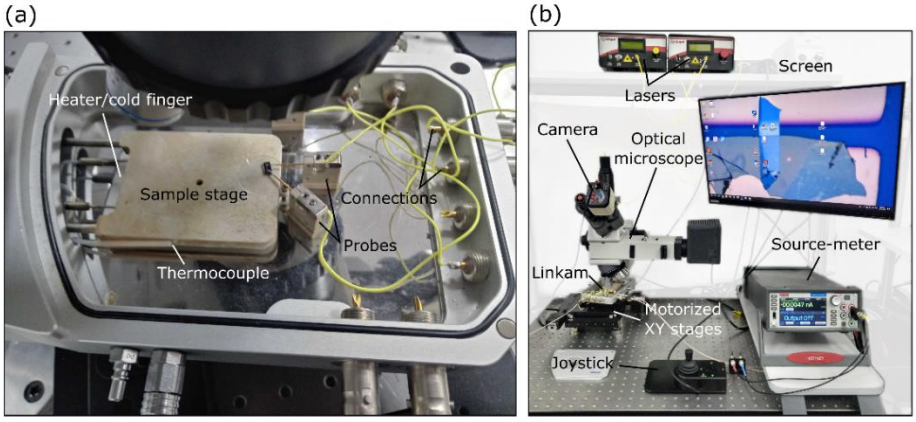

Figure 6. (a) Optical image of the Linkam probe station with the main components indicated. (b) Optical image of the scanning photocurrent setup in which the Linkam is embedded.

Commercial probe stations are a convenient tool for performing electronic characterization, but this is not an affordable option for all the laboratories. In this

case, a home-made probe station is a solution to minimize the price of the setup and include the needed characteristics. The first example of a home-made probe station used during this thesis is shown in Figure 7(a). Here, the probe station is designed by Andrés Castellanos Gómez and Riccardo Frisenda to measure the current dependency on the bias voltage, with the possibility of measuring under light conditions. When we introduce another manipulator with a probe and a cheap source, it is also possible to apply different gate voltages.

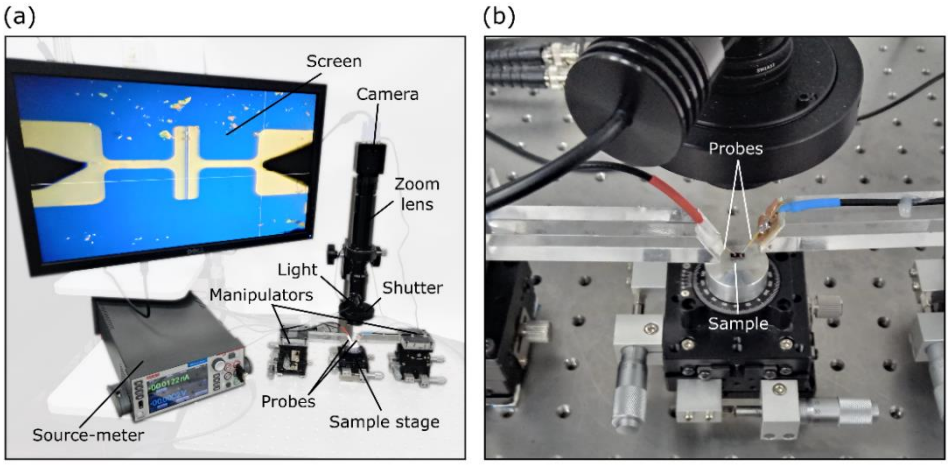

Figure 7. (a) Optical image of the home-made probe station with two probes. The different components are pointed in the image. (b) Zoomed image of the sample stage in which the two probes can be appreciated while they are contacting the sample.

In Figure 7(a), the crucial components of the probe station are pointed. There are two XYZ micro-stages where the probes are mounted. The probes are attached to home-made pieces to introduce angle to the tips in order to facilitate the observation of the tip landing on the sample electrodes. The sample is placed in a XY micro-stage with an added rotator as shown in Figure 7(b). Likewise, a zoom lens with a camera attached, which is connected to a screen, allows the observation of the process. Besides watching the probes landing, we can easily place a chosen light source in the zoom lens. In the case of connecting the light by an optical fiber with a known diameter, the light spot can be projected on the sample with the same size, making possible to calculate the power density of the light. This method requires to adjust the optical path of the light for projecting a focused spot on the sample, which is possible by changing the distance of the optical fiber to the beam splitter. Finally, a source-meter (Keithley 2450) is connected to the probes for characterizing the optoelectronic behaviour of the sample.

In this first setup is not possible to control the environment of the sample, like the temperature or the atmosphere. So, we display in Figure 8 and 9 other examples of probe stations setup by Félix Carrascoso Plana and Qinghua Zhao (not used during this thesis) in which we can measure in vacuum (~10^{-6}) or an inert gas atmosphere. The temperature can be also monitored, and a heater allows to increase the temperature from room temperature to 150 ºC. In both cases, we require to contact the sample with probes first, and test all the electrical connections before closing the chamber. This procedure is necessary because once the chamber is in vacuum, the probes cannot be operated from outside.

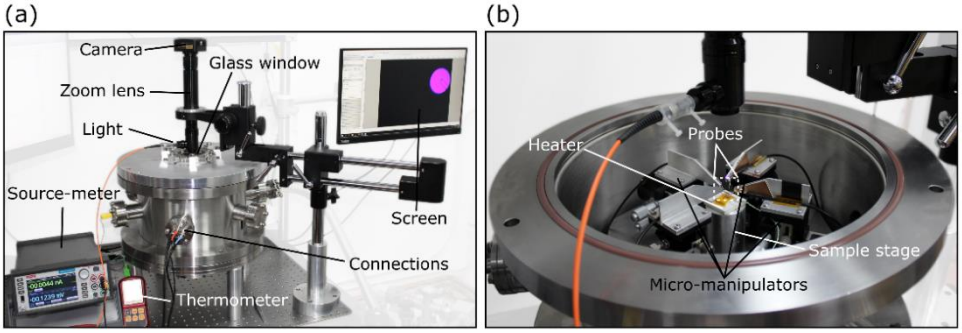

Figure 8. (a) Optical image of a home-made probe station to perform measurements in vacuum. The different components are pointed in the image. (b) Image of the probe station when the isolated chamber is opened. Here, the micromanipulators in which the probes are mounted, and the sample stage can be observed.

As we can observe, the probes and the cables are inserted inside home-made vacuum chambers. In order to allow the connection of the probes to a source-meter, the cables are attached to BNC feedthrough connectors placed in the chamber walls. So, these chambers have connections for contacting three electrodes (source, drain and gate), the heater and a thermocouple, which allows us to monitor the temperature on the sample. Another important characteristic of these setups in order to perform the optoelectronic measurements on the samples is the presence of a glass window covering the chamber. Thus, we can illuminate the sample by using the same method explained before thanks to the possibility of the projected light spot crossing the glass.

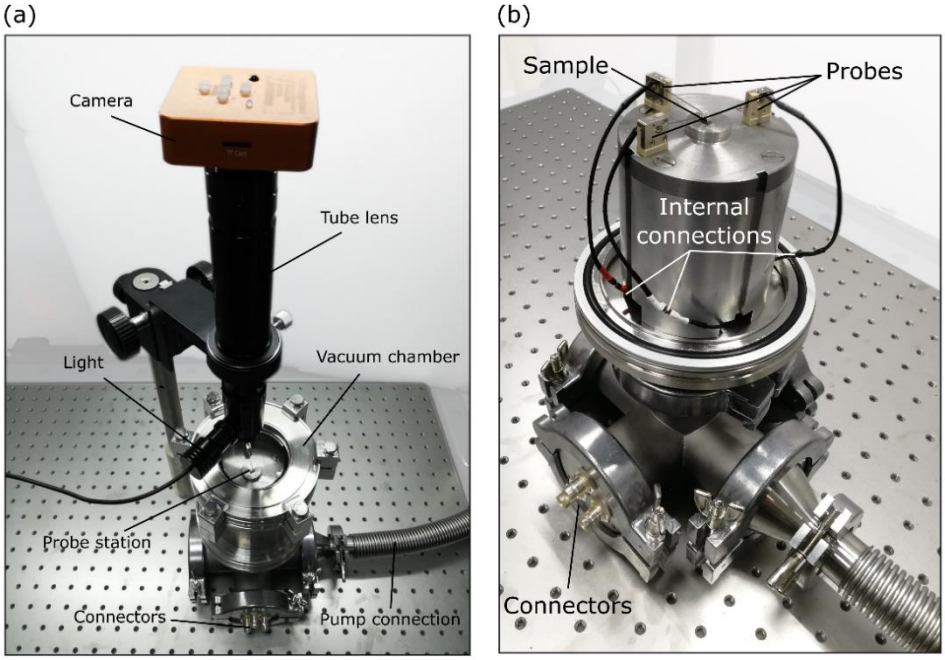

Figure 9. (a) Optical image of a home-made probe station to perform measurements in vacuum. The different components are pointed in the image. (b) Image of the probe station when the isolated chamber is opened. Here, the magnetic probes are mounted, and the sample stage can be observed.

We have demonstrated the flexibility that provides the decision of using a home-made probe station. This choice allows us to select the components to fit the purpose of the research and the budget for building the setup. So, different parameters can be easily adjusted like the number of probes, the integration of a heater/cooler or the possibility of controlling the atmosphere.

3.3.2.2 MoS_2 measurements under different environmental conditions

To prove the reliability of our home-made probe stations, we use the probe station shown in Figure 8 to characterize a MoS_2 device. As previously pointed, this setup allows us to measure under different environmental conditions. Thus, the MoS_2 device is characterized at $2.8 \cdot 10^{-6}$ mbar and atmospheric conditions.

The device is fabricated with a mechanically exfoliated MoS_2 single layer flake extracted from a bulk mineral of molybdenite (Moly Hill mine, Quebec). The MoS_2 flake is transfer to a SiO_2/Si substrate with pre-patterned Au/Ti electrodes by the deterministic transfer technique explained in C. Once the device was prepared, we

annealed the sample in vacuum in order to improve the electrical contact. The sample was annealed in vacuum during 8h at a temperature of 200 ºC.

Figure 10 shows the main measurements performed in the sample in both conditions: air (red) and vacuum (blue). We observe differences in all the cases between the measurement performed in air and in vacuum. The current versus bias voltage curves in Figure 10(a) have similar tendencies, showing the device slightly higher current values in air conditions. However, the behaviours in Figure 10(b) show a prominent contrast. The gate trace (measured at a bias voltage of 1 V) obtained in air conditions shows a big hysteresis, while the hysteresis in vacuum conditions is small. This phenomenon was previously studied by other groups, concluding that the hysteresis is produced due to the charge trapping of H_2O molecules in the MoS_2 surface and MoS_2/SiO_2 interface.[8,9]

Furthermore, the response time strongly depends on the environmental conditions too. Figure 10(c) shows the light response of the MoS_2 device by monitoring the current (applying a bias voltage of 1 V) while turning on and off a LED source with a wavelength of 420 nm and a power density of 3 μW/cm^2. We observe the slower response time obtained during the measurements in vacuum. These changes appear due to the traps recombination dynamic differences; while in air the presence of H_2O and O_2 molecules increases the recombination rate, this process is slow in vacuum due to the small molecules concentration.[10,11]

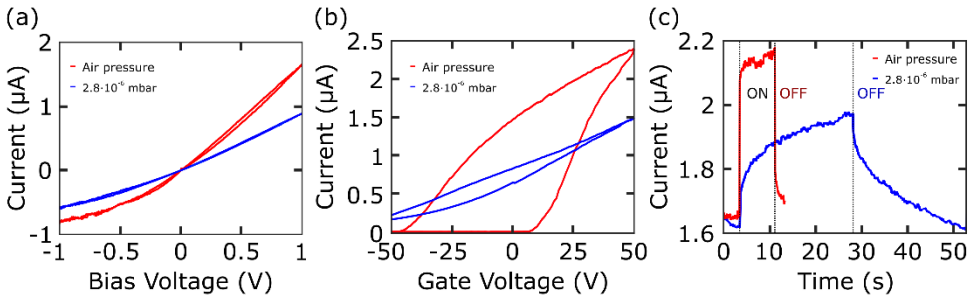

Figure 10. (a) Current versus bias voltage curves for a single-layer MoS_2 device measured in air conditions (red) and a pressure of $2.8 \cdot 10^{-6}$ mbar (blue). The measurements are performed in dark conditions and no gate voltage applied. (b) Gate traces measured in the same device at a bias voltage of 1 V in dark conditions. (c) Time traces recorded at an applied bias voltage of 1 V and no gate voltage applied. The LED used has a wavelength of 420 nm and a power density of 3 μW/cm^2. The light was turned on and off to observe the sample response.

The response time of the device was acquired in different light conditions in order to study the MoS_2 spectra and power density. Figure 11(a) shows the MoS_2 photocurrent measured at different wavelengths. This characterization was performed by illuminating the sample with fiber coupled LEDs (Thorlabs) of different wavelengths (420 nm, 470 nm, 530 nm, 565 nm, 595 nm, 660 nm and 740 nm) at the same power density of 3 μW/cm^2. We applied a bias voltage of 1 V while the LED was turning on and off, in order to obtain the current in dark and light conditions. The photocurrent spectrum measured in vacuum is slightly lower than the spectra obtained in air.

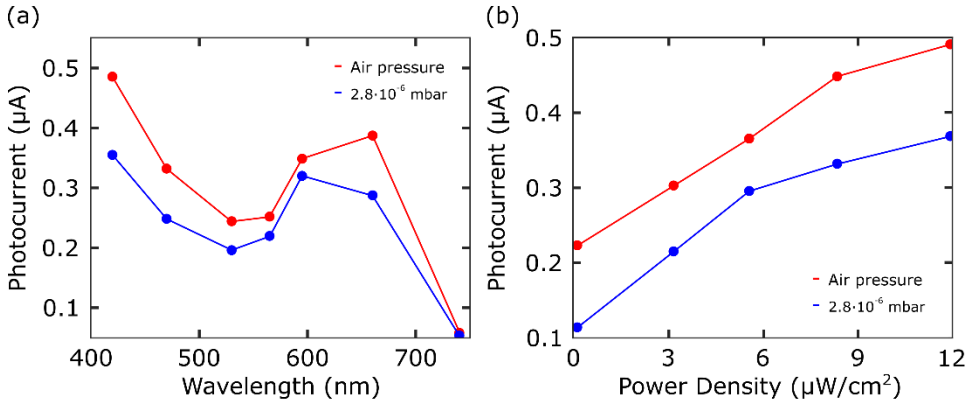

Figure 11. (a) Photocurrent spectra of the single-layer MoS_2 sample measured in air (red) and vacuum (blue) conditions. Each point corresponds to the photocurrent value calculated by subtracting the dark current to the current in light conditions. The measurements are time traces like the ones shown in Figure 12(c), measured with LEDs of different wavelengths (420 nm, 470 nm, 530 nm, 565 nm, 595 nm, 660 nm, 740 nm) and power density of 3 μW/cm^2. (b) Photocurrent dependency on the light power density of the single-layer MoS_2 sample measured in air (red) and vacuum (blue) conditions. Each point corresponds to the photocurrent value calculated by subtracting the dark current to the current in light conditions. The measurements are time traces like the ones shown in Figure 12(c), measured with a LED with a wavelength of 420 nm at different power densities (0.1 μW/cm^2, 3 μW/cm^2, 5.5 μW/cm^2, 8.4 μW/cm^2, 11.9 μW/cm^2).

We also studied the photocurrent dependency on the light power density. In this case, a LED with a wavelength of 420 nm was used for acquiring the data. The performed measurements are like the previous ones, in which the sample was measured at 1 V while turning on and off the light. The power density can be set with a power modulator attached to the LED, allowing us to measure at power densities of 0.1 μW/cm^2, 3 μW/cm^2, 5.5 μW/cm^2, 8.4 μW/cm^2 and 11.9 μW/cm^2. Here, the dependency on the power is different between the sample in air and in vacuum. The

sample in air shows a behaviour closer to the linear dependency, even though both traces show sub-linear tendencies.

3.4 Direct micro-probing to flakes

The techniques presented until now are well-known methods developed by the community in order to performed electrical characterization on 2D materials. Nevertheless, the method described in this section is a new technique developed in Andrés Castellanos Gómez laboratory and implemented by me in order to avoid some of the problems presented by the processes explained in the rest of the chapter.

The main goal of this technique is to provide a new tool for performing electrical measurements in 2D materials without the need of specialised equipment not accessible to any laboratory. In order to measure electronic properties in 2D samples, we already discussed the necessity of using nanofabrication techniques such as lithography or metal evaporation. These techniques are carried out in clean room facilities with the specific tools, which suppose a big investment specially for those institutions without a previous research on micro or nanoelectronics. For this reason, alternatives to the lithographic methods are being investigated to encourage the implementation of electrical measurements on 2D materials in material science laboratories. Nowadays the methods designed for substituting these techniques are mainly the direct metal evaporation through shadow/stencil mask[5,12–14] and microsoldering.[15,16] The first ones still use a metal evaporator and tools for stencil fabrication while the microsoldering requires an experienced user with very specific training.

The procedure used in this technique is similar to the operation of a normal atmospheric probe station, but the probes directly contact the flakes instead the electrode pads. The problem with the usual probe stations is the size of the probes used, which have a diameter of >25 µm. These dimensions are bigger than usual lateral size of a mechanically exfoliated flake. Another issue with the usual probes is their stiffness, which makes impossible to gently touch the samples without any damage. Reliable versions for 2D materials contacts of probe stations with nanoscopic probes have been developed, but it is necessary the use of accurate piezoelectric actuator and specialized microscopy systems (AFM, SEM or TEM) to inspect the gentle approach of the probes.[17–19] We have developed a setup with carbon fiber probes which does not require of elaborated microscopic methods or positioning techniques.

3.4.1 Setup

The setup is based on the probe station shown in Figure 7, but the probes used to contact the samples are made of polyacrylonitrile (PAN) carbon fibers.[20–23] These fibers have a very small diameter of 7 µm, as we can appreciate in Figure 12 (where a comparison between a carbon fiber and a human hair is shown), which allow us to place them very accurately in the flakes. Thus, the flakes can be electrically contacted by the carbon fibers probes directly.

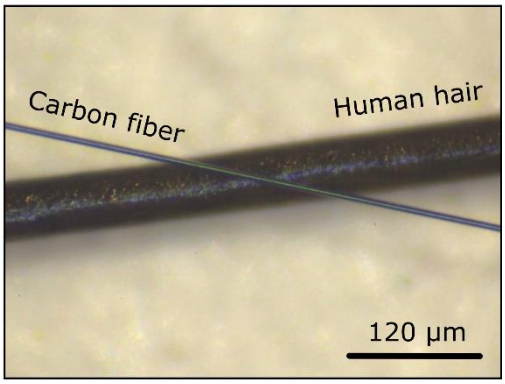

Figure 12. Comparison between a human hair and a PAN carbon fiber (7 µm of diameter) in the zoom lens.

The process followed to fabricate the carbon fiber probes is shown in Figure 13. First, we attached a surgical metallic needle to a square piece of copper board (PCB) and we wired it with a micro coaxial connection. The resulted probe was placed in the sample holder of the stamping setup used for fabrication of 2D samples, shown in Chapter 2.[24,25] Despite its low diameter, the carbon fiber is very long and easy to hold with tweezer, so we could operate the fiber without damaging it (see mechanical properties in the next section). The carbon fiber was stuck to a glass slide in order to transfer the carbon fiber completely straight in the needle tip. Once the carbon fiber was placed exactly where we wanted, we applied silver paint to the needle tip, which not only glue the carbon fiber but also improves the electrical contact. When the silver paint was dried, we cut the fiber from the glass slide with a nail cuticle nipper. This process is performed each time that we need a new probe, so there is no limit for the number of probes that we can fabricate.

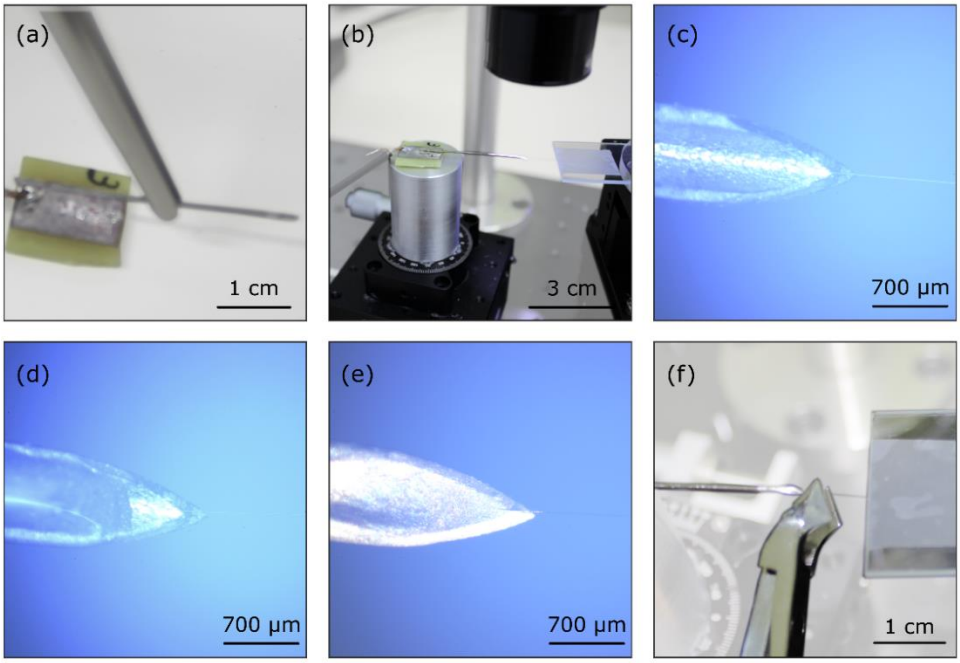

Figure 13. (a) Metallic needle welded to a PCB piece. (b) The piece with the needle is mounted in the deterministic transfer setup while a long carbon fiber is attached to the glass with tape. The glass slide is attached to an XYZ stage that allows the placement of the carbon fiber on the needle. This process is inspected by the zoom lens. (c) The carbon fiber is in contact with the metallic needle. (d) The carbon fiber is attached to the needle with one drop of silver paint. (e) The silver paint is already dry, so the carbon fiber is contacted with the needle. (f) The long carbon fiber is cut with a nail cuticle nipper.

After fabricating two probes, these are mounted in two XYZ micro-stages like the one displayed in Figure 14(b) to manipulate the tips positions. The stages are placed under a zoom lens with a camera attached as shown in Figure 14(a), allowing us to observe the flake and moving the carbon fiber tips toward the desire place on the flake. In order to prove the accuracy of the carbon fiber tips, we show in Figure 14(c) a MoS_2 flake contacted with two carbon fiber tips. The separation between the tips is 20 µm, being the minimun separation achieved in this setup of 10 µm.

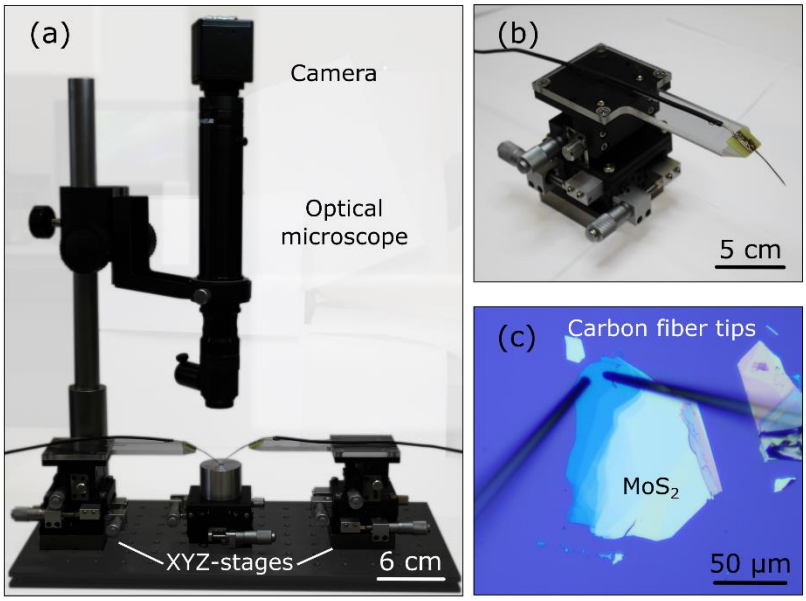

Figure 14. (a) Optical image of the two carbon fiber microprobes setup. (b) Detail of the XYZ micro-stage used to move the probes. (c) Optical image of two carbon fiber tips contacting a MoS_2 flake on SiO_2/Si.

3.4.2 Carbon fiber characterization

As mentioned before, the tips used during the experiments are PAN carbon fibers. In order to demonstrate their suitability for electrically contact the flakes, we studied their mechanical and electrical properties.

First, we need to assure that the carbon fibers are floppy enough to not damage the flakes if we push the fiber against the sample. The magnitude that provides information about the fibers flexibility is the spring constant. Considering the carbon fiber as cylindrical cantilevers, the spring constant is given by:[26]

$$k = \frac{r^4 \cdot E}{2 \cdot L^3 (1 - v^2)}$$

where k is the spring constant, r is the fiber radius (in our case 7 µm of diameter), E is the Young's modulus, L is the length (the typical probes length is 1 mm) and v is the Poisson's ratio. The E and v values are extracted from Reference [26] as the fibers used are the same, being $E = 246 \pm 8$ GPa and $v = 0.27$. We calculated then the spring constant, obtaining a value of $k \sim 0.02$ N/m. Thus, the tips do not damage the flakes when we contact them because the carbon fibers are quite flexible.

This flexibility of the fibers can also affects to the stability of the probes in the case of having mechanical resonance frequencies in the low range of 1-100 Hz. Acoustic noise and other laboratory vibrations have frequencies in that range, propitiating possible instabilities in the contact of ours probes. The frequency resonance is calculated again considering the carbon fiber tips as cylindrical cantilevers, reported in [26] as:

$$f = \frac{1}{2\pi}\sqrt{\frac{k}{m_{effect}}}$$

where f is the resonance frequency, k the spring constant and m_{effect} is the effective mass of the carbon fiber probe. This last parameter is given by:

$$m_{effect} = 0.243 \cdot \rho \cdot L \cdot \pi r^2$$

where ρ is the mass density (ρ = 1.71 ± 0.06 g/cm^3), extracted from the same Reference as well. The value obtained for the mechanical resonance is ~5.6 kHz, which is above the human voice range (up to 3.4 kHz), so the mechanical stability is not affected by the voices.

Other important parameters in electrical probes are the fiber electrical resistivity and the contact resistance with the flakes. In order to calculate these two parameters, we followed the procedure explained in Reference[26]. A carbon fiber was placed in a glass slide and silver paint drops were put along the fiber to facilitate the electrical contact. The resistance of the fiber was measured at different distances between the silver drops, obtaining the graph shown in Figure 15. Thus, the resistivity of the fiber and the contact resistance with a metal can be calculated by:

$$R = (\rho_{el} \cdot A^{-1}) \cdot L + 2R_C$$

where R is the resistance, ρ_{el} is the electrical resistivity, A is the cross section of the fiber, L is the distance between the silver paint drops measured and R_C is the contact resistance between the carbon fiber tip and the silver paint. As we can observe in Figure 15, the data follow a linear tendency in which the slope is 1.92·10-5 Ω·m. This value corresponds with the electrical resistivity of the carbon fiber, being the contact resistance between the carbon fiber and the silver paint 80 Ω.

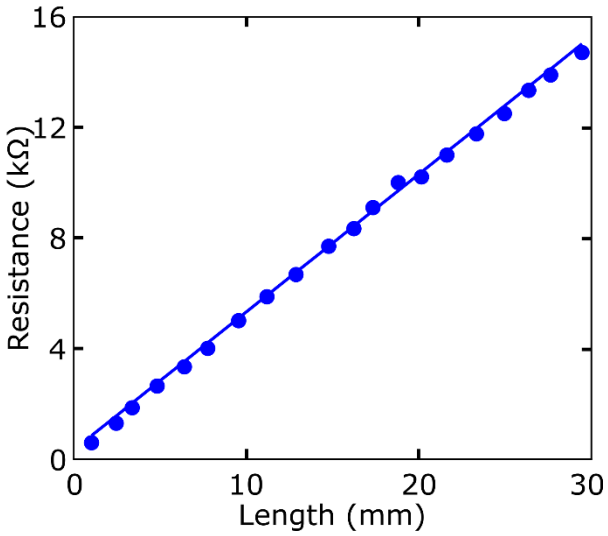

Figure 15. The resistance measured between silver drop contacts at different distances in the carbon fiber.

Once the contact resistance with a metal was obtained, we also needed to determine the contact resistance of the carbon fiber tip with a 2D material, because these fibers are used to contact flakes. We chose in this case a TiS_3 nanoribbon to determine the contact resistance. TiS_3 is a 2D materials that grows in nanoribbon shape, allowing us to have homogeneous channel width. This characteristic facilitates the determination of the distance between both contacts with the flake. In this case, two carbon fibers were used to contact directly the sample and current versus voltage curves were measured to extract the resistance, as shown in Figure 16. We obtained for the contact resistance of the carbon fiber with the flake a value of 33.1 kΩ (or 8.3 Ω·cm). If we compare this value with the contact resistance between a trilayer MoS_2 and Au electrodes reported,[27] we observe that both are in the same range.

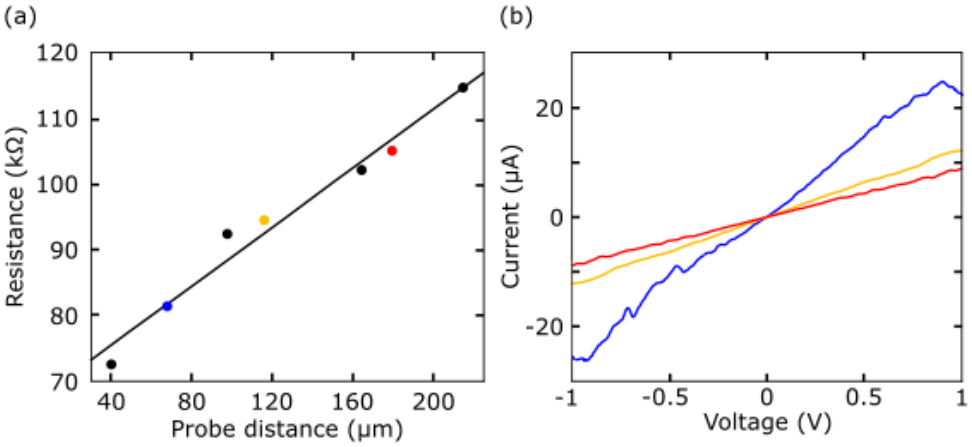

Figure 16. (a) Resistance measured in a TiS_3 nanoribbon at different distances between the two carbon fiber probes. (b) Current versus voltage curves recorded in order to measure the resistance at different distances in the flake.

Finally, Figure 17 shows the monitoring of the current over the time while we approached a carbon fiber tip to a SiO_2/Si substrate with Au coating. The Au substrate and the carbon fiber probe were connected to a Keithley 2450 source-meter that allowed us to apply certain voltage and measure the current. So, the carbon fiber tip was lowered until it reached the Au surface, closing the circuit and showing a certain current flow.

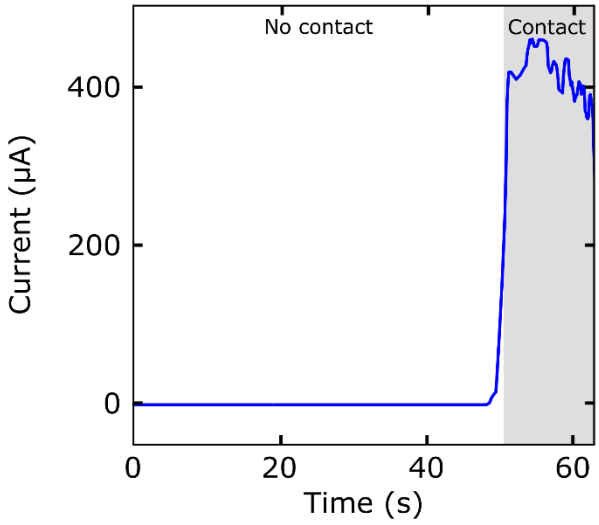

Figure 17. Current measurement while the probe is contacting the Au substrate, being the fluctuations due to the manual manipulation with the micro-stage.

3.4.3 Sample fabrication

To test this electrical contacting technique, we fabricated several samples with different 2D materials, following the same procedure for all of them. The MoS_2 was extracted from a bulk natural mineral from Moly Hill mine (Quebec, Canada), the TiS_3 used was synthesized by the same process described in Reference [28] and was provided by I.J. Ferrer and J.R. Ares, the black phosphorus was bought in Smart Elements and the WS_2 and WSe_2 are natural crystals provided by R. Bratschitsch. In order to obtain flakes from these bulk crystals, we mechanically exfoliated them with Nitto tape (SPV) several times as already explained in C. In the last exfoliation step, we used a PDMS stamp to obtain thin layers of material. After the exfoliation, the PDMS stamps were inspected in the optical microscope to select a flake. In the case of the MoS_2 flakes, differential reflectance spectra were measured to determine the number of layers of the flake.[29] The chosen flakes were transferred with the deterministic transfer method described in C to different substrates: Au and Si for the sample prepared in the section 3.2.4 and SiO_2/Si for the rest of the samples.[24,25]

3.4.4 Vertical measurements

The setup was tested by measuring samples with a single probe contact, so vertical devices were fabricated to measure electrical transport in the out-of plane direction. The first sample was a MoS_2 flake with areas of different thicknesses transferred on Au substrate. In Figure 18(a), there is a scheme of the setup configuration in which we can observe how the carbon fiber and the Au substrate are connected to the source-meter. Once the carbon fiber contacts the flake, we measure the resistance of the MoS_2 flake in the c-axis. The optical image of the sample is shown in Figure 18(b), in which inset we can also observe the sample contacted by the carbon fiber probe. The sample was contacted in four different areas: monolayer, bilayer, trilayer and multilayer. In each area, a current versus voltage curve was measured in order to obtain an electrical characterization and calculate the resistance of the MoS_2 for different thicknesses. The resistance values were obtained considering the resistance of the fiber probe, which was subtracted to the total resistance. Thus, the fiber was previously contacted to the Au substrate to measure the probe resistance with an IV trace ($R = 800 \pm 50\ \Omega$). Figure 18(c) displays the IVs recorded, which show a lower resistance for the monolayer and exponentially higher resistance for the rest of the thicknesses of the flake. This behaviour of the MoS_2 is compatible with a tunnelling barrier,[30] in which the width of the barrier depends on the number of layers of the flake.

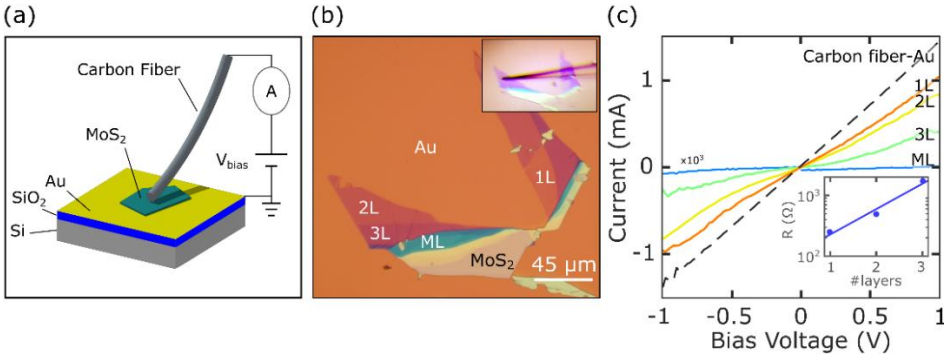

Figure 18. (a) Illustration of the MoS_2 flake transferred on Au substrate and the electrical connections to measure with the carbon fiber. (b) Optical image of the MoS_2 flake with different thicknesses on Au. Inset: Carbon fiber contacting the bilayer area of the flake. (c) Current versus bias voltage measured in the areas marked in (b). Inset: Resistance extracted from the IVs at bias voltage of 1V, subtracting the fiber resistance.

The next sample measured with one carbon fiber probe was a p-n junction between a single-layer MoS_2 and p-type silicon. An illustration of the setup and the sample is shown in Figure 19(a), similarly to the scheme of Figure 18(a). Here, we observe the connections from the Si and the carbon fiber probe to the source-meter while the MoS_2 is contacted by the carbon fiber tip. It was already reported that MoS_2, which is a n-type semiconductor, forms a p-n junction in contact with p-type Si.[31–35] In Figure 19(b), we see an optical image of the sample measured (a transmission image of the flake before the transfer is shown in the inset to facilitate the inspection). The single-layer area marked in Figure 19(b) is contacted by the carbon fiber probe to perform the measurements. IVs in dark conditions (black line) and under illumination with a white LED source (blue line) were obtained. As it can be observe in Figure 19(c), the black curve shows a rectifying behaviour which is characteristic from a diode. The increase of the open-circuit voltage (~0.15 V) and short-circuit current (~5 nA) is also the proper behaviour of a photovoltaic photocurrent generation mechanism of a p-n junction.

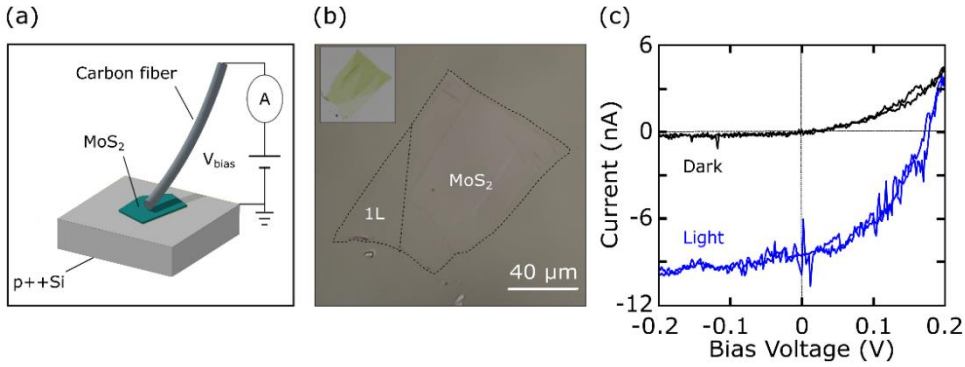

Figure 19. (a) Illustration of the n-type MoS_2 flake transferred on p-type Si substrate and the electrical connections set for the measurements. (b) Optical image of the sample of MoS_2 transferred on Si. Inset: Transmission image of the MoS_2 flake to facilitate the recognition. (c) Current versus voltage curves for the p-n junction fabricated, measured in dark conditions (black trace) and under illumination with white light (blue).

3.4.5 Phototransistor measurements

Once we finished with the measurements of one carbon fiber probe, we had to test the performance of two carbon fiber tips. The measurements done with this aim are the characterization of the phototransistor properties in a MoS_2 trilayer. In Figure 20(a), there is a schematic image of the setup and the electrical configuration. In this case, we have connected both probes to the source-meter to apply a voltage difference between two points on the sample surface with the tips.

The MoS_2 flake was transferred on SiO_2/Si wafer, which allows us to establish a back-gate voltage between the Si of the substrate and one of the carbon fiber tips to perform electric field effect measurements.[36] An optical image of the sample is shown in Figure 20(b), where the trilayer region contacted is marked. We observe in the inset how this region was probe by the two carbon fiber tips. Current versus voltage characteristics were recorded for different gate voltages applied in the MoS_2 trilayer, as shown in Figure 20(c). We extracted the current measured at a bias voltage of 1 V for each gate voltage applied, obtaining the inset of Figure 20(c). Here, it can be appreciated the dependency of the current with the gate voltage, which shows a characteristic behaviour of a n-type semiconductor.[36] Thus, the current increases with the increment of gate voltage while it decreases for negative voltage, being completely switch off at negative gate voltages of ~-20 V. Moreover, the transistor configuration presents an ON-OFF current ratio of ~150 at a bias voltage of 1 V.[37] This last value is comparable to those reported in the literature for trilayer

MoS_2 measured at similar conditions. We can also estimate from the gate trace the mobility of the transistor, which is between 1.3 and 3.3 $cm^2/(V \cdot s)$. This uncertainty in the mobility calculation is due to the width and length channel determination. The mobilities reported in literature for trilayer MoS_2 devices fabricated with lithography range from 0.5 to 10 $cm^2/(V \cdot s)$. These values of the trilayer MoS_2 mobility are compatible with the data reported by the literature.[36–39] In order to reduce the uncertainty in the mobility calculation, four probes with a van der Pauw configuration can be disposed to better obtain the channel dimensions and the contact resistance.

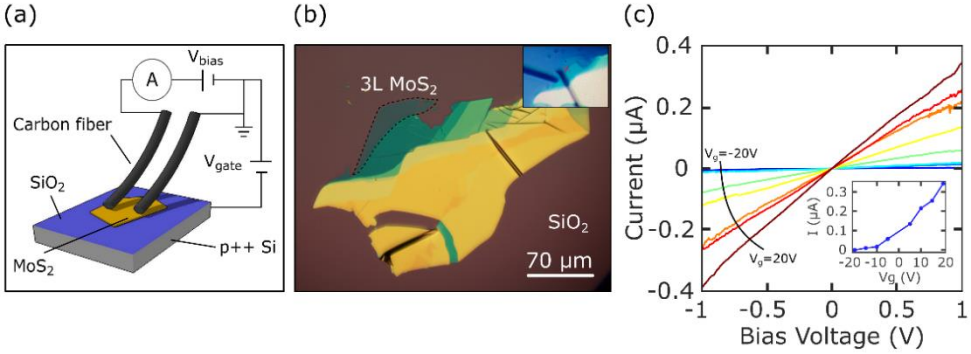

Figure 20. (a) Illustration of the MoS_2 flake on SiO_2/Si substrate and the electrical connection to measure with two carbon fiber probes. (b) Optical image of the MoS_2 flake on SiO_2, being the marked area the trilayer measured. Inset: MoS_2 trilayer contacted by two carbon fiber probes. (c) Current versus bias voltage traces measured at different gate voltages applied, ranging from -20 V to 20 V. Inset: Current extracted from the IVs at a bias voltage of 1 V for each gate voltage.

We also can use the same configuration employed for field-effect measurement (shown in Figure 20(a)) to perform measurements of the MoS_2 response to the light. The probes leave the semiconductor channel exposed thanks to their small size. Thus, the channel can be illuminated allowing us to measure the photodetection or the chemical sensing of our flake.[40] We tested the response to the illumination of our MoS_2 trilayer, studying the light power and wavelength dependencies of the sample.[41,42]

Figure 21(a) shows the current versus voltage traces for the MoS_2 under illumination with a LED source with 455 nm of wavelength. Each curve corresponds to different power density of the light. From these data, we extracted the current measured at a bias voltage of 10 V in order to observe the photocurrent dependency on the

illumination power. This dependency is linear, as it can be observed in the inset of the Figure 21(a)

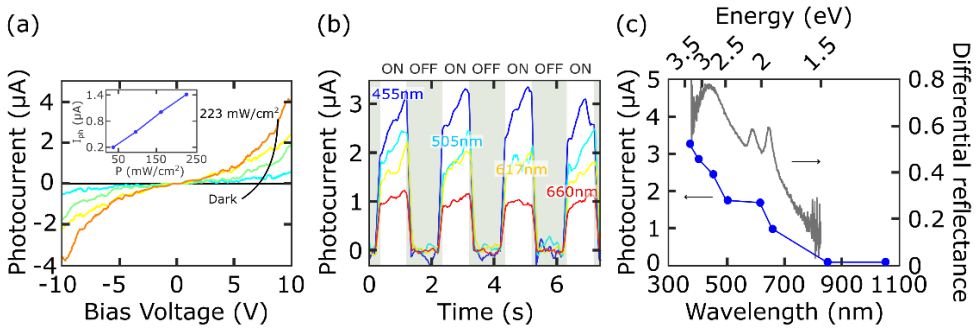

Figure 21. (a) Photocurrent versus bias voltage traces measured under illumination with light wavelength of 455 nm at different power densities. Inset: Photocurrent extracted from the IVs at bias voltage of 10 V for each light power density. (b) Response time measurements under illumination with LED sources of 455 nm (dark blue), 505 nm (light blue), 617 nm (yellow) and 660 nm (red) at fixed power density of 160 mW/cm^2 and bias voltage of 10 V. (c) Photocurrent spectrum extracted from measurements at bias voltage of 10V and power density of 140 mW/cm^2. The differential reflectance spectrum of MoS_2 flake is shown in the same graph.

The next experiment carried out was performed in order to study the photodetection response at different wavelengths. The bias voltage was set at 10 V while the illumination was modulated with a square function, having the ON state a power density of 160 mW/cm^2. The response time of the photodetector can be obtained from these data, being ~100 ms for all the wavelengths. This value of the photodetection response time is in the range of the reported results (from μs[39,43] to s[44,45]) for MoS_2 photodetectors. From the measurements at different wavelengths at fixed power density, one can extract the photocurrent spectrum of the photodetector. The photocurrent spectrum of the photodetection is related to the absorption spectrum of the MoS_2 flake. In order to facilitate the comparison, we plotted the differential reflectance spectrum measured prior the transfer (related to the absorbance) in the Figure 21(c) together with the photocurrent spectrum. We can observe that the photocurrent spectrum shows a peak in the area where the differential reflectance spectrum shows the A and B excitonic resonances.[46] Moreover, the photocurrent spectrum follows the same behaviour than the differential reflectance spectrum in the studied wavelength range. The photocurrent data also allow us to calculate the responsivity of the MoS_2 by:

$$R = \frac{I_{ph}}{P_{den} \cdot A_{chan}}$$

where R is the responsivity, I_{ph} is the photocurrent, P_{den} is the light power density and A_{chan} is the area of the semiconductor channel. Our sample reaches 26 A/W, which is in the range of conventional MoS_2 photodetectors measured at similar light and bias conditions previously reported by the literature.[44]

3.4.6 Reproducibility of the measurements and stability of the contact

One big difference between using conventional contacts made by lithographic techniques and measuring directly with carbon fiber tips is the stability of the established contact. The contact between the carbon fiber and the flake changes due to mechanical vibrations during certain measurement, unlike the conventional metallic electrodes. Likewise, the contact is different from measurement to measurement (different spot on the flake surface, different pressure applied to the contact, …), which does not occur in samples with conventional metallic electrodes. Due to the possible contact shift produced along the measurements, we need to characterize the reproducibility and stability of the measurements performed by the carbon fiber probes.

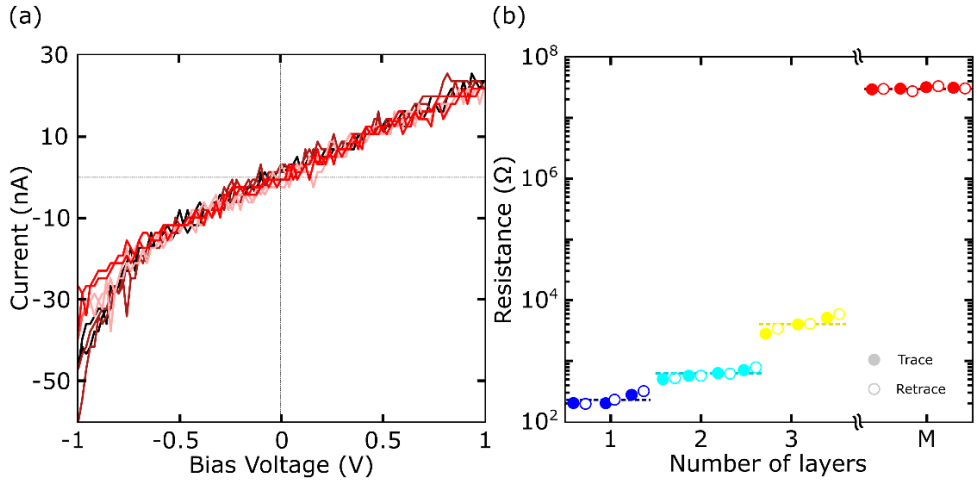

Figure 22. (a) Current versus voltage curves measured in the out-of-plane direction of a MoS_2 multilayer region transferred on Au substrate with one carbon fiber probe. The graph shows the trace and the retrace for each measurement. (b) Resistance calculated from the IVs measured in regions with different thicknesses of the MoS_2 flake on Au substrate, using the same configuration with one carbon fiber probe. The filled circles correspond to the trace and the unfilled circles to the retrace.

The first test performed in the sample was the measurement of current versus voltage characteristics on different areas of a MoS_2 flake transferred on Au substrate. One carbon fiber probe and the Au substrate were connected to the source-meter while the carbon fiber tip was probing the MoS_2 sample, similarly to the scheme of the Figure 18(a). The current flow across the out-of-plane direction of the flake (c-axis of MoS_2) was recorded few times in order to study the reproducibility. In Figure 22(a), we show four IVs measured in a multilayer area of the MoS_2 sample (trace and retrace in each measurement), finding a good reproducibility from curve to curve. We extracted the resistance of each area of the flake from IVs measured along the sample with different number of layers, as shown in Figure 22(b). There are some differences between the values calculated from each trace or retrace, probably due to the mechanical vibration of the setup. These vibrations were produced because of the lack of isolation of the setup (the setup was situated in a normal desk without any cover), so the reproducibility can be improved by introducing some changes in the setup isolation.

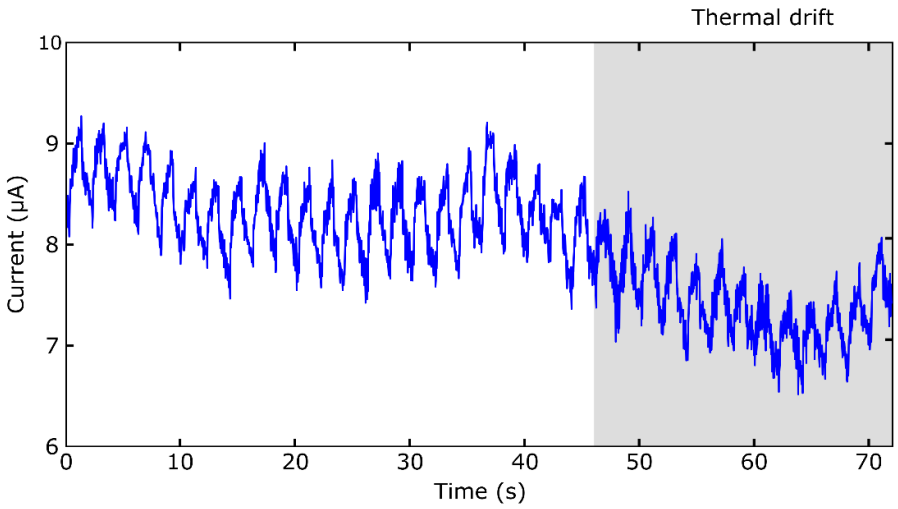

Figure 23. Time trace of the MoS_2 sample transferred on Au substrate and measured in the out-of-plane direction with one carbon fiber probe. The bias voltage is kept at 10 V and the illumination is modulated with a square signal in a LED source of 505 nm with a power density of 160 mW/cm^2.

One the other hand, we also performed long time traces in order to observe the stability of the carbon fiber probes. Photodetection of the MoS_2 sample was acquired during more than one minute, maintaining a bias voltage of 10 V and illuminating the sample with square-modulated light of 505 nm with a power density of 160 mW/cm^2. We observe in Figure 23 that the measurement was stable for 10-20 s.

However, the trace started to shift at certain point because air flow produces the tip drifts. This problem could be also improve by a better isolation of the setup.

3.4.7 Reliability

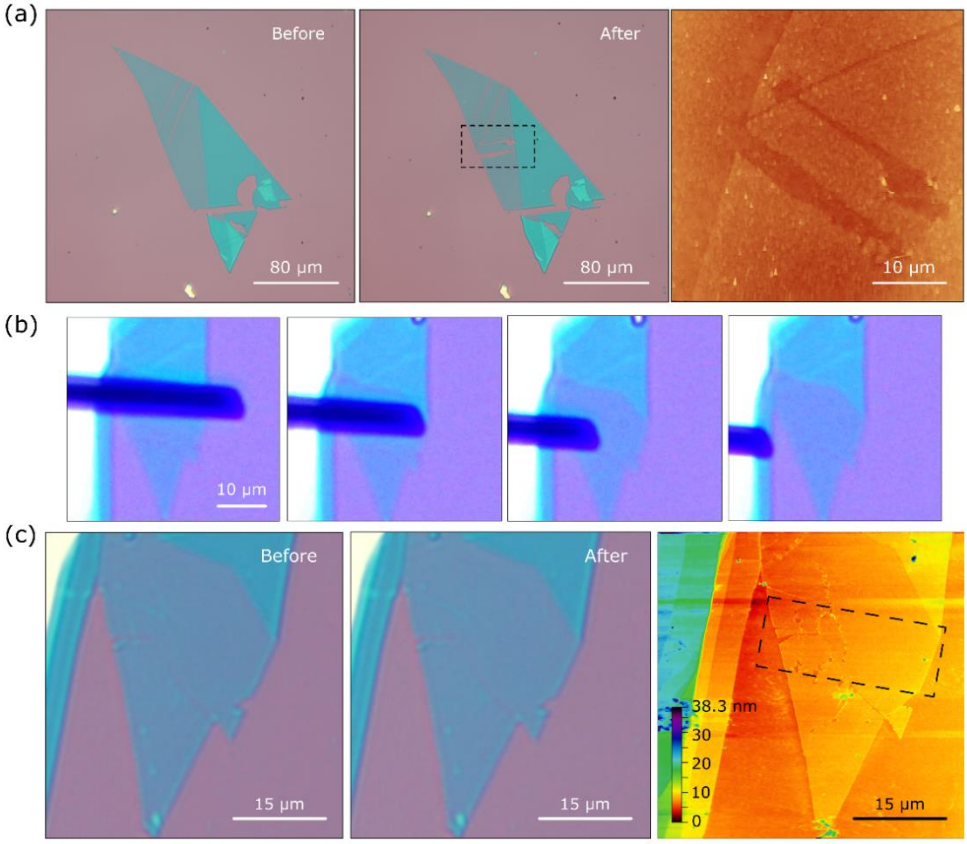

Figure 24. (a) Optical images with better resolution of the flake before and after sweeping with a metallic wire. The last panel is the AFM image acquired after sweeping with the metallic wire. (b) Optical images of a carbon fiber sweeping a MoS_2 monolayer area. (c) Optical images with better resolution of the flake before and after sweeping. The last panel is the AFM image acquired after sweeping with the carbon fiber tip.

Carbon fiber probes proved to be suitable for optoelectronic characterization of 2D materials, as we showed in the previous sections. Moreover, we also aim to assure the gentleness of the probing, showing that our carbon fibers do not produce any damage to the flakes. So, we used one carbon fiber to sweep the surface of a single-layer MoS_2 area, as it can be observed in Figure 24(a). Optical microscopy images were acquired before and after the process, we do not observe any difference between

them. AFM characterization was also performed for inspecting the possible changes between before sweeping and after sweeping the sample. The image after sweeping is shown in Figure 24(b), where any noticeable scratch was found in the surface of the flake. We tried to follow the same process with a 10 mm of diameter metal wire, in order to inspect the possibility of using them instead of carbon fibers, but the wire damage and scratch the flakes.

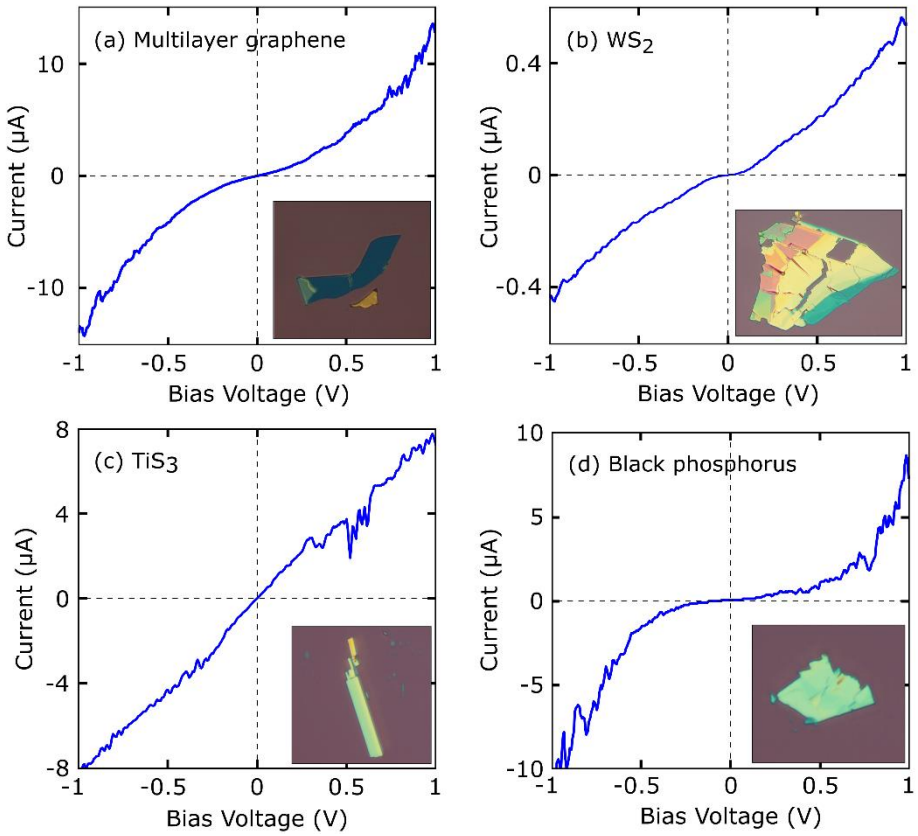

Figure 25. Current versus bias voltage characteristics measured in flakes of (a) multilayer graphene flake, (b) WS_2 flake, (c) TiS_3 flake and (d) black phosphorus.

In order to show the reliability of this technique for probing any 2D material, we also measure other materials apart of MoS_2. We use again the configuration of two carbon fiber tips to measure IVs in the in-plane direction of the different flakes. The results are shown in Figure 25, in which the materials measured are: multilayer graphene, the most remarkable and well-known 2D material; WS_2, a member of the same family of MoS_2 (TMDCs); TiS_3, a transition metal trichalcogenide; and black phosphorus, belonging to a different 2D materials group. We did not find any

problem in contacting all these materials with two carbon fiber probes and measure the current versus voltage characteristics, demonstrating the versatility of this method and the possibility of extending it to any 2D material.

3.5 Conclusions

The electrical characterization of 2D materials requires of specific techniques and methods in order to perform measurements on the flakes. Along this chapter, we review different approaches for contacting 2D materials. In order to electrically contact the flakes, metallic electrodes are usually patterned on the substrate surface. The electrodes can be patterned before or after the transfer of the flake, which usually determines the technique used for patterning. The most common methods for pre-patterning electrodes are the photolithographic techniques and the shadow masks meanwhile the e-beam lithography is commonly used for patterning electrodes on a transferred flake.
Once the flake is contacted by metallic electrodes, we need to connect these electrodes with external electronics. There are two well-known techniques to contact the electrodes: the wire bonding and the micro-probing with a probe station. The wire bonding requires of certain expertise to apply the right parameters to create a bond without damaging the electrodes. Micro-probing with the tips of a probe station can be very gentle, avoiding unintentional damages on the electrodes. On the other hand, the number of probes available in a probe station limiting the number of electrical connections. With wire bonding one can easily make as many bonds as need.

Another completely different method is the direct probing of the flakes, in which the carbon fiber probes are also the electrodes. This technique allows us to avoid the electrodes patterning process while making the electrical connection of the flakes with the source-meter as easy as operating a probe station. The main difference is the gentleness and the low diameter of the probes, which are required characteristics to perform the microprobing. Although this method is very convenient for certain experiments, there are some disadvantages with respect to the common techniques, like the stability of the contact.

So, the choice between the use of different techniques and methods strongly depends on the characteristics of the experiment. Each method has advantages and disadvantages that need to be study in order to accomplish the requirements of the research.

References

1. Ito, T. & Okazaki, S. Pushing the limits of lithography. *Nature* **406**, 1027–1031 (2000).
2. Susi, T., Meyer, J. C. & Kotakoski, J. Manipulating low-dimensional materials down to the level of single atoms with electron irradiation. *Ultramicroscopy* **180**, 163–172 (2017).
3. Altissimo, M. E-beam lithography for micro-/nanofabrication. *Biomicrofluidics* **4**, (2010).
4. Pimpin, A. & Srituravanich, W. Reviews on micro- and nanolithography techniques and their applications. *Engineering Journal* **16**, 37–55 (2012).
5. Tien, D. H., Park, J.-Y., Kim, K. B., Lee, N. & Seo, Y. Characterization of graphene-based FET fabricated using a shadow mask. *Sci. Rep.* **6**, 25050 (2016).
6. Bao, W. *et al.* Lithography-free fabrication of high quality substrate-supported and freestanding graphene devices. *Nano Res.* **3**, 98–102 (2010).
7. Chauhan, P. S., Choubey, A., Zhong, Z. & Pecht, M. G. Copper Wire Bonding. in *Copper Wire Bonding* 1–9 (Springer New York, 2014).
8. Late, D. J., Liu, B., Ramakrishna Matte, H. S. S., Dravid, V. P. & Rao, C. N. R. Hysteresis in Single-Layer MoS_2 Field Effect Transistors. (2012).
9. Di Bartolomeo, A. *et al.* Hysteresis in the transfer characteristics of MoS_2 transistors. *2D Mater.* **5**, (2018).
10. Khan, M. F. *et al.* Photocurrent Response of MoS_2 Field-Effect Transistor by Deep Ultraviolet Light in Atmospheric and N_2 Gas Environments. (2014).
11. Khan, M. F., Nazir, G., Lermolenko, V. M. & Eom, J. Electrical and photo-electrical properties of MoS_2 nanosheets with and without an Al_2O_3 capping layer under various environmental conditions. *Sci. Technol. Adv. Mater.* **17**, 166–176 (2016).
12. Yun, H. *et al.* Stencil nano lithography based on a nanoscale polymer shadow mask: towards organic nanoelectronics. *Sci. Rep.* **5**, 10220 (2015).
13. Yong, K., Ashraf, A., Kang, P. & Nam, S. Rapid stencil mask fabrication enabled one-step polymer-free graphene patterning and direct transfer for flexible graphene devices. *Sci. Rep.* **6**, 24890 (2016).
14. Bao, W. *et al.* Lithography-free fabrication of high quality substrate-supported and freestanding graphene devices. *Nano Res.* **3**, 98–102 (2010).
15. Girit, Ç. Ö. & Zettl, A. Soldering to a single atomic layer. *Appl. Phys. Lett.* **91**, 193512 (2007).
16. Geringer, V. *et al.* Electrical transport and low-temperature scanning tunneling microscopy of microsoldered graphene. *Appl. Phys. Lett.* **96**, 1–4 (2010).
17. Hanson, E. D. *et al.* Systematic study of oxygen vacancy tunable transport properties of few-layer MoO_{3-x} enabled by vapor-based synthesis. *Adv.*

Funct. Mater. 1605380 (2017).
18. Baringhaus, J. *et al.* Exceptional ballistic transport in epitaxial graphene nanoribbons. *Nature* **506**, 349–354 (2014).
19. Yakes, M. K. *et al.* Conductance anisotropy in epitaxial graphene sheets generated by substrate interactions. *Nano Lett.* **10**, 1559–1562 (2010).
20. Perret, R. & Ruland, W. The microstructure of PAN-base carbon fibres. *J. Appl. Crystallogr.* **3**, 525–532 (1970).
21. Huang, X. Fabrication and properties of carbon fibers. 2369–2403 (2009).
22. Castellanos-Gomez, a, Agraït, N. & Rubio-Bollinger, G. Carbon fibre tips for scanning probe microscopy based on quartz tuning fork force sensors. *Nanotechnology* **21**, 145702 (2010).
23. Castellanos-Gomez, A. *et al.* Carbon tips as electrodes for single-molecule junctions. *Appl. Phys. Lett.* **99**, 1–11 (2011).
24. Castellanos-Gomez, A. *et al.* Deterministic transfer of two-dimensional materials by all-dry viscoelastic stamping. *2D Mater.* **1**, 011002 (2014).
25. Frisenda, R. *et al.* Recent progress in the assembly of nanodevices and van der Waals heterostructures by deterministic placement of 2D materials. *Chem. Soc. Rev.* **47**, 53–68 (2018).
26. Castellanos-Gomez, A. A simple method to characterize the electrical and mechanical properties of micro-fibers. **34**, 1547–1554 (2013).
27. Li, S.-L. *et al.* Thickness scaling effect on interfacial barrier and electrical contact to two-dimensional MoS_2 layers. *ACS Nano* **8**, (2014).
28. Ferrer, I. J., Maciá, M. D., Carcelén, V., Ares, J. R. & Sánchez, C. On the Photoelectrochemical Properties of TiS_3 Films. *Energy Procedia* **22**, 48–52 (2012).
29. Frisenda, R. *et al.* Micro-reflectance and transmittance spectroscopy: A versatile and powerful tool to characterize 2D materials. *J. Phys. D. Appl. Phys.* **50**, (2017).
30. Popov, I., Seifert, G. & Tománek, D. Designing electrical contacts to MoS_2 monolayers: a computational study. *Phys. Rev. Lett.* **108**, 1–5 (2012).
31. Li, Y., Xu, C.-Y., Wang, J.-Y. & Zhen, L. Photodiode-like behavior and excellent photoresponse of vertical Si/monolayer MoS_2 heterostructures. *Sci. Rep.* **4**, 7186 (2014).
32. Hao, L. *et al.* Electrical and photovoltaic characteristics of MoS_2/Si p-n junctions. *J. Appl. Phys.* **117**, (2015).
33. Wang, L. *et al.* MoS_2/Si heterojunction with vertically standing layered structure for ultrafast, high-detectivity, self-driven visible-near infrared photodetectors. *Adv. Funct. Mater.* **25**, 2910–2919 (2015).
34. Lopez-Sanchez, O. *et al.* Light generation and harvesting in a van der Waals heterostructure. *ACS Nano* **8**, 3042–3048 (2014).
35. Tsai, M.-L. *et al.* Monolayer MoS_2 Heterojunction Solar Cells. *ACS Nano* **8**, 8317–8322 (2014).
36. Radisavljevic, B., Radenovic, A., Brivio, J., Giacometti, V. & Kis, A. Single-layer MoS_2 transistors. *Nat. Nanotechnol.* **6**, 147–50 (2011).

37. Furchi, M. M., Polyushkin, D. K., Pospischil, A. & Mueller, T. Mechanisms of photoconductivity in atomically thin MoS_2. *Nano Lett.* **14**, 6165–6170 (2014).
38. Novoselov, K. S. *et al.* Two-dimensional atomic crystals. *Proc. Natl. Acad. Sci. U. S. A.* **102**, 10451–3 (2005).
39. Wu, C. C. *et al.* Elucidating the photoresponse of ultrathin MoS_2 field-effect transistors by scanning photocurrent microscopy. *J. Phys. Chem. Lett.* **4**, 2508–2513 (2013).
40. Koppens, F. H. *et al.* Photodetectors based on graphene, other two-dimensional materials and hybrid systems. *Nat Nanotechnol* **9**, 780–793 (2014).
41. Choi, W. *et al.* High-detectivity multilayer MoS_2 phototransistors with spectral response from ultraviolet to infrared. *Adv. Mater.* **24**, 5832–5836 (2012).
42. Yin, Z. *et al.* Single-layer MoS_2 phototransistors. *ACS Nano* **6**, 74–80 (2012).
43. Tsai, D. S. *et al.* Few-layer MoS_2 with high broadband photogain and fast optical switching for use in harsh environments. *ACS Nano* **7**, 3905–3911 (2013).
44. Lopez-Sanchez, O., Lembke, D., Kayci, M., Radenovic, A. & Kis, A. Ultrasensitive photodetectors based on monolayer MoS_2. *Nat. Nanotechnol.* **8**, 497–501 (2013).
45. Zhang, W. *et al.* High-gain phototransistors based on a CVD MoS_2 monolayer. *Adv. Mater.* **25**, 3456–3461 (2013).
46. Splendiani, A. *et al.* Emerging Photoluminescence in Monolayer MoS_2. *Nano Lett.* **10**, 1271–1275 (2010).

4. Strain tunable single-layer MoS_2 photodetector

4.1 Introduction

Electronic devices are characterized by the presence of an external knob that allows to manipulate and control their performance. The most common example is the field-effect transistor, in which the conductance can be tuned by applying an electric field between the gate and the drain electrodes.[1–5] This trend continues nowadays, so the researchers are studying other external knobs to develop new designs for devices like in the case of valleytronics or spintronics.[6–11]

In this chapter, we explore the possibility of using strain engineering as a tuning knob for varying the optoelectrical behaviour of MoS_2 photodetectors. Strain engineering has already proven to produce the modification of the optoelectronic properties when the materials are grown with certain stress respect to their original lattice.[12–15] This conventional approach provides fixed values of strain to the materials without the possibility of modifying the strain level. Moreover, the strain levels achieved are small due to the brittle of the materials. After the isolation of 2D materials, the paradigm of strain engineering changed completely thanks to the flexibility of these materials. The low presence of defects and the lack of dangling bonds in the surface of 2D materials allow to stretch and bend them at large levels compare with 3D materials without damaging them. Furthermore, the strain is reversible in these materials due to their flexibility, which means a new way to use strain engineering.[16–20]

There have been several optical studies on 2D materials in which the samples were measured with different levels of applied strain. In the case of transition metal dichalcogenides, we already explained in Chapter 1 that tensile uniaxial (or biaxial) strain produce a reduction in the bandgap. [21–27] During our experiments, we used single-layer MoS_2 photodetectors, so the bandgap modification is observed in the photodetector performance. Unlike the experiments explained in other works,[28,29] the aim of this study is the adjustment of the photodetector bandwidth with the application of strain. Thus, we obtained a device in which we can select the operation mode by selecting the percentage of applied strain, opening the possibility of using

it as an external knob. This technique can be extended to other 2D materials, in which the modifications would depend on the band structure evolution produced by the application of strain. Black phosphorus, for example, is another 2D material in which the bandgap changes introduced by strain are more noticeable than the ones observed in MoS_2.[30–32]

4.2 Fabrication process

The photodetectors measured along the experiments use MoS_2 flakes mechanically exfoliated from a bulk natural crystal of molybdenite (Moly Hill mine, Quebec, Canada) with the technique previously explained in Chapter 3. Prior to the transfer of the flakes, transmittance measurements (see Chapter 2 and [33]) were performed in the flakes to determine the number of layers of the material in order to select the single-layer areas of MoS_2.[34] Once we identify a single-layer MoS_2, it was determiniscally transferred between pre-patterned Au/Ti electrodes by the method explained in Chapter 3.[35,36] These electrodes were previously fabricated on polycarbonate (PC) substrate by electron-beam evaporation through an Ossila® shadow mask (E324). Finally, the resulting device was annealed at 100 ºC to improve the contact between the flake and the electrodes. An example of a single-layer MoS_2 device can be observed in Figure 1b.

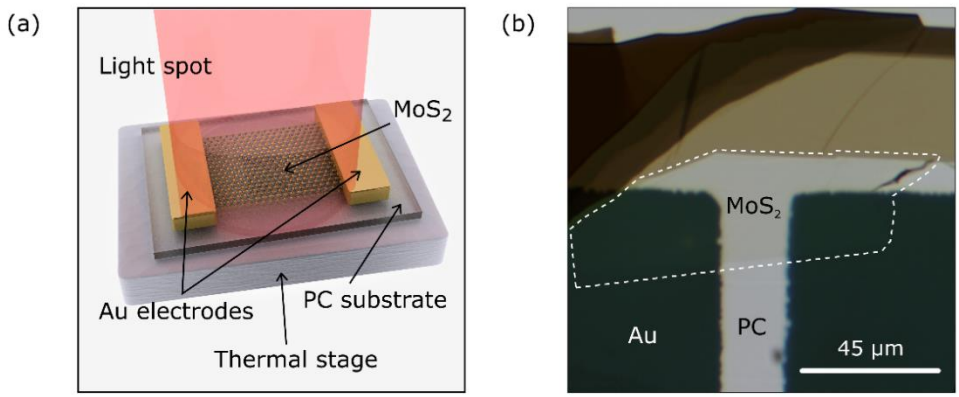

Figure 1. (a) Schematic representation of the single-layer MoS_2 photodetectors configuration and the setup in which the measurements were performed. There is a thermal stage underneath the device. The sample is illuminated with a light spot from the top. (b) Optical transmission image of a single-layer MoS_2 photodetector. The substrate is polycarbonate (PC) and the source and drain electrodes are made of Au/Ti.

4.3 Strain application

The method used to apply strain is already explained in the Chapter 1. The sample is heated up/cooled down, which produces the expansion/contraction of the substrate. The thermal coefficient of the MoS_2 is negligible compare with the thermal coefficient of the substrate, resulting in the application of biaxial strain to the flake placed in the surface of the substrate. The control of the substrate expansion was carried out with a thermal stage placed under the sample (Linkam HFS600-P for both expansion/contraction measurements and a Peltier heater for only expansion measurements). The PC was chosen among other polymeric substrates due to the large thermal expansion and the high Young's modulus (E = 2.5 GPa), as shown in Figure 2. These two parameters assure a big biaxial expansion and contraction of the substrate under temperature modifications and a good strain transfer to the MoS_2 flakes deposited on top. The polycarbonate substrate transfers at least the 80% of the strain to the sample according with the calculations performed by Riccardo Frisenda and co-workers in [37]. These calculations only provide a rough approximation of the strain transfer efficiency, so perfect strain transfer is assumed during the experiments (giving a low boundary to the strain gauge values calculated).

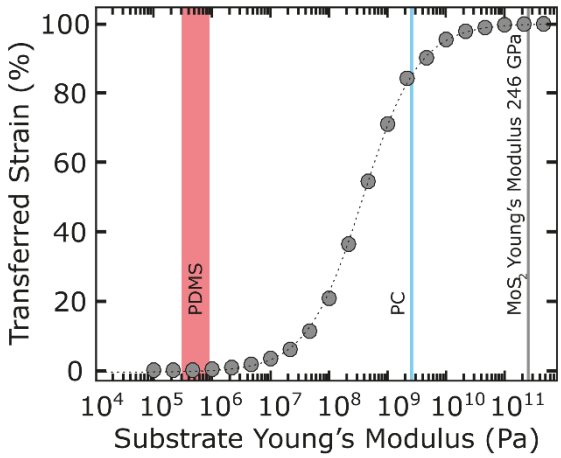

Figure 2. Finite element calculation of a biaxial strain test sample consisting of a 100-µm-thick substrate and single-layer MoS_2 (0.7 nm thickness) on the substrate. The curve represents the maximum transferred strain in MoS_2 as a function of substrate's Young's Modulus.

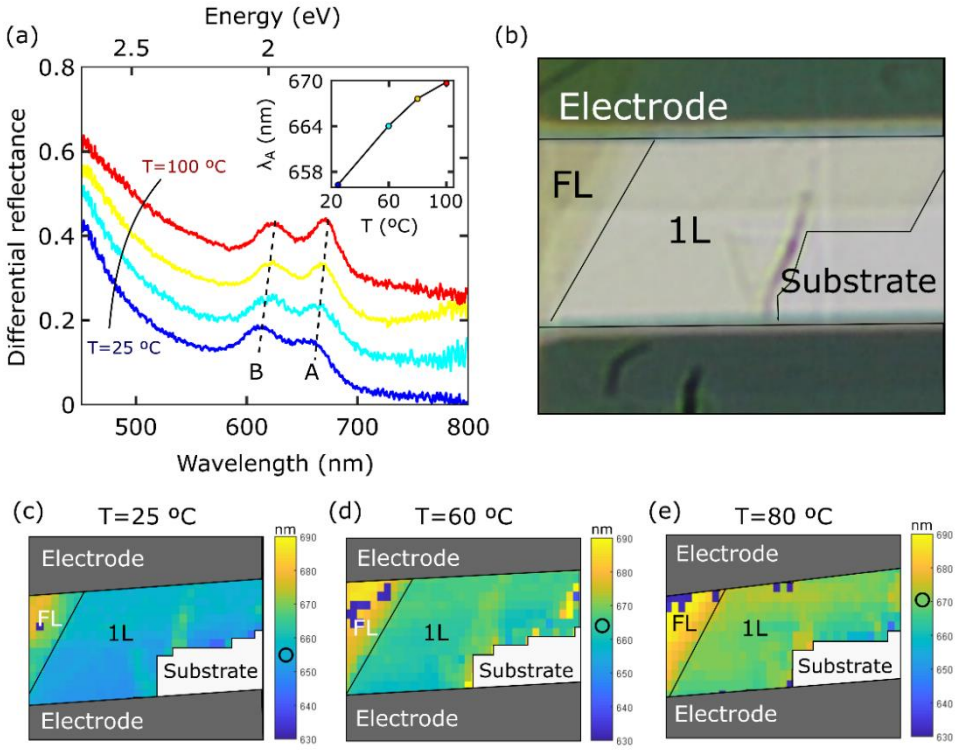

Figure 3. (a) Differential reflectance spectra measured at 25 ºC (dark blue), 60 ºC (light blue), 80 ºC (yellow) and 100 ºC (red). They are translated by 0.08 in the vertical axis. Inset: Calculated A exciton wavelength from the spectra shown. (b) Optical transmission photo of the single-layer MoS_2 device showing the different areas. (c)-(e) Exciton A energy maps, calculated from the differential reflectance spectra in each point measured at 25 ºC (c), 60 ºC (d) and 80 ºC (e).

To check the homogeneity of the strain applied along the sample, differential reflectance maps were measured in a MoS_2 photodetector at different temperatures. These measurements were performed in the micro-reflectance setup explained in Chapter 2 equipped with a XY motorized stage system controlled by a Matlab program. This XY system allows us to scan the sample in order to measure the reflection spectrum in different points. From the spectra of each point, one can extract the A exciton energy from a fit as shown in Figure 3(a). This process was done in each point, obtaining an A exciton energy map. One can observe in Figure 3(c)-(e) that the signal along the sample is homogeneous in the maps, being a clear indication of the strain homogeneity. These maps also provide information about the energy shift that the strain produces in the sample, the A exciton has an energy of 655 nm when there is no strain applied and 665 nm and 670 nm for 0.22% and 0.35% of applied strain respectively. These data are consistent with the expected results, the A exciton energy shows a redshift when there is expansive strain application due to

the bandgap reduction as previously explained in Chapter 1. Thus, we can also assure that the strain is transferred to the MoS_2 flake and there is not slippage. Apart of the slippage, another phenomenon that can occur under large levels of compressive strain is the buckling of the flake, as it was mentioned in the Chapter 1. However, there is no buckling phenomena during the application of compressive strain in our experiments. According to previous works, the buckling under compressive strain occurs at higher strain levels than $\varepsilon_c = 0.25\cdot(3\cdot E_{substrate}/E_{flake})^{2/3}$, which in our case corresponds to ~-2.7% of strain (along this work we reached only -1.48% of strain).[38,39]

4.4 Strain calibration

As mentioned before, we assumed perfect strain transfer between the substrate and the sample. For this reason, the calibration of the thermal expansion of the PC was performed, to determine the amount of applied strain with the temperature. The calibration method used for extracting the thermal expansion of polymeric substrates was reported by Frisenda et al[37]. The first step consists on the patterning of periodic pillars of resist in the PC substrate by using a Smart Print maskless lithographty system (from Microlight 3D). The sample with pillars was then placed in the Linkam HFS600-P system, in which we could vary the temperature of the sample (from -200 ºC to 100 ºC). This system has a transparent window that allows us to observe the sample with a zoom lens (Navitar) equipped with a camera (Amscope 18 MP). In Figure 4(a), we show two optical images of the samples at different temperatures. As it can be better appreciated in Figure 4(b), the distance between the pillars changes with the temperature because of the thermal contraction and expansion of the substrate. Several photos were acquired at different temperatures and then analysed with a Matlab script that finds the position of the pillars. The strain was calculated by:

$$\varepsilon = \frac{L - L_0}{L_0}$$

where ε is the strain, L is the length at the studied temperature and L_0 is the length for the unstrained substrate, in our case at 25 ºC. The results of this analysis are shown in Figure 4(c), where each dot corresponds to the value calculated in one photo. The dependency is linear, and we obtained from the fit a factor of $6.4\cdot10^{-3}$ %/ºC for the applied strain per degree (a linear expansion coefficient of $64\cdot10^{-6}$ K^{-1}).

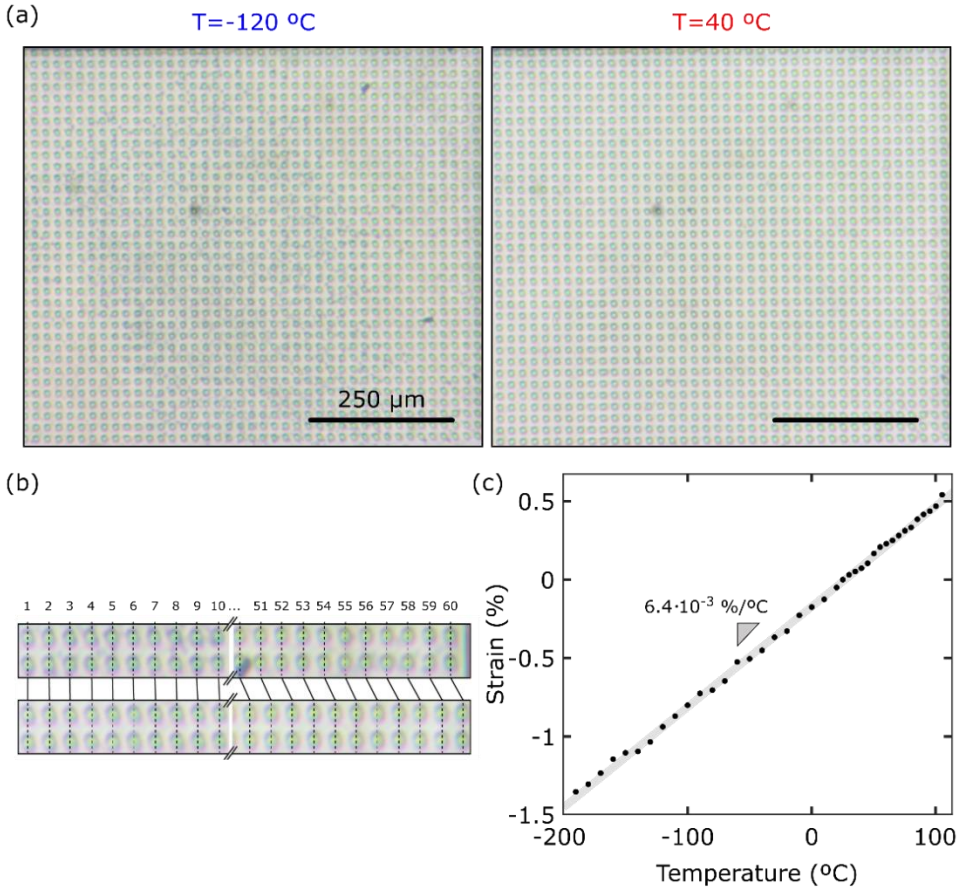

Figure 4. (a) Optical transmission images of the PC substrate with patterned pillars at -120 ºC and 40 ºC. (b) Zoom in the same area of the substrate for both temperatures in order to distinguish the expansion of the substrate thanks to the change in the distance between the pillars. (c) Calibration of the PC strain dependency on the temperature.

4.5 Optoelectrical measurements

The optoelectrical measurements were carried out with a Keithley 2450 source-meter unit connected to the Linkam system, which includes two metal probes that allows us to measure the device while controlling the temperature. The samples were illuminated through the transparent window with a spot of 400 µm of diameter. In order to create the spot, an optical fiber with a 400 µm core is attached to the light source in one side. The other side is placed in the side illumination module of the zoom lens. By adjusting the position of the fiber in the module (closer or further from the beam splitter), we can focus the spot in the sample plane, which allow us to obtain

a homogeneous power density along the whole spot area of 8 mW/cm^2. The light source used during the experiments was a Bentham TLS120Xe, which is a Xenon lamp coupled to a monochromator. The wavelength spectrum of this lamp ranges from 280 nm to 1100 nm and the wavelength can be selected with an average FWHM of 10 nm. The average power outlet of the light in the spectral range used during the experiments is ~10^{-5} W after passing through the optical system. Thus, Figure 5 shows the power spectrum of the lamp from 550 nm to 800nm, which is the wavelength interval used along the experiments.

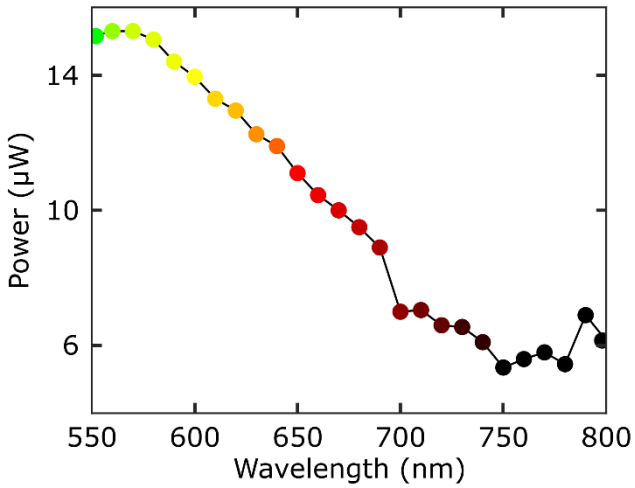

Figure 5. Xenon lamp power spectrum recorded after passing through the zoom lens. The optical fiber used has a core of 400 µm.

The MoS_2 photodetectors were measured at a constant bias voltage of 10 V. In the meantime, the light source was turned on and off for producing a square signal illumination, as shown in Figure 6. These measurements allow us to extract the current in dark conditions and the photocurrent generated in the device under light conditions. These two values are necessary to study the responsivity of the photodetector to the light. In order to obtain the spectral response of the photodetector in unstrained and strained conditions, the device was illuminated with light of wavelengths ranging from 550 nm to 800 nm, recording the response at each 10 nm. The responsivity of the device is calculated from the next expression:

$$R = \frac{I_{ph}}{P_{den} \cdot A_{dev}}$$

where R is the responsivity, I_{ph} is the photocurrent, P_{den} is the density power of the incident light and A_{dev} is the MoS_2 illuminated channel area.

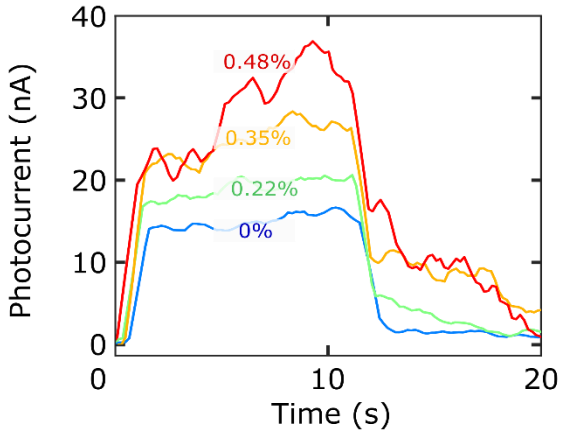

Figure 6. Response time of a single-layer MoS_2 photodetector at 0% (blue), 0.22% (green), 0.35% (orange) and 0.48% (red) of applied strain.

4.6 Photodetectors response

Figure 7 shows the responsivity spectrum of a single-layer MoS_2 device without any strain applied (which means a temperature of 25 ºC). As it was explained, each dot corresponds to one response time measurement, like the ones explained in the previous section. The responsivity values are compatible with other works in literature for MoS_2 photodetectors on SiO_2/Si substrates under similar experimental conditions (bias voltage applied and power densities), better performances are reported for higher drain-source voltage and low illumination power density.[40–42] In the responsivity spectrum, we can distinguish two peaks that correspond to the exciton A and B already observed in the differential reflectance spectra of the single-layer MoS_2 photodetector. For energies lower than the A exciton energy there is a drop in the responsivity that also appears in the differential reflectance spectra, showing a good agreement between the optical measurements and the optoelectrical behaviour of the device.[43–45]

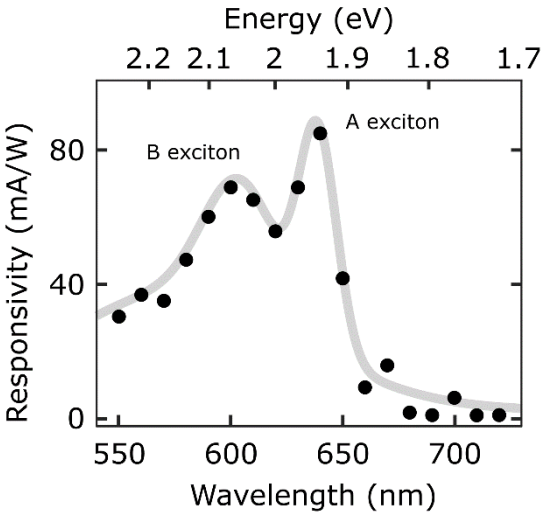

Figure 7. Responsivity spectrum of an unstrained single-layer MoS_2 photodetector. Each dot corresponds to the value extracted from a response time measurement recorded at a bias voltage of 10 V and illuminated with a light power of 8 mW/cm^2.

After obtaining the spectrum of the unstrained single-layer MoS_2 photodetector, we continued the study of the spectral response of other single-layer MoS_2 photodetectors under different applied strains. In Figure 3(a), we can observe similar shape of these spectra compared with the one displayed in Figure 7. The A and B excitonic peaks appear in all the spectra, showing a redshift/blueshift when expansive/compressive strain is applied. These results are compatible with the phenomena already obtained in the differential reflectance spectra (Figure 3(a)). The spectra were fitted with a broad gaussian background and two gaussian peaks centred in the A and B excitonic resonances. We calculated a strain gauge factor of 31 nm/% (~94 meV/%) in the A exciton energy, while a strain gauge factor of ~58 nm/% (~135 meV/%) was obtained for the photodetector cut-off wavelength. The cut-off wavelength is extracted from the wavelength value at which the photocurrent drops below the setup noise level (1pA). These data are shown in the Figure 8(b) and they are in good agreement with previous reported results in MoS_2 photodetectors fabricated on SiO_2/Si substrate.[37,46]

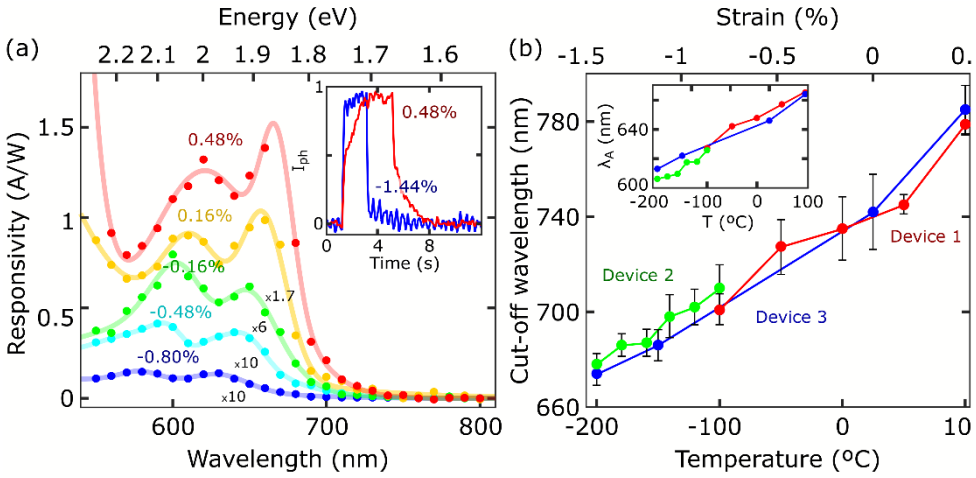

Figure 8. (a) Responsivity spectra of a single-layer MoS_2 photodetector measured at -0.80% (dark blue), -0.48% (light blue), -0.16% (green), 0.16% (yellow) and 0.48% (red) of applied strain. Each dot corresponds to the value extracted from a response time measurement recorded at a bias voltage of 10 V and illuminated with a light power of 8 mW/cm^2. The spectra are multiplied by certain factors in order to facilitate the comparison: -0.80% by 10, -0.48% by 10, -0.16% by 6 and 0.16% by 1.7. (b) Cut-off wavelengths calculated from the fits of the responsivity spectra of three single-layer MoS_2 photodetectors measured at different strain ranges. Inset: Exciton A wavelengths of the same spectra calculated from the fits.

Another phenomenon observed was an increase on the responsivity values when we applied tensile strain. Device #1 spectra recorded at several strain levels are shown in Figure 8(a), where an increment in the responsivity values by a factor of ~100 was measured between -0.8% and 0.48% of applied strain (higher changes were observed in device #2, where the increase was by a factor of ~1000 for strain ranging from -1.44% to 0.48%).

4.7 Effects of the strain in the photodetector's response

In order to elucidate the variable that was causing this huge increment in the responsivity, we first studied the performance of single-layer MoS_2 photodetectors fabricated on SiO_2/Si substrate. In this case, the strain does not play a role in the measurements (the thermal expansion coefficient of SiO_2/Si substrate is negligible) so we can separate the effect of the temperature from the strain. The results of these experiments are displayed in Figure 9, in which panel (a) shows the data for the device fabricated on PC and panel (b) for the photodetector on SiO_2/Si. It can be easily distinguish the huge responsivity increase experienced by the single-layer MoS_2 photodetector from the unstrained state to strained state (0.48% of applied strain) while there are no big changes between both responsivity spectra in the single-

layer MoS_2 photodetector fabricated in SiO_2/Si. Our findings point to the strain as the variable that produces this phenomenon of responsivity enhancement.

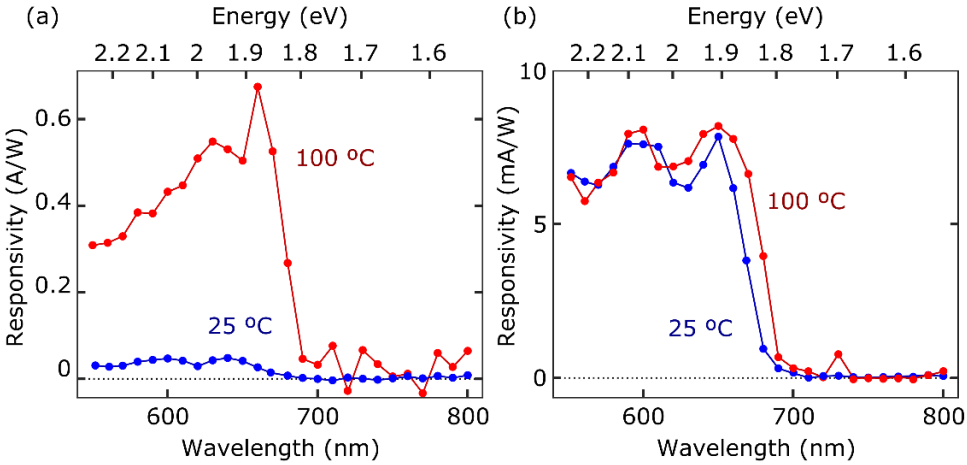

Figure 9. (a) Responsivity spectra of a single-layer MoS_2 photodetector fabricated on PC measured at 25 ºC (0% of strain) and 100 ºC (0.48% of strain). Each dot corresponds to a response time measurement at 10 V of bias voltage and illuminated with a power density of 8 mW/cm^2. (b) Responsivity spectra of a single-layer MoS_2 photodetector fabricated on SiO_2/Si measured at 25 ºC and 100 ºC (in this case there is no strain applied). Each dot corresponds to a response time measurement at 10 V of bias voltage and illuminated with a power density of 8 mW/cm^2.

An explanation for the huge difference in the behaviour of unstrained and strained devices was searched by studying the response time of the photodetectors, that it is linked to the responsivity of the devices. The photocurrent generation in MoS_2 photodetectors is carried out mostly by two different mechanisms,[40,47–49] photoconductance and photogating. Both mechanisms have different performances in response time and responsivity, which will allow to determine the dominant behaviours of our devices in different conditions.

The first mechanism, the photoconduction, usually has a response time of <10 ms and lower responsivity values. Here, the photoexcited electrons and holes are separated by the bias voltage, which will produce an increase in the device current. The responsivity for a photoconductive photodetector has a theoretical limit that can be calculated by using:

$$R = \eta \frac{q}{h \cdot f}$$

where R is the responsivity, η is the quantum efficiency, q is the electron charge, h is the Planck's constant and f is the frecuency of the light. Assuming a quantum efficiency of 100%, we would obtain values of responsivity ranging from 0.44 A/W (for light wavelength of 550 nm) to 0.65 A/W (for light wavelength of 800 nm) in the light spectrum studied. However, the real values of quantum efficiency are far from 100% because of the absorbance of MoS_2 being around ~10% in the wavelength interval considered.

On the other hand, the photogating process creates a different response in the carriers, which is shown in the scheme of Figure 10. The separation of electrons and holes is produced when the semiconductor material is illuminated with light, as it occurs during the photoconductive process. However, in this case, the minority carriers (electrons in a p-type semiconductor and holes in a n-type semiconductor) are trapped in the trap centers of the semiconductor material while the majority carriers are conducted to the drain electrodes. In order to keep the charge neutrality, a flow of majority carriers from the source electrode to semiconductor material is established. However, once in the semiconductor, the majority carriers are affected by the bias voltage and continue the flow towards the drain electrode. This process continues until the trapped minority carriers are released from the trap centers. Thus, each photon starts the generation of G minor carriers, where G is the gain of the photodetector. The gain G is then proportional to the ratio between the travelling time of the majority carriers from the source to the drain electrodes and the minority carrier trapped time. This phenomenon is quite common in 2D materials, in which the defects and impurities act as trap centers of the minority carriers.

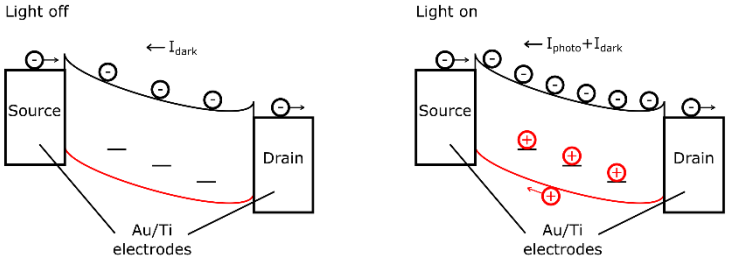

Figure 10. Schematic of the photogating mechanism. In the left, the n-type semiconductor in dark conditions conduces the majority carriers (electrons in this case) between the electrodes. In the right, the illumination produces the separation between electrons and holes in the material. The majority carriers (electrons) travel between electrodes while part of the minority carriers (holes) are trapped in the defects or impurities of the semiconductor material.

As it can be seen in the inset of Figure 8(a), the response time for compressive strain of -1.44% is very fast (lower than 80 ms, which is the resolution of our setup) compare with the slow response of ~1.5 s obtained for the photodetector with +0.48% of applied strain. These results are compatible with the enhancement in the responsivity values measured in the photodetectors. These changes in the photodetector response when the strain is increased indicates a transition from a photoconductive behaviour to a photogating mechanism, in which there is an increment in the device traps.

We again compare the response time data of the devices prepared in PC with the ones measured in MoS_2 photodetectors fabricated on SiO_2/Si substrate. The increase in the response time previously found in the PC devices does not appear in the SiO_2/Si photodetectors for temperatures from 25 ºC to 100 ºC. So, both the increase in the responsivity and the response time are characteristic from strained devices, although we could not identify the microscopic mechanism that produces the changes.

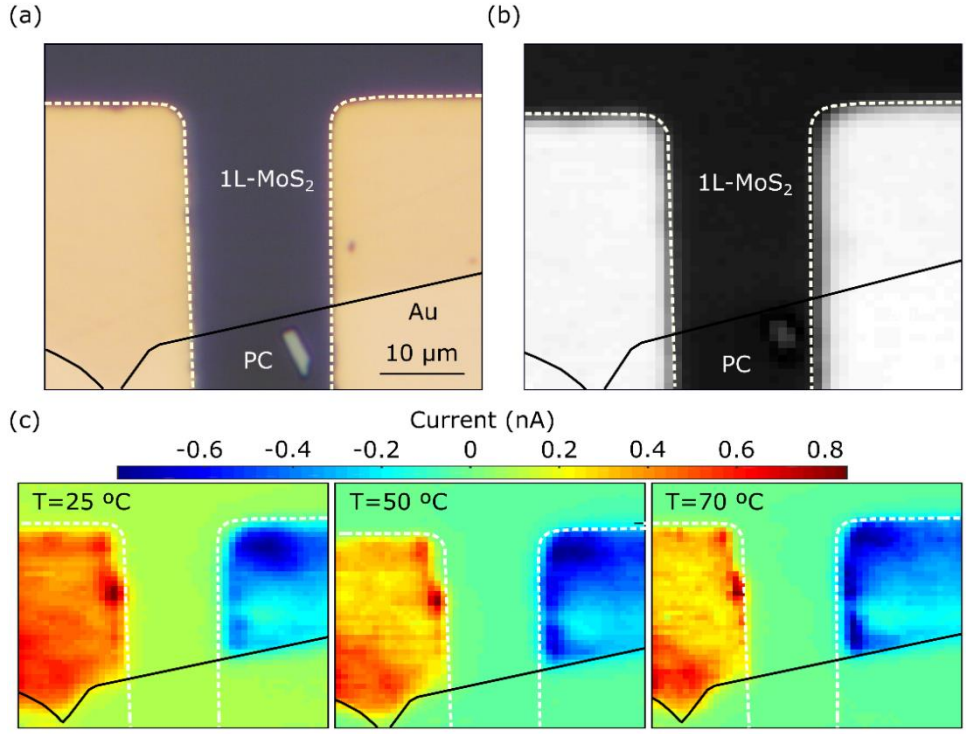

Figure 11. (a) Optical reflection photo of a single-layer MoS_2 photodetector on PC with the different areas marked. (b) Reflection map of the same photodetector measured with a laser of 650 nm. (c) Current maps of the same photodetector measured at 25 ºC, 50 ºC and 70 ºC. The lines show the same areas marked in the photo on (a) and the reflection map on (b).

We also studied the Schottky barrier height by scanning photocurrent to provide further information about the effects of strain in the photodetectors performance.[50] Figure 11 shows photocurrent maps recorded at different applied temperatures for a bias voltage of 0 V. The current values change not only along the barrier but also in the rest of the device, which implies that Schottky effect is not the only mechanism involve in the photocurrent generation. The height of the barrier was calculated by performing line cuts at several applied bias voltages as shown in Figure 12, allowing us to extract the values for different levels of strain. For the unstrained photodetector, we obtained a barrier height of ~14 meV while for the strained device the height slightly decreases with the applied strain value. This reduction of the barrier also contributes to the increment of the responsivity with the expansive strain.

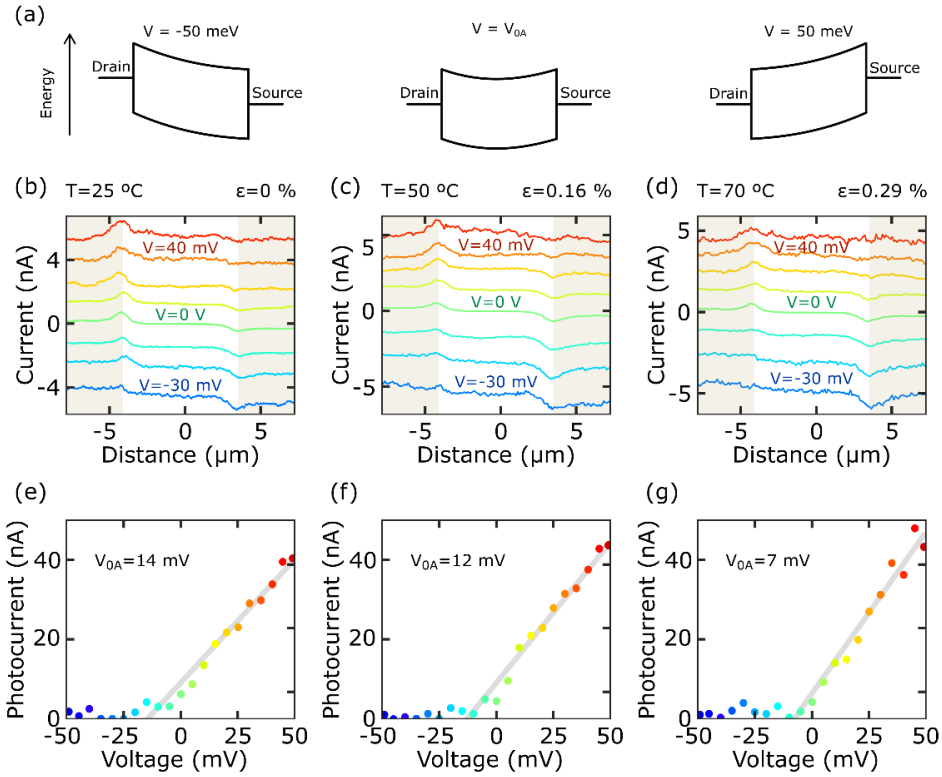

Figure 12. (a) Schematic of the band diagram for each case of applied voltage between the electrodes. (b)-(d) Current linecuts in the single-layer MoS_2 photodetector shown in Figure 8(a) measured with the same laser and applying bias voltages from -50 mV to 50 mV (measurements changing the bias voltage in 5 mV). Only few of the linecuts are shown for clarity. The electrodes area is marked with a dark area in the graphs. These linecuts were performed at 25 ºC (a), 50 ºC (b) and 70 ºC (c). (e)-(g) Current barrier measured in the left electrode at different applied bias voltages. The grey line corresponds to the fit of the linear part of the data (excluded the data points corresponding to the noise level). The fit provides an estimation of the Schottky barrier height at each temperature, given by the cut of the fit with the horizontal axis.

Consequently, we proved that the MoS_2 devices can be tuned by the application of biaxial strain. Thus, an increase in the responsivity and bandwidth is achieved with the expansive strain although the photodetector response is slower, and the opposite is found for compressive strain, lower responsivities and smaller bandwidth but faster response time. This adaptability in the photodetector performance allows us to modify the device characteristics depending on the light conditions, which would mimic the human eye adaptability (change from photopic to scotopic vision for daylight or nightlight respectively).[51] We also achieved light detection for bigger wavelength than the cut-off wavelength of unstrained MoS_2 photodetectors thanks to the redshift of the spectrum obtained by expansive strain.

4.8 Response tunability

An important parameter to study, if we aim to use the strain as a tuning knob, is the speed of the photodetector response to the applied strain. In order to extract this parameter, the strain in the sample was modulated with the Linkam system at the maximum temperature increment rate (150 ºC/min). The measurements were performed at a constant bias voltage of 5 V first in dark conditions and, right after, illuminating with light of 740 nm with a power density of 5 mW/cm^2. The data acquired in dark conditions allowed us to exclude the increase in the dark current due to the increment of the temperature, so we can calculate the change in the photocurrent generated in the device. Moreover, we chose this wavelength (740 nm) because is close to the cut-off wavelength of the unstrained MoS_2 photodetector, facilitating the inspection of the photocurrent modification.

In Figure 13(a), we can observe a considerable growth in the photocurrent when the strain level goes from 0.16% to 0.48%. This growth in the photocurrent occurs when increasing the strain level because of a combination of a redshift in the photodetector cut-off wavelength and the increase in the responsivity of the photodetector. Several cycles of strain were performed, finding a reproducible result in the change of the photocurrent. The photodetector response speed can be better appreciated in Figure 13(b), showing a value of ~20 s. This speed is currently limited by the thermalization of the Linkam stage used, which opens the possibility to improvement by utilizing different heating methods. For example, one solution could be to fabricate microheaters on the substrate surface in order to improve the heating and thermalization of the device.

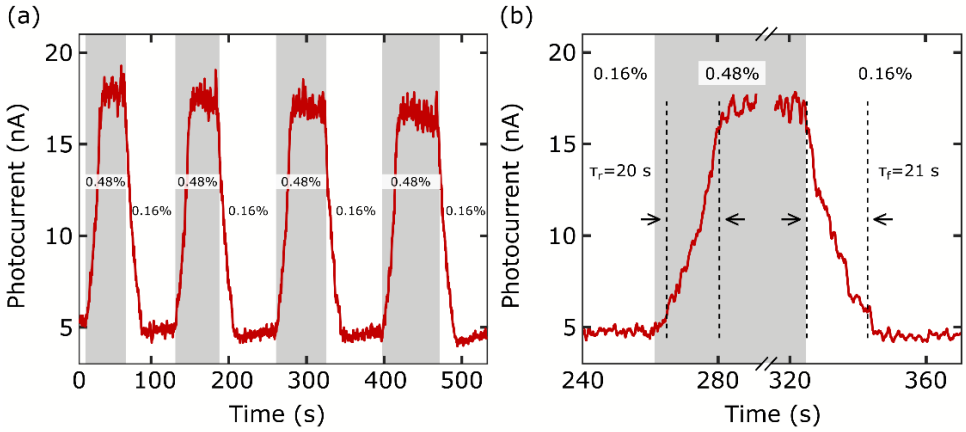

Figure 13. (a) Response time to strain of a single-layer MoS_2 photodetector. The OFF state corresponds to 0.16% of strain and ON state is 0.48% of strain. The cycles are measured at bias voltage of 5 V and light wavelength of 740 nm with a power density of 5 mW/cm^2. (b) Zoom in the third strain cycle of the measurements shown in (a) to allow the calculation of the rise and fall times, extracted with the 10%-90% criterion.

4.9 Reproducibility

Another important fact that we need to investigate, in order to prove the application feasibility, is the reproducibility in the redshift produced by strain. One single-layer MoS_2 photodetector was fabricated and subjected to 40 cycles of strain. Figure 14 displays the results of the measurements performed in some of the cycles. In this case, current versus voltage characteristics (the responsivity was calculated for a bias voltage of 10 V) were measured in dark conditions and then, in light conditions with and LED of 740 nm illumination wavelength and a power density of 12 mW/cm^2. As in the previous section, the wavelength was chosen for facilitating the determination of the response change because of its proximity to the cut-off wavelength of the unstrained MoS_2 photodetector. We observe the evolution of the responsivity from very low values (in the noise level of the setup) for no applied strain to high values when expansive strain is applied to the device, as also displayed in Figure 14. The reproducibility of the photodetector responsivity is good along the measured cycles, demonstrating that the shifts produced by the strain do not change from cycle to cycle.

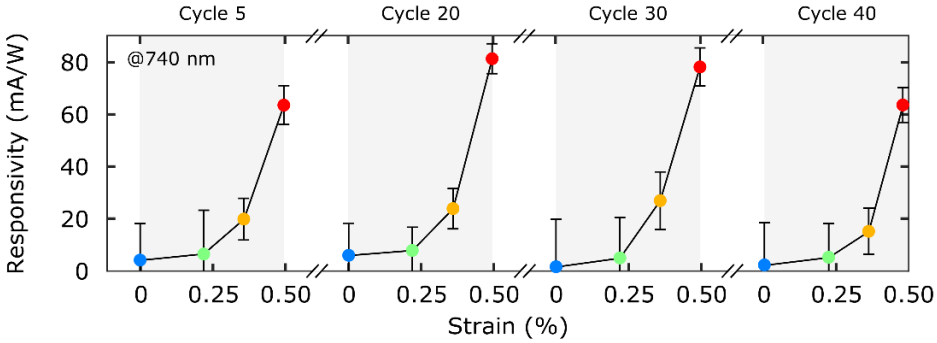

Figure 14. Responsivities of a single-layer MoS_2 photodetector measured at a bias voltage of 10 V and illuminating with light wavelength of 740 nm and a power density of 12 mW/cm^2. The strain cycles shown are the cycle 5, 20, 30 and 40.

4.10 Conclusions

As it was explained in other Chapters, the MoS_2 bandgap changes by applying strain, which allowed us to introduce in this Chapter the adjustment in the bandwidth of single-layer MoS_2 photodetectors. This mechanism is reversible, given that the strain is introduced in the sample through the control of the substrate temperature. Moreover, we are applying biaxial strain with this technique because the expansion/compression of the substrate is isotropic in the plane. When biaxial strain is applied, the MoS_2 photodetectors show a shift in the A and B exciton energies to lower energies for expansive strain and to higher energies for compressive strain, which is in good agreement with the previous spectroscopic experiments. So, the results obtained in the experiments show a strain gauge factor for the cut-off wavelength of ~58 nm/% (~135 meV/%) while the gauge factor for the A exciton is ~31 nm/% (~94 meV/%).

Furthermore, we report other changes that the strain introduces in the photodetector response. The photodetector has faster response time and low responsivity (photoconductive mechanism) for compressive strain and it has slow response time and high responsivity (photogating mechanism) for expansive strain. These different behaviours of the same photodetector for different strain values demonstrate that straintronics can be used to modify photonic devices. Thus, one example would be the change in the photodetector regime depending on the light conditions (photoconductive for bright light conditions and photogating for low light conditions), similarly to the human eye adaptation (photopic vision for bright light conditions and scotopic vision for low light conditions).

We have shown the great possibilities that 2D materials opens in the straintronic field. Opposite to 3D materials, strain can be easily applied in 2D materials in many ways without damaging them in a large scale of induced strain. Moreover, the modification of the physical properties in 2D materials by applying strain is bigger than in 3D materials thanks to their reduced thickness and the strong atomic interaction. We show the change produced in the photodetector response under strain modifications, proving the possibility of using straintronics as a tuning knob in devices.

References

1. Javey, A., Guo, J., Wang, Q., Lundstrom, M. & Dai, H. Ballistic carbon nanotube field-effect transistors. *Nature* **424**, 654 (2003).
2. Novoselov, K. S. *et al.* Electric field effect in atomically thin carbon films. *Science* **306**, 666–669 (2004).
3. Chua, L.-L. *et al.* General observation of n-type field-effect behaviour in organic semiconductors. *Nature* **434**, 194 (2005).
4. Radisavljevic, B., Radenovic, A., Brivio, J., Giacometti, V. & Kis, A. Single-layer MoS_2 transistors. *Nat. Nanotechnol.* **6**, 147–50 (2011).
5. Li, L. *et al.* Black phosphorus field-effect transistors. *Nat. Nanotechnol.* **9**, 372–7 (2014).
6. Wolf, S. A. *et al.* Spintronics: a spin-based electronics vision for the future. *Science* **294**, 1488–95 (2001).
7. Mak, K. F., He, K., Shan, J. & Heinz, T. F. Control of valley polarization in monolayer MoS_2 by optical helicity. *Nat. Nanotechnol.* **7**, 494–8 (2012).
8. Zeng, H., Dai, J., Yao, W., Xiao, D. & Cui, X. Valley polarization in MoS_2 monolayers by optical pumping. *Nat. Nanotechnol.* **7**, 490–3 (2012).
9. Cao, T. *et al.* Valley-selective circular dichroism of monolayer molybdenum disulphide. *Nat. Commun.* **3**, 887 (2012).
10. Wang, Z. L. Progress in piezotronics and piezo-phototronics. *Adv. Mater.* **24**, 4632–4646 (2012).
11. Wu, W. *et al.* Piezoelectricity of single-atomic-layer MoS_2 for energy conversion and piezotronics. *Nature* **514**, 470–474 (2014).
12. Haeni, J. H. *et al.* Room-temperature ferroelectricity in strained $SrTiO_3$. *Nature* **430**, 758 (2004).
13. Jacobsen, R. S. *et al.* Strained silicon as a new electro-optic material. *Nature* **441**, 199–202 (2006).
14. Zhao, W. *et al.* Evolution of electronic structure in atomically thin sheets of WS_2 and WSe_2. *ACS Nano* **7**, 791–7 (2013).
15. De Sanctis, A., Amit, I., Hepplestone, S. P., Craciun, M. F. & Russo, S. Strain-engineered inverse charge-funnelling in layered semiconductors. *Nat.*

Commun. **9**, 1652 (2018).
16. Lee, C., Wei, X., Kysar, J. W. & Hone, J. Measurement of the elastic properties and intrinsic strength of monolayer graphene. *Science.* **321**, 385–388 (2008).
17. Bertolazzi, S., Brivio, J. & Kis, A. Stretching and breaking of ultrathin MoS_2. *ACS Nano* **5**, 9703–9 (2011).
18. Feng, J., Qian, X., Huang, C.-W. & Li, J. Strain-engineered artificial atom as a broad-spectrum solar energy funnel. *Nat. Photonics* **6**, 866–872 (2012).
19. Roldán, R., Castellanos-Gomez, A., Cappelluti, E. & Guinea, F. Strain engineering in semiconducting two-dimensional crystals. *J. Phys. Condens. Matter* **27**, 313201 (2015).
20. Manzeli, S., Allain, A., Ghadimi, A. & Kis, A. Piezoresistivity and Strain-induced Band Gap Tuning in Atomically Thin MoS_2. *Nano Lett.* **15**, 5330–5335 (2015).
21. Conley, H. J. *et al.* Bandgap Engineering of Strained Monolayer and Bilayer MoS_2. *Nano Lett.* **13**, 3626–3630 (2013).
22. Castellanos-Gomez, A. *et al.* Local strain engineering in atomically thin MoS_2. *Nano Lett.* **13**, 5361–6 (2013).
23. Hui, Y. Y. *et al.* Exceptional tunability of band energy in a compressively strained trilayer MoS_2 sheet. *ACS Nano* **7**, 7126–31 (2013).
24. He, K., Poole, C., Mak, K. F. & Shan, J. Experimental Demonstration of Continuous Electronic Structure Tuning via Strain in Atomically Thin MoS_2. *Nano Lett.* **13**, 2931–2936 (2013).
25. Zhu, C. R. *et al.* Strain tuning of optical emission energy and polarization in monolayer and bilayer MoS_2. *Phys. Rev. B* **88**, 121301 (2013).
26. Li, H. *et al.* Optoelectronic crystal of artificial atoms in strain-textured molybdenum disulphide. *Nat. Commun.* **6**, 7381 (2015).
27. Lloyd, D. *et al.* Band Gap Engineering with Ultralarge Biaxial Strains in Suspended Monolayer MoS_2. *Nano Lett.* **16**, 5836–5841 (2016).
28. Sahatiya, P. & Badhulika, S. Strain-modulation-assisted enhanced broadband photodetector based on large-area, flexible, few-layered Gr/MoS_2 on cellulose paper. *Nanotechnology* **28**, 455204 (2017).
29. De Fazio, D. *et al.* High Responsivity, Large-Area Graphene/MoS_2 Flexible Photodetectors. *ACS Nano* **10**, 8252–8262 (2016).
30. Rodin, A. S., Carvalho, A. & Castro Neto, A. H. Strain-Induced Gap Modification in Black Phosphorus. *Phys. Rev. Lett.* **112**, 176801 (2014).
31. Çakır, D., Sahin, H. & Peeters, F. M. Tuning of the electronic and optical properties of single-layer black phosphorus by strain. *Phys. Rev. B* **90**, 205421 (2014).
32. Quereda, J. *et al.* Strong Modulation of Optical Properties in Black Phosphorus through Strain-Engineered Rippling. *Nano Lett.* **16**, 2931–2937 (2016).
33. Frisenda, R. *et al.* Micro-reflectance and transmittance spectroscopy: A versatile and powerful tool to characterize 2D materials. *J. Phys. D. Appl.*

Phys. **50**, (2017).
34. Niu, Y. et al. Thickness-Dependent Differential Reflectance Spectra of Monolayer and Few-Layer MoS_2, $MoSe_2$, WS_2 and WSe_2. *Nanomaterials* **8**, 725 (2018).
35. Castellanos-Gomez, A. *et al.* Deterministic transfer of two-dimensional materials by all-dry viscoelastic stamping. *2D Mater.* **1**, 011002 (2014).
36. Frisenda, R. *et al.* Recent progress in the assembly of nanodevices and van der Waals heterostructures by deterministic placement of 2D materials. *Chem. Soc. Rev.* **47**, (2018).
37. Frisenda, R. *et al.* Biaxial strain tuning of the optical properties of single-layer transition metal dichalcogenides. *npj 2D Mater. Appl.* **1**, 10 (2017).
38. Khang, D.-Y., Rogers, J. A. & Lee, H. H. Mechanical Buckling: Mechanics, Metrology, and Stretchable Electronics. *Adv. Funct. Mater.* **19**, 1526–1536 (2009).
39. Iguiñiz, N., Frisenda, R., Bratschitsch, R. & Castellanos-Gomez, A. Revisiting the Buckling Metrology Method to Determine the Young's Modulus of 2D Materials. *Adv. Mater.* **31**, 1807150 (2019).
40. Lopez-Sanchez, O., Lembke, D., Kayci, M., Radenovic, A. & Kis, A. Ultrasensitive photodetectors based on monolayer MoS_2. *Nat. Nanotechnol.* **8**, 497–501 (2013).
41. Yin, Z. *et al.* Single-layer MoS_2 phototransistors. *ACS Nano* **6**, 74–80 (2012).
42. Choi, W. *et al.* High-detectivity multilayer MoS_2 phototransistors with spectral response from ultraviolet to infrared. *Adv. Mater.* **24**, 5832–5836 (2012).
43. Splendiani, A. *et al.* Emerging Photoluminescence in Monolayer MoS_2. *Nano Lett.* **10**, 1271–1275 (2010).
44. Mak, K. F., Lee, C., Hone, J., Shan, J. & Heinz, T. F. Atomically thin MoS_2: A new direct-gap semiconductor. *Phys. Rev. Lett.* **105**, 2–5 (2010).
45. Castellanos-Gomez, A., Quereda, J., van der Meulen, H. P., Agrait, N. & Rubio-Bollinger, G. Spatially resolved optical absorption spectroscopy of single- and few-layer MoS_2 by hyperspectral imaging. *Nanotechnology* **27**, 5 (2016).
46. Scalise, E., Houssa, M., Pourtois, G., Afanas'ev, V. & Stesmans, A. Strain-Induced Semiconductor to Metal Transition in the Two-Dimensional Honeycomb Structure of MoS_2. *Nano Res* **2012**, 43–48
47. Buscema, M. *et al.* Photocurrent generation with two-dimensional van der Waals semiconductors. *Chem. Soc. Rev.* **44**, 3691–3718 (2015).
48. Furchi, M. M., Polyushkin, D. K., Pospischil, A. & Mueller, T. Mechanisms of photoconductivity in atomically thin MoS_2. *Nano Lett.* **14**, 6165–6170 (2014).
49. Kufer, D. & Konstantatos, G. Highly sensitive, encapsulated MoS_2 photodetector with gate controllable gain and speed. *Nano Lett.* **15**, 7307–7313 (2015).
50. Reuter, C. *et al.* A Versatile Scanning Photocurrent Mapping System to

Characterize Optoelectronic Devices based on 2D Materials. *Small Methods* **1**, 1700119 (2017).

51. Walls, G. L. *The vertebrate eye and its adaptive radiation [by] Gordon Lynn Walls.* (Cranbrook Institute of Science, 1942).

General conclusions

Here, we conclude summarizing the achievements of this thesis. The main goal of this thesis was the fabrication of a straintronic proof-of-concept device. In the Introduction, the reasons that led us to set this purpose are explained, while giving certain background about the electronics situation: the electronics scalability is threatened by several issues. The researchers are studying different approaches to solve the problems, among which we decided to explore the possibility of creating electronic components with extra tuning knobs. This approach will allow to increase the number of functionalities of each electronic component by expanding the amount of responses. There are different properties of the semiconductor material used in the components that can be used as tuning knob, so we chose the strain.

The application of strain in a material introduces changes in the physical characteristics of the material, which allowed us to control the response of the material. In order to obtain a big change in the material response, we use a 2D material as our semiconductor in the devices because of the convenience of applying strain in these materials and the possibility of reaching high levels of strain. MoS_2 is the chosen material because of the easy fabrication processes and all the information available about this material. Likewise, this material optical properties are very sensitive to the strain, which make it a good candidate for a straintronic photodetector.

In Chapter 2 I showed the main optical techniques used along this thesis. First, the well-known Raman and photoluminescence spectroscopies are explained, emphasizing their importance for the characterization of TMDCs. Then, the micro-reflectance and transmittance spectroscopies are presented. These methods are characteristics for 2D materials and were developed in our lab. In the case of TMDCs, the micro-reflectance and transmittance allow us to determine the thickness of the material besides providing information about the spectral characteristics. The last technique is used for the determination of the thickness of TMDCs with a fast method, that can be easily modified for its application to other 2D materials. All these techniques show the optical modification of the MoS_2 spectrum under strain, which is critical for the achievement of MoS_2 straintronic photodetector.

The fabrication and testing of electronic devices made of 2D materials are slightly different from the methods usually used in the electronic industry. The fabrication process usually requires from a transfer step, in which the 2D material is deposited on a substrate, and the production of electrodes that contact the 2D material for performing electrical measurements. Once the 2D material is contacted by metallic electrodes, there are several techniques for measuring the device which are also introduce in Chapter 3. The MoS_2 straintronics photodetectors used for the experiments were fabricated on polycarbonate substrate with metallic electrodes made by evaporation through shadow mask. The MoS_2 flakes were deposited between the electrodes by an all-dry deterministic transfer method. Finally, the devices were electrically contacted by different probe stations, depending on the experiment needs.

The last Chapter show all the experiments which prove the operation of a straintronic device. The MoS_2 photodetectors present a shift in the spectral response depending on the strain applied to the device. Moreover, the responsivity and the response time to the light of the photodetectors are modified by the application of strain. This behaviour is expected from a straintronic device, a change in the response introduced by the modification of the strain applied. In order to test the reliability of this type of device for the real world, we also obtained the response time to the strain and the reproducibility of the measurements in the devices. The response time to the strain was around 20 s and the data are quite reproducible. These results are very promising for the implementation of this new concept devices because there are room for improvements and optimization in the experiments and designs, these are just preliminary data from proof-of-concept devices.

This thesis achieved the main goal of creating a functional straintronic device. Our hope is that the experimental data provided here will boost the interest in this research field. Straintronics with 2D materials can be a powerful tool for improving the performance of electronic devices, but it requires from further theoretical and experimental studies. We show a simple concept for implementing straintronics in a device, which it is just the first stone for paving the path of the 2D materials straintronics research.

List of publications

1. Gant, P. *et al.* A system for the deterministic transfer of 2D materials under inert environmental conditions. *2D Mater.* **7**, 025034 (2020).
2. Gant, P. *et al.* A strain tunable single-layer MoS_2 photodetector. *Mater. Today* (2019).
3. Gant, P. *et al.* Optical contrast and refractive index of natural van der Waals heterostructure nanosheets of franckeite. *Beilstein J. Nanotechnol.* **8**, (2017).
4. Gant, P. *et al.* Lithography-free electrical transport measurements on 2D materials by direct microprobing. *J. Mater. Chem. C* **5**, (2017).
5. Zhao, Q. *et al.* A system to test 2D optoelectronic devices in high vacuum. *J. Phys. Mater.* **3**, 036001 (2020).
6. Muñoz, R. *et al.* Tailored graphenic structures directly grown on titanium oxide boost the interfacial charge transfer. *Appl. Surf. Sci.* **504**, 144439 (2020).
7. Carrascoso, F. *et al.* Direct Transformation of Crystalline MoO_3 into Few-Layers MoS_2. *Materials (Basel).* **13**, 2293 (2020).
8. Seitz, M., Gant, P., Castellanos-Gomez, A. & Prins, F. Long-Term Stabilization of Two-Dimensional Perovskites by Encapsulation with Hexagonal Boron Nitride. *Nanomaterials* **9**, 1120 (2019).
9. Taghavi, N. S. *et al.* Thickness determination of MoS_2, $MoSe_2$, WS_2 and WSe_2 on transparent stamps used for deterministic transfer of 2D materials. *Nano Res.* **12**, 1691–1695 (2019).
10. Zhang, N. *et al.* Moiré Intralayer Excitons in a $MoSe_2/MoS_2$ Heterostructure. *Nano Lett.* **18**, 7651–7657 (2018).
11. Zhao, Q. *et al.* Toward Air Stability of Thin GaSe Devices: Avoiding Environmental and Laser-Induced Degradation by Encapsulation. *Adv. Funct. Mater.* **28**, 1805304 (2018).
12. Niu, Y. *et al.* Thickness-Dependent Differential Reflectance Spectra of Monolayer and Few-Layer MoS_2, $MoSe_2$, WS_2 and WSe_2. *Nanomaterials* **8**, 725 (2018).
13. Frisenda, R. *et al.* Recent progress in the assembly of nanodevices and van der Waals heterostructures by deterministic placement of 2D materials. *Chemical Society Reviews* **47**, 53–68 (2018).
14. López, C. A. *et al.* Elucidating the Methylammonium (MA) Conformation in $MAPbBr_3$ Perovskite with Application in Solar Cells. *Inorg. Chem.* **56**, 14214–14219 (2017).
15. Frisenda, R. *et al.* Characterization of highly crystalline lead iodide nanosheets prepared by room-temperature solution processing.

Nanotechnology **28**, 455703 (2017).
16. Niu, Y. *et al*. Photodiodes based in $La_{0.7}Sr_{0.3}MnO_3$/single layer MoS_2 hybrid vertical heterostructures. *2D Mater*. **4**, 034002 (2017).
17. Frisenda, R. *et al*. Micro-reflectance and transmittance spectroscopy: A versatile and powerful tool to characterize 2D materials. *J. Phys. D. Appl. Phys.* **50**, 074002 (2017).